REVIEW

Copper–antimony and copper–bismuth chalcogenides—Research opportunities and review for solar photovoltaics

Enzo Peccerillo and **Ken Durose**, Stephenson Institute for Renewable Energy/Department of Physics, University of Liverpool, Liverpool L69 7ZF, U.K.

Address all correspondence to Ken Durose at ken.durose@liverpool.ac.uk

(Received 31 March 2018; accepted 6 August 2018)

ABSTRACT

The ternary Cu–Sb- and Cu–Bi-chalcogenides present a rich range of compounds of potential use for large-scale photovoltaics from Earth abundant elements. This paper reviews the state of fundamental knowledge about them, and their technological status with regard to solar cells. Research targets and missing data are highlighted, which may provide opportunities to help realize the goal of sustainable photovoltaics.

The family of ternary Cu–Sb- and Cu–Bi-chalcogenides and their solid solutions present a rich selection of potential candidates for Earth-abundant low toxicity photovoltaic (PV) absorber materials. Moreover, they have some novel features imparted by the ns^2 lone pair of electrons on the Sb and Bi ions. This review evaluates them as electronic materials, including experimental and theoretical evaluations of their phases, thermodynamic stability, point defects, conductivity, optical data, and PV performances. Formation of the materials in bulk, thin film, and nanoforms and the properties of the materials are critically assessed with relevance to their suitability for PV devices. There is special emphasis on $CuSbS_2$ and $CuSbSe_2$ which form the mainstay of the device literature and provide the most insights into the present-day limitation of the device efficiencies to 3 or 4%. Missing features of the literature are highlighted and clear statements recommending potential research pathways are made, which may help advance the technological performance from its present stuck position.

Keywords: photovoltaic; thin film; sustainability; nanostructure

DISCUSSION POINTS

- The photon conversion efficiency of Cu–Sb-chalcogenide solar cells is limited by their current harvesting—what is the cause of this limitation?

- Does phase purity and the possible presence of deep level recombination centers irrevocably compromise this class of materials for PV?

Introduction and scope

At the time of writing, the total annual world energy consumption is $13,500 \times 10^6$ tonnes of oil equivalent, and the demand is rising at 2.2% per annum.[1] Given the need to peg CO_2 emissions, there is a strong case that renewables should play an increasing role in the inevitable future expansion of energy production. Indeed, the renewable sector increased its energy output by 17% in 2017, mainly through wind power. Solar photovoltaic (PV) generating capacity continues to grow at the rate of 20–40% year on year, with approximately 90% of world production being of crystalline silicon modules, which are being very effectively mass produced in the Far East. The intrinsically cheaper thin film compound semiconductor alternatives, notably CdTe and copper indium gallium disulphide/diselenide (CIGS), are the strongest competitors to wafer silicon. However, while they have a significant market position, Peter[2] makes the case in a 2011 manifesto paper that these present-day thin film leaders will struggle to meet the future demand for PV if they are to provide a significant fraction of the required power generation: the underlying issues are the scarcity of the constituent elements, the competition for them from other industries, and the costs involved. The example is given that tellurium production, presently just 450–500 tonnes per annum,[3] is a factor of 100 times lower than that needed to meet the demand required.[2] Indium, although slightly less rare, is well-known to command high prices due to the competing demands for it from for the display industries. Hence it has become widely accepted that alternative, Earth abundant, and cheap materials, capable of being the mainstay of a mass-market PV industry, should

be sought. Of these, Cu_2ZnSnS_4 (CZTS) is the best known, but it suffers from the major disadvantage that despite more than a decade of research, PV devices made from it have very low voltages compared to those expected from materials having a comparable band gap. Alternative chalcogenides of copper, and antimony or bismuth are, however, potentially viable. The annual production figures (tonnes per annum) indicate that there is not a resource issue, except for the tellurides. (The figures are as follows: Cu–20,000; Sb–150,000; Bi–14,000; S–83,000; Se–3300; Te–450). There has therefore been growing interest in these materials for electro-optic applications, and they are therefore the subject of this review.

This paper comprehensively summarizes the state of knowledge of Cu–Sb and Cu–Bi chalcogenide materials and identifies research opportunities for them as potential PV materials. Recently, this family of Cu–Sb and Cu–Bi chalcogenides, long known in mineralogy, has come under scrutiny from the electronic materials community–there having been a rapid increase in the number of publications since 2010. The diversity of the compounds available from the combinations of Cu, Sb, and/or Bi and S, Se, and Te offer a wide range of potentially appropriate properties, notably band gaps and p-type semiconducting behavior. Moreover, by analogy with CIGS and CZTS, copper vacancy (V_{Cu}) driven native p-conductivity is expected for this class of materials and there is real potential for the large-scale production of p–n junction devices. For example, as the most widely explored material in the class, $CuSbS_2$ has a band gap (1.49 eV) within the optimum range 1.1–1.6 eV from the Shockley-Queisser analysis[4] and is naturally p-type. Perniu[5] has made a Kroger-Vink analysis of the conduction mechanisms and indeed deviations from stoichiometry, notably V_{Cd}, are expected to give p-type electronic conduction. (However ionic conduction on the Cu sublattice is also possible in principle and could be harmful to PV devices at elevated temperatures.)

At the time of writing, there has been sufficient interest in the Cu–Sb,Bi chalcogenides as electronic materials (about 300 papers) to warrant this overview. PV devices having efficiencies of several percent have been made by a number of labs using a variety of device architectures, most notably with $CuSbS_2$ (which has itself been the subject of a brief review[6]). However, it is fair to say that progress is presently stuck, and that some kind of breakthrough is needed to increase the efficiency further. It is a common experience that a given lab will work on $CuSbS_2$, making credible reports of some aspect of its development, only to go on to achieve no more than 1% photon conversion efficiency (PCE). The best reported is not much more than 3% PCE. It is therefore an objective of this paper to identify research targets that may enable the field to move on.

The scope and outline of this overview is as follows: Section "Cu–Sb, Bi–S, Se, Te compounds: crystallographic data, stability and phase diagrams" reports the known compounds in the Cu–Sb, Bi–S, Se, Te series, their crystal structures, phases, reactions, and Gibbs free energies of formation. Their silver analogues are beyond the scope of this paper, but a list of the known compounds and some studies of them as electronic materials are presented in Appendix A. Section "Formation and properties of bulk, thin film

and nanoparticle materials" reports the synthesis of the materials in bulk, thin film, and nanoparticle form. The preparative methods are recorded, along with the materials properties, especially those pertinent to PV, namely band gap, conductivity type, carrier concentration, and mobility. Comparisons with theory are included. Section "Photovoltaic devices–predictions of performance, design of devices and technological status" focusses on PV devices themselves, reporting structures, performance, and performance limiting aspects where known. A brief overview of the other potential applications of the materials is given in section "Other applications". Section "Conclusions and research recommendations for solar PV devices from the Cu-Sb- and Cu-Bi-chalcogenides" highlights the gaps in the current research portfolio, and opportunities for research that could result in improvements in the generally modest PCE values obtained so far.

The review uses a combination of tables with a commentary to provide an accessible yet comprehensive overview of the full output of the research community. It is the intention to draw attention to the important findings and themes, concluding with a summary of missing work and a view of the future direction of the field. The specialist researcher may wish to use section "Conclusions and research recommendations for solar PV devices from the Cu-Sb- and Cu-Bi-chalcogenides" directly and to use the remainder as a reference source, which is comprehensive at the time of writing.

Cu–Sb, Bi–S, Se, and Te compounds: crystallographic data, stability, and phase diagrams

Materials category, bonding, grain boundary passivation, and stoichiometries and solid solutions

Each of the ternary groups Cu-Sb-S, Cu-Sb-Se, Cu-Sb-Te, Cu-Bi-S, Cu-Bi-Se, and Cu-Bi-Te, comprise a wide range of compounds which are listed in Table 1 but are more easily visualized from triangular phase diagrams–a selection is shown in Fig. 1. Much of the early work on this class of materials was driven by ore mineralogy which distinguishes ternary metal sulfides as 'sulfo-salts', a subclass of the chalcogenides. The interested reader is referred to Moelo[7] for a comprehensive account, while a summary of the discoveries of $CuSbS_2$ and Cu_3SbS_3 for the PV reader are given by Lane et al.[8]

A particular feature of the Sb(III) and Bi(III) compounds is that these ions have $Sb5s^2$ and $Bi6s^2$ lone pairs that block a bonding direction (see Fig. 2). These may be considered as antibonding orbitals that are energetically stabilized by including distortions into the crystal lattice–a detailed appraisal may be found in Ref. 9. Further work on their influence on the structures of $CuSbS_2$ and $CuBiS_2$ is given by Dufton.[10] The resulting broken symmetry imparts complex crystal structures to most of the family of compounds, with orthorhombic, monoclinic, and tetragonal unit cells being common (Table 1). These crystal structures often comprise covalently bonded sheets that are themselves connected by van der Waal's forces along planes of lone pair electron density where covalent bonds may not form. Anisotropy of the physical properties is expected.

Table 1. List of Cu–Sb and Cu–Bi chalcogenide phases at room temperature with mineralogical names/appearances and crystallographic data. The crystallographic data are in chronological order. Mineral names are those adopted by International Mineralogical Association only unless in inverted commas. Visual appearances of minerals are from mindat.org.[28]

Compound Mineral name Appearance	Crystal system/space group Lattice parameters Notes
$CuSbS_2$ chalcostibite (wolfsbergite in earlier manuscripts) lead or iron gray	Orthorhombic $Pnma$
	$a = 6.018(1)$, $b = 3.7958(6)$, $c = 14.495(7)$[29]
	$a = 6.02$ Å, $b = 14.49$ Å, $c = 3.79$ Å[30]
	$a = 6.018(3)$ Å, $b = 3.794(2)$ Å, $c = 14.490(6)$ Å[31]
	Twins on {140}[32]
	Mineral occurrence see, e.g., Refs. 28 and 33
Cu_3SbS_3 skinnerite metallic luster	Monoclinic RT (β-phase) $P2_1/c$ (No. 14)
	$a = 7.81$ Å, $b = 10.25$ Å, $c = 13.27$ Å, $β = 90° 21′$,[34]
	$a = 7.808(1)$ Å, $b = 10.233(2)$ Å, $c = 13.268(2)$ Å, $β = 90.31(1)°$[35]
	$a = 7.815$ Å, $b = 10.252$ Å, $c = 13.270$ Å, $β = 90.35°$[36]
	$a = 7.8142(3)$ Å, $b = 10.2424(4)$ Å, $c = 13.2726(5)$ Å, $β = 90.294(3)°$[37]
	$a = 7.814(1)$ Å, $b = 10.242(1)$ Å, $c = 13.273(1)$ Å, $β = 90.29(1)°$[38]
	Mineral occurrence speculated by Skinner 1972,[11] listed in Ref. 28
Cu_3SbS_4 famatinite deep pinkish brown	Tetragonal $I\overline{4}2m$
	$a = 5.38$ Å, $c = 10.76$ Å[39]
	Mineral occurrence[28]
$Cu_{12+x}Sb_{4+y}S_{13}$ $0 \leq x \leq 1.92$ and $0.02 \leq y \leq 0.27$ 'tetrahedrite'	Cubic $I\overline{4}3m$
	$a = 10.308$ (1) Å[40]
	Description in Skinner 1972[11]
$CuSbSe_2$ příbramite metallic luster	Orthorhombic $Pnma$
	$a = 6.3042(15)$ Å, $b = 3.980(1)$ Å, $c = 14.989(4)$ Å[41]
	Mineral listed in Ref. 28

Continued

Table 1. Continued

Compound / Mineral name / Appearance	Crystal system/space group / Lattice parameters / Notes
Cu$_3$SbSe$_3$ bytízite	Orthorhombic *Pnma*
	$a = 7.9865(8)$, $b = 10.6138(9)$, $c = 6.8372(7)$[35,42]
	$a = 7.959(1)$ Å, $b = 10.583(1)$ Å, $c = 6.824(1)$ Å[43]
	For atom positions see Ref. 44
	Mineral listed in Ref. 28
Cu$_3$SbSe$_4$ permingeatite brown	Tetragonal *I*$\bar{4}$2*m*
	$a = 5.63$ Å, $c = 11.23$ Å[45]
	Mineral listed in Ref. 28
CuSbTe$_2$	Hexagonal
	$a = 4.22$ Å, $c = 29.9$ Å[46]
CuBiS$_2$ emplectite metallic luster	Orthorhombic *Pnma*
	$a = 6.12$ Å, $b = 3.89$ Å, $c = 14.51$ Å[29]
	$a = 6.1426(3)$ Å, $b = 3.9189(4)$ Å, $c = 14.5282(7)$ Å[47]
	$a = 6.134(1)$, $b = 3.9111(8)$, $c = 14.548(8)$[30]
	Mineral listed in Ref. 28
Cu$_3$BiS$_3$ wittichenite lead gray, bronze, tin-white, steel gray, yellow with a metallic luster	Orthorhombic *P*2$_1$2$_1$2$_1$
	$a = 7.723$ Å, $b = 10.395$ Å, $c = 6.716$ Å[48]
	Mineral listed in Ref. 28
Cu$_4$Bi$_4$S$_9$	Orthorhombic *Pbnm*
	$a = 11.589(5)$ Å, $b = 32.05(1)$ Å, $c = 3.951(5)$ Å[18,19]
	$a = 31.68(1)$ Å, $b = 11.659(4)$ Å, $c = 3.972(6)$ Å[20]
Cu$_4$Bi$_7$S$_{12}$	...

Continued

Table 1. Continued

Compound Mineral name Appearance	Crystal system/space group Lattice parameters Notes
Cu_9BiS_6	Cubic $Fm3m$
	$a = 5.563(1)$ Å[49]
	$a = 5.563$ Å[50]
$CuBi_3S_5$	…
$Cu_3Bi_5S_9$	…
$Cu_8Bi_{12}S_{22}$ hodrušite metallic luster	Monoclinic $C2/m$
	$a = 27.21$ Å, $b = 3.93$ Å, $c = 17.58$ Å, $\beta = 92°9′$[51]
	$a = 27.205$ Å, $b = 3.927$ Å, $c = 17.575$ Å, $\beta = 92°$[52]
	Mineral listed in Ref. 28
$CuBiSe_2$ grunmannite	Orthorhombic $Pnma$
	$a = 6.6362(5)$ Å, $b = 4.2581(3)$ Å, $c = 15.3691(9)$ Å[53]
	Fcc
	$a = 5.69$ Å[46]
	Mineral listed in Ref. 28
$Cu_4Bi_4Se_9$	Orthorhombic $Pbnma$
	$a = 32.692$ Å, $b = 4.120$ Å, $c = 12.202$ Å[54]
$Cu_6BiSe_4(Se_2)$ eldragónite brownish to light maroon	Orthorhombic $Pmcn$ (nonstandard)
	$a = 4.0341(4)$ Å, $b = 27.056(3)$ Å, $c = 9.5559(9)$ Å[55]
$CuBiTe_2$	Hexagonal, Bi_2Te_3 type
	$a = 4.35$ Å, $c = 30.1$[46]

An important–but yet to be realized–consequence of this structural feature is its potential effect on grain boundaries and their influence on recombination in PV devices. In the better-known diamond-like semiconductors (Si, GaAs, CdTe, CIGS, etc) the bonding is entirely covalent or covalent/ionic. The wrong- or dangling-bonds at grain boundaries are generally considered to be associated with electronic energy levels that are deep in their band gaps, and hence able to promote rapid Shockley–Hall–Reed recombination. This harms both the open circuit voltage (V_{oc}) and short circuit currents (J_{sc}) of PV devices. However, it has been pointed out that for compounds with mixed covalent and van der Waals bonding (e.g., the ribbon-bonded
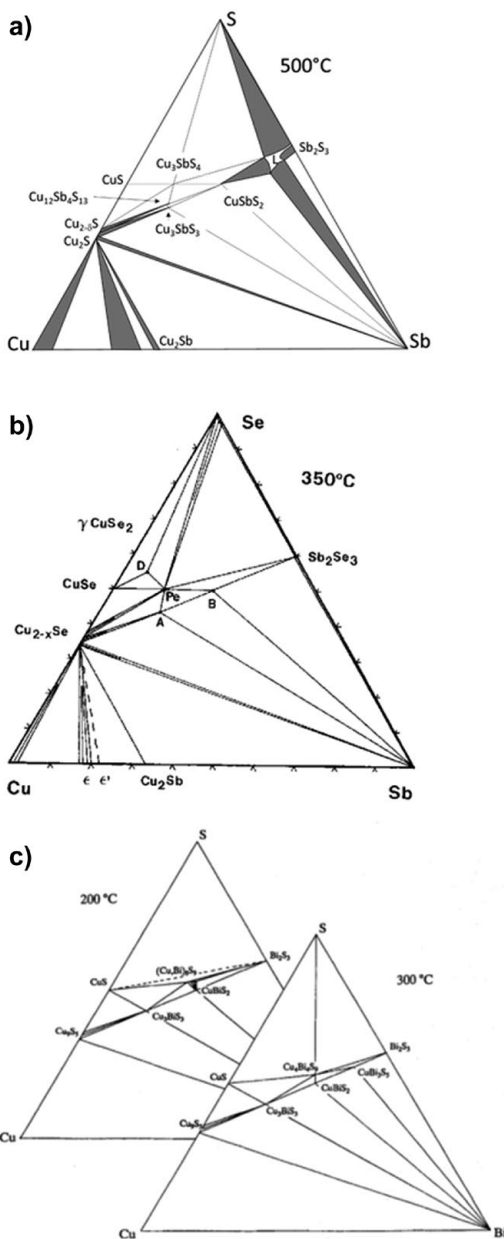
Figure 1. Ternary phase diagrams for some Cu–Sb,Bi chalcogenides—the tie lines connect the phases that exist in stable equilibrium. (a) Cu–Sb–S at 500 °C.[11] (b) Cu–Sb–Se section at 350 °C,[12] and (c) Cu–Bi–S sections at 200 and 300 °C.[13] (a) redrawn from Skinner, 1972[11] and with permission from the Society of Economic Geologists, (b) redrawn from Karup-Moller, 1999[12] www.schweizerbart.de/journals/njma with permission of Schweizerbart Science Publishers, and (c) reproduced with the permission of the Mineralogical Society of Great Britain & Ireland, from Wang, 1994.[13]

Figure 2. The crystal structure of $CuSbSe_2$ showing the layered structure that results from the lone pair on the Sb ion.[14] Covalently bonded sheets are joined by van der Waals forces. Figure from Xue, 2015,[14] reproduced with permission from John Wiley.

demonstrated in practice for any material, let alone the Cu–Sb,Bi-chalcogenides.

A second consequence of the mixed bonding in the Sb(III) and Bi(III) is that the phonon dispersion relations are affected and hence they have low thermal conductivity. For example, Ref. 17 used calculations to compare $CuSbS_2$ and its Fe analogue–the lone pairs present in the Sb, but not the Fe compound were responsible for extra phonon scattering and hence low thermal conductivity. This combination of low thermal with high electrical conductivity has led to some interest from the thermoelectric community but without any remarkable demonstrations of any high ZT figure of merit to date (see "Other applications").

While there are many members of this family of compounds, the most commonly reported ones are analogous to $CuSbS_2$, Cu_3SbS_3, Cu_3SbS_4, and $Cu_{12}Sb_4S_{13}$, i.e., substituted with Bi, Se, and Te. In addition, the Cu–Bi–S series contains the phase $Cu_4Bi_4S_9$ which is a recognized mineralogical phase that has been studied for its crystal structure.[18-20] Of these, the most important compounds for PV to date are $CuSbS_2$ (>90 papers) and Cu_3BiS_3 (>60 papers, but no devices), although there are some remarkable but as yet unverified claims for $Cu_4Bi_4S_9$ (see "Photovoltaic devices–predictions of performance, design of devices and technological status" and Table 10).

Of the many unusual stoichiometries, 'tetrahedrite' requires special explanation. Named for its striking crystal habit in natural deposits, the Sulfosalt Sub-committee of the International Mineralogical Association Commission on Ore Mineralogy[7] lists tetrahedrite as $Cu_6[Cu_4(Fe,Zn)_2]Sb_4S_{13}$, i.e., with the sum of Cu and Fe and/or Zn being 12. Indeed, the name

compound Sb_2Se_3[15]), it is in principle possible for the grain boundaries in crystallographically textured films to be van der Waal's bonded, and hence to contain no bad covalent bonds. Engineered formation of low recombination boundaries by means of encouraging aligned needle-like grains through the use of the 'structure zone model'[16] has yet be
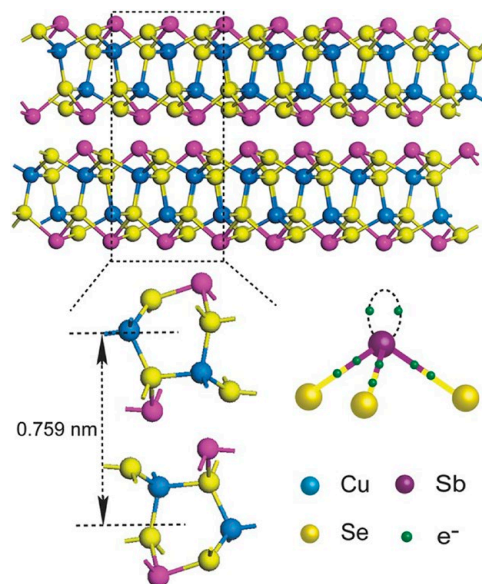
'tetrahedrite' is used in the literature to embrace a multiplicity of substituted compositions. Its pure ternary analogue, and the only one relevant here, is $Cu_{12}Sb_4S_{13}$. Deviations from this stoichiometry (the *existence region* of 'tetrahedrite' in phase space) were identified as $Cu_{12+x}Sb_{4+y}S_{13}$ $0 \leq x \leq 1.92$ and $0.02 \leq y \leq 0.27$ by Skinner.[11] The bismuth substituted analogues are named bismuthian tetrahedrites.

Given that Sb may substitute for Bi, and the chalcogens are all interchangeable, it is to be expected that many of the Cu-Sb,Bi chalcogenides will form solid solutions with their analogues. The few that have been studied are as follows:

(i) $CuSbS_2$–$CuBiS_2$: Existence of a continuous solid solution across whole composition range was verified by synthesis from the elements in the tube reaction at 310 °C (although success of forming the Bi-rich compounds depends on the heating schedule used, see Ref. 21). $CuBiS_2$ is thermally unstable to decomposition to Cu_3BiS_3 and Bi_2S_3 at 427 °C, but addition of Sb increases stability, and for $x \geq 0.3$, decomposition is not observed.[21] An unrelated paper on analytical methods demonstrated that the accuracy of 'abrasive stripping voltammetry' is $x \pm 0.03$ for the same solid solution.[22]

(ii) $CuSbS_2$–$CuSbSe_2$: The full composition range of 'mesocrystals' was synthesized by the hot injection method and shows almost linear Vegard's plots for a, b, and c.[23] Theory also supports the linear variation of the band gap with composition.[24,25]

(iii) Cu_3SbS_3–Cu_3BiS_3: Maiello[26] fabricated the full composition range and demonstrated linear behavior of Vegard's law for band gap.

(iv) $Cu_{12}Sb_4S_{13}$–$Cu_{12}Bi_4S_{13}$: Kumar[27] made the full composition range by direct reaction of the elements.

Table 2 shows the high and low temperature phases of the Cu-Sb,Bi chalcogenides and also the Gibbs free energies of formation of the room temperature phases.

Phase changes in the range of PV device operation

Since the normal temperature range of operation for solar PVs is from an upper limit of about 60 °C down to the winter minimum, few compounds in the series have phase transitions that would compromise the stability of PV devices in service. However, Cu_3SbS_3 would be susceptible to low temperatures, undergoing a transition from monoclinic to orthorhombic at −9 °C, which probably rules it out for PV applications in some climates. Its bismuth analogue, Cu_3BiS_3 has a phase transition at 118.5 °C, but this is above the likely operating range for PV.

Thermal decomposition

Thermal decomposition information is available for a limited range of the compounds. The onset of degradation has been recorded as follows (see Table 2): $CuSbS_2 > 400$ °C[58]; $Cu_3SbS_3 > 400$ °C[64]; $Cu_3SbS_4 > 300$ °C[65]; $Cu_{12}Sb_4S_{13}$ 519 °C[40] or 543 ± 2 °C[11]; and $CuBiS_2$ 472 °C.[21] These relatively low

temperatures, especially for the former three, may cause problems for the formation of films using methods where the substrate temperature is expected to exceed the decomposition point, e.g., close space sublimation.

Ternary phase diagrams, pseudo-binary phase diagrams, and reactions

Cu–Sb–S system

The ternary isothermal phase diagrams (see Fig. 1) indicate the stable phases and their relationships at a given temperature. For the Cu-Sb-S system, the earliest determinations were by Skinner[11] who made an experimental evaluation of the behavior of the main phases in the range 400–600 °C, including, for example, evaluation of the temperature dependence of the existence region of 'tetrahedrite' $Cu_{12}SbS_{13}$. Follow-on work by Braga[71] largely confirmed Skinner's findings and there is a comprehensive summary by Tesfeye Firdu.[61]

As may be expected, some of the principal phases in the Cu-Sb-S plane lie on lines connecting significant binary phases. For example, both $CuSbS_2$ and Cu_3SbS_3 lie directly on the Cu_2S–Sb_2S_3 line. Hence the pseudo-binary phase diagrams are of interest in informing the stability, reactions, and synthesis of the main phases. Figure 3 shows the Cu_2S–Sb_2S_3 pseudo-binary diagram[61,72] and this highlights the possibility of reactions of Cu_2S and Sb_2S_3 to form either $CuSbS_2$ or Cu_3SbS_3. Indeed, the combination of binary compounds has been used to inform the bulk and thin film synthesis of this class of ternary materials more generally, either from solid state reactions or by co-sputtering, for example, as described in the section "Formation and properties of bulk, thin film and nanoparticle materials".

For a full description of the phase diagrams, phase relations, and reactions in the Cu-Sb-S system, the reader is referred to the comprehensive review by Tesfeye Firdu.[61] The reader is reminded that the Cu-S phase diagram and that the number and type of phases of the $Cu_{2−\delta}S$ compounds is itself very complex–the binary phase diagram and the main phases are reported in Ref. 73.

Cu–Sb–Se and Cu–Sb–Te systems

The ternary diagram is shown in Fig. 1 for 350 °C[12] and has considerable similarities with that of Cu-Sb-S. Karup-Moller's paper[12] is comprehensive, giving the three binary Se-Cu-Sb-Se phase diagrams plus a thorough determination of the Cu-Sb-Se triangle at 300, 400, 450, 500, 600, and 700 °C.

No triangular phase diagram is known to the author for Cu-Sb-Te.

Cu–Bi–S system

Ternary isotherms for Cu-Bi-S were determined by Wang et al.[13] at 200 and 300 °C, while the pseudobinary Cu_2S–Bi_2S_3 T-x phase diagram is reported by Chang.[69] Both are contained in Tesfeye Firdu's review[61] along with accounts of the main reactions and the Gibbs free energies of formation of Cu_9BiS_6, Cu_3BiS_3, $Cu_3Bi_5S_9$, and $CuBi_3S_5$–from the elements, and from the elements in various combinations with either Cu_2S

or one of several other Cu–Bi–S compounds.[59,69] The thermochemical data come from solid state galvanic cell e.m.f measurements.[74]

A significant difference between the Cu–Bi–S and Cu–Sb–S systems is the presence of the $Cu_4Bi_4S_9$ phase, for which the Sb analogue is not recorded. $Cu_4Bi_4S_9$ is a well-documented uncontroversial orthorhombic phase that has been the subject of several crystallographic investigations.[18-20]

Cu–Bi–Se and Cu–Bi–Te systems

No phase diagrams have been reported to date to the author's knowledge.

Table 2. Phase transformations and thermochemical information. (Second, and further confirmatory reports of data in columns 2 and 3 are indented).

Formula and RTP phase	Phases and high/low temp and high pressure. (Repeat and further reports are indented)	Stability/thermochemical info for the RT phase
$CuSbS_2$ chalcostibite	Mpt 533 °C[11]	ΔG_f (400 °C) = −156.5 kJ/mol[59]
	Stable at 200 °C and 10^8 Pa under hydrothermal conditions[56]	From the elements at 25 °C
	Transforms to triclinic P1 > 8–13 GPa[57]	$\Delta G^0 = -132.86$ kJ/mol
		$\Delta H_f^0 = -130.79$ kJ/mol
		$S^0 = 149.2$ J/mol
		$C_p^0 = 88.1 + 0.0404\,T\,(\mathrm{K})$ J/mol
		$\Delta_f G_{T(\mathrm{K})}^0 = -227.07 + 0.1033\,T + 1.966\,T^{0.5}$ kJ/mol[60]
	Degrades at 350 °C to $Cu_{12}Sb_4S_{13}$, Sb_2S_3, and Sb_4[58]	From elements in standard states at 400 °C:
		$\Delta G_f^0 = -156.5$ kJ/mol[59,61]
		From Cu_2S and Sb_2S_3 at 25 °C (orthorhombic)
		$\Delta G_f^0 = -17.10$ kJ/mol
		$\Delta H_f^0 = -20.2 \pm 2.1$ kJ/mol
		$S^0 = 10.4 \pm 3.1$ J/mol,[61] and refs therein
		From Cu_2S and Sb_2S_3 at 400 °C (orthorhombic):
		$\Delta G_f^0 = -13.17$ (or 11.93) kJ/mol
		$\Delta H_f^0 = -24.8 \pm 2.7$ kJ/mol
		$S^0 = 10.4$ (or 12.3) ± 3.1 J/mol,[61] and refs therein
		Theory, Dufton 2012 HSE06
		$\Delta G_f^0 = -104$ kJ/mol[10]

Continued

Table 2. Continued

Formula and RTP phase	Phases and high/low temp and high pressure. (Repeat and further reports are indented)	Stability/thermochemical info for the RT phase
Cu_3SbS_3 skinnerite	Below −9 °C	ΔG_f (400 °C) = −273.3 kJ/mol[59]
	γ phase, orthorhombic	
	$a = 7.884(2)$ Å, $b = 10.219(2)$ Å, $c = 6.623(2)$ Å (measured at −100 °C)[35]	Calc. ΔG 'indicates decomposition at 400 °C': $2Cu_3SbS_3 = 3Cu_2S + 2Sb + 3/2S_2$[64]
	Below −10 °C $P2_12_12_1$[62] Below −9 °C γ-Cu_3SbS_3, orthorhombic $P2_12_12_1$ (No. 19), $a = 7.884(1)$ Å, $b = 10.221(1)$ Å, $c = 6.624(1)$ Å (−50 °C)[36]	From elements in standard states at 400 °C: $\Delta G_f^0 = -273.3$ kJ/mol[59,61] From reactions of the elements with Cu_2S at 400 °C: $\Delta G_f^0 = -143.055$ kJ/mol[59,61]
	Between −9 and about 115–125 °C monoclinic[8,11]	From reaction of $CuSbS_2$ with Cu_2S at 400 °C: $\Delta G_f^0 = -1.289$ kJ/mol[61,64]
	Between −9 and 122 °C Monoclinic $P2_1/c$ $a = 7.81$ Å, $b = 10.24$ Å, $c = 13.27$ Å, β = 90.4°[62] Above about 115–125 °C orthorhombic[8,11] Above 122 °C Orthorhombic $Pnma$[62] Above 121 °C, α phase, orthorhombic, either $Pnma$ (No. 62) or $Pna2_1$ (No. 33)	From Cu_2S and Sb_2S_3 at 25 °C (orthorhombic) $\Delta G_f^0 = -21.88$ kJ/mol $\Delta H_f^0 = -24.8 \pm 2.7$ kJ/mol $S^0 = 9.8 \pm 4.0$ J/mol,[61] and refs therein From Cu_2S and Sb_2S_3 at 400 °C (monoclinic) $\Delta G_f^0 = -18.2$ (or 18.25) kJ/mol $\Delta H_f^0 = -24.8 \pm 2.7$ kJ/mol $S^0 = 9.7 \pm 4.0$ J/mol,[61] and refs therein …
	$a = 7.828(3)$ Å, $b = 10.276(4)$ Å, $c = 6.604(3)$ Å (meas. at 200 °C)[35] Above 121 °C Orthorhombic $Pnma$ (No. 62), $a = 7.808(1)$ Å, $b = 10.252(2)$ Å, $c = 6.587(2)$ Å (measured at 220 °C)[36]	… … … …

Continued

Table 2. Continued

Formula and RTP phase	Phases and high/low temp and high pressure. (Repeat and further reports are indented)	Stability/thermochemical info for the RT phase
	Orthorhombic *Pnma*	...
	$a = 7.891$ (1) Å, $b = 10.312$ (1) Å, $c = 6.588$ (1) Å (measured at 570 °C)[40]	...
	Ionic conductor at $T > 122$ °C[63] (mobile Cu sub-lattice)	...
	Above 400 °C stability constrained by decomposition to $Cu_2S + Sb + S_2$[64]	...
	Melts 607.5 °C (congruent)[11]	...
Cu_3SbS_4 famatinite	Mpt ~ 627 °C[11]	...
	Begins to decompose and sublime above 300 °C[65]	
$Cu_{12}Sb_4S_{13}$ 'tetrahedrite'	At 27 °C: $I\bar{4}3m$	...
	$a = 10.308$ (1) Å[40]	
	Above 543 ± 2 °C decomposes to an 'fcc phase, Cu_3SbS_3 and Cu_3SbS_4'[11]	
	Above 519 °C: decomposes to orthorhombic Cu_3SbS_3 (i.e., the high temp. phase)[40]	
	Quenching behavior from melt:	
	- To above 95 °C single phase tetrahedrite with composition range $Cu_{12+x}Cu_{4+y}S_{13}$ 0.11 $< x < 1.77$; $0.03 < y < 0.30$	
	- To below 95 °C two immiscible phases differing in Cu content (rapid reversible transformation)[66]	
	Further complex phase relations in Ref. 66	
$CuSbSe_2$ příbramite orthorhombic *Pnma*	Atmospheric pressure: Orthorhombic *Pnma*	...
	Above 8–10 GPa: Transforms to triclinic P1[57]	
Cu_3SbSe_3 bytízite	Between −180 and 25 °C – no sign of a phase change	...
	Orthorhombic *Pnma* (No. 62)	...

Table 2. Continued

Formula and RTP phase	Phases and high/low temp and high pressure. (Repeat and further reports are indented)	Stability/thermochemical info for the RT phase
	$a = 7.9865(8)$ Å, $b = 10.6138(9)$ Å, $c = 6.8372(7)$ Å[42]	…
	At 295 K orthorhombic $Pnma$	…
	$a = 7.97$ Å, $b = 10.61$ Å, $c = 6.83$ Å[62]	…
	107 °C: order–disorder transformation at (Cu site occupancy becomes disordered and Raman/ thermal conductivity signature changes)[67]	…
Cu_3SbSe_4 permingeatite	…	…
$CuSbTe_2$	530 °C: melts	…
$CuBiS_2$ emplectite	427 °C: decomposes to Cu_3BiS_3 and Bi_2S_3.[21] Solid solution with Sb analogues are more stable	Theory, Dufton 2012 HSE06 $\Delta G_f^0 = -112$ kJ/mol[10]
Cu_3BiS_3 wittichenite	RT to 118.5 °C: orthorhombic $P2_12_12_1$ $a = 7.705$ Å, $b = 10.400$ Å, $c = 6.70$ Å[68]	From the elements at 510 °C: $\Delta G_f^0 = -238.05$ kJ/mol[59,61,69]
	Between 118.5 and 191 °C: $Pn2_1a$ or $Pnma$[68] ionic conductor at $T > 135$ °C[63] (mobile Cu sub-lattice)	
	Between 191 and 300 °C (measurement limit) $Pnma$[68]	
$Cu_4Bi_4S_9$	High pressure phase at 14.5 and reversible amorphisation at 25.6 GPa[70]	…
$CuBiSe_2$ grunmannite	585 °C: melts	…
$CuBiTe_2$	520 °C: melts	…

### Interaction of copper antimony sulfides with CIGS and ZnS

A further aspect of the copper antimony chalcogenides is that Sb has been reported to promote the formation and subsequent metallurgical change in $Cu(In,Ga)Se_2$ (CIGS). The key intermediate is Cu_3SbSe_3.

Sintering aid for chalcopyrites and kesterites

The lower melting point of $CuSbS_2$ compared to $CuInSe_2$ enables it to act as a sintering aid for thermal processing of $CuInSe_2$ solar cell materials. The use of $SbCl_3$ in this context is explained in Ref. 76. Korzun gives the relevant pseudobinary phase diagram.[77] Xiang, in work on $Cu(In,Ga)Se_2$ (CIGS), identifies Cu_3SbSe_3 as an important intermediate.[78]

It is used similarly with Cu_2ZnSnS_4 (CZTS)[79] in which it promotes grain growth, although Sb_2S_3 is more effective.

The mineralogical literature[64] evaluated the interaction of Cu_3SbS_3 with ZnS and identified the reaction:

$$4Cu_3SbS_3 + 2ZnS = Cu_{10}Zn_2Sb_4S_{13} + Cu_2S,$$
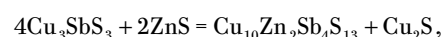
that is, ZnS is a thermodynamically unsuitable partner layer for Cu_3SbS_3 in PV devices.

Formation and properties of bulk, thin film and nanoparticle materials

This section reviews the methods used to form the compounds in their bulk, thin film and nanoparticle forms. Since these materials comprise the basis of the experimental reports of band gap, conductivity and optical dispersion, this section also provides a comprehensive account, including the results of theoretical calculations.
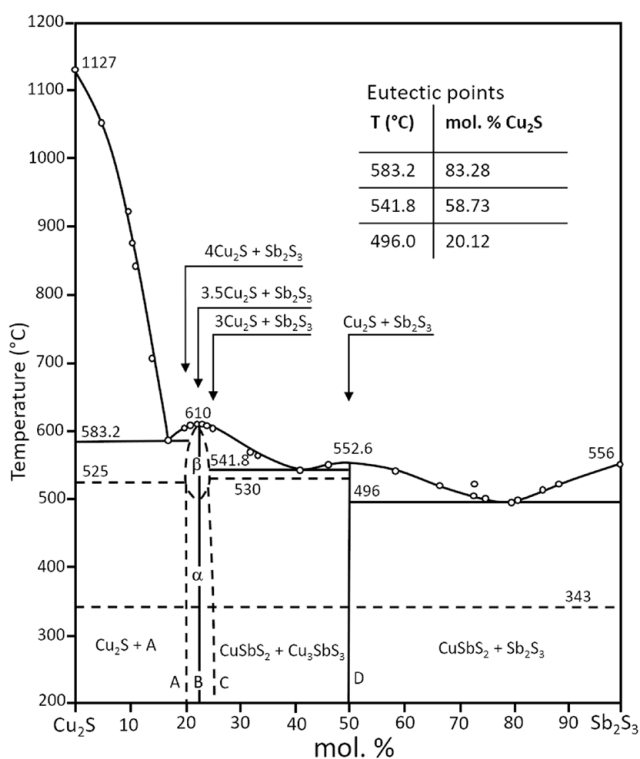
Figure 3. Pseudo-binary phase diagram of Cu_2S–Sb_2S_3. Adapted from Cambi, 1965,[72] and also appears in Tesfeye Firdu, 2010.[61] A simplified version also appears in Ref. 75.

Bulk synthesis methods (see Table 3)

A full palate of methods has been used to form the bulk materials, there being a total of just over 20 reports in all. While there are isolated studies of the optical and electrical properties of naturally occurring minerals, e.g., $CuSbS_2$,[81] the presence of impurities (nearly 5% Fe in this case) makes artificial synthesis preferable for reliable physical studies. A summary of the laboratory methods used follows, while Table 3 provides a comprehensive review of the literature reports of bulk synthesis including the band gaps and conductivity properties of the products.

Bulk synthesis from the elements (in tubes; by spark; ball milling and solvothermal methods)

Direct combination of the elements is favourable energetically and several methods have been used to achieve it in practice.

Synthesis from the elements in sealed tubes is the most widely reported method and has been demonstrated for Cu_3SbS_3,[83] 'tetrahedrite' $Cu_{12}Sb_4S_{13}$ and its mixed Sb–Bi analogue,[85] $CuSbSe_2$,[86,87] Cu_3SbSe_3,[87,89,90] and $CuBiSe_2$.[96,97] Spark sintering of the elements has been used for Cu_3SbSe_3[84] and Cu_3SbSe_3[91]; and.[91,92] The elements may also be combined by ball milling at room temperature to produce powder. While for the present family of compounds, this has only been demonstrated for $CuSbSe_2$,[88] the method has been used for CdTe and CZTS and may be expected to be general. The elements have

been combined by solvothermal synthesis in 1,2-diamino-propane to form $CuSbS_2$ and $CuSbSe_2$,[82] although to date this has only been the subject of a single paper as a method of making bulk materials.

Bulk synthesis from the binary compounds

Reactions highlighted from the pseudo-binary phase diagrams have been exploited to form $CuSbS_2$, Cu_3SbSe_3, and $CuBiS_2$: For $CuSbS_2$, CuS, and Sb_2S_3 were heated in the presence of a compensation disk to prevent volatile escape.[83] For Cu_3SbSe_3, the binaries were combined in the ratio $3Cu_2Se + 1Sb_2Se_3$ and then heated for 3 weeks at 350 °C in a quartz capsule.[42] For $CuBiS_2$, Cu_2S was combined with Bi_2S_3 at 400 °C, again with a CuS compensator.

Majsztrik[87] considers that the formation of Cu_3SbSe_3 from the elements proceeds via the intermediates Cu_2S and $CuSbSe_3$ and that the rate of the reaction is controlled by their solid state interdiffusion. Possibly this is general, but it has not been investigated for other compounds.

Crystal growth

There are few reports. Wachtel[80] grew $CuSbS_2$ by the Bridgman–Stockbarger method; Mariolacos grew Cu_3BiS_3 octahedral crystallites by HI vapor transport and gives a thorough thermochemical evaluation of the options for process chemistries.[95]

Thin film formation methods

This section outlines the methods of formation as applied to the whole series of compounds and listed by the method.

Single source evaporation

Evaporation (physical vapor deposition) is quite widely used but given the propensity for the compounds to lose components, many of the reports contain accounts of post-growth annealing in the chalcogen to correct for losses.

For $CuSbS_2$, see Refs. 98–107; For Cu_3SbS_3, Refs. 108 and 109; for $CuSbSe_2$, see Ref. 99 and by e-beam, see Ref. 110; for $CuSbTe_2$, see Ref. 99; for Cu_3BiS_3, see Ref. 111.

Co-evaporation

Co-evaporation affords greater stoichiometric control, preventing the loss of individual components, notably the chalcogen. For example, S is sometimes provided from an effusion source, but there are variants with multistep evaporation sequences.

For $CuSbS_2$ (multistep), see Ref. 112 and for $CuBiS_2$, see Ref. 113; for Cu_3BiS_3–see a number of similar reports from Mesa et al.,[114-117] also Ref. 118; for $CuBiSe_2$, see Ref. 119.

Chemical bath deposition

Most commonly, chemical bath deposition (CBD) is conducted by decomposing thiourea in the presence of the aqueous metal ions at moderate temperatures. Given the prevalence of CBD for depositing CdS and CZTS, the literature for the sulfo-salts is surprisingly sparse. It has nevertheless been extended to a wide range of them as follows:

Table 3. Formation of the bulk compounds and associated reports of their conductivity type, band gap, and resistivity where available.

Cmpd.	Ref.	Growth/synthesis technique	Conductivity type, band gap E_g (eV), resistivity
$CuSbS_2$	Wachtel 1980[80]	Bridgman–Stockbarger	Elect. Activation energy 0.28 eV
			$\rho = {\sim}20\ \Omega$ cm at 398 K
	Durant 2016[81]	Natural mineral with 4.6% Fe	p-type
			1.40 eV (indirect)
			2.0 eV (direct)
	Zhou 2008[82]	Solvothermal from the elements in 1,2-diamino-propane)	1.38 eV
			$\rho = 67\ \Omega$ cm
	Wubet 2014[83]	Reactive sintering of Cu_2S and Sb_2S_3 at 400 °C with a CuS compensation disc	p-type
			$p = 3.78 \times 10^{18}$ cm^{-3}
			$\rho = 0.067\ \Omega$ cm
			Hall mobility of 20 cm^2/(V s)
Cu_3SbS_3	Skinner 1972[11]	Reaction of the elements in sealed tubes	…
	Liu 2016[84]	Spark sintered from the elements	p-type
			$\rho = 1\ \Omega$ cm 300 K
$Cu_{12}Sb_4S_{13}$	Wang 2016[85]	From the elements in a sealed tube; synthesis studied in detail	p-type
			$\rho = 12.9$–$15.3 \times 10^{-4}\ \Omega$ cm
$CuSbSe_2$	Abdelghany, 1989[86]	From the elements in a sealed tube–melt phase at 1200 °C	7.4×10^{14} cm^{-3} defects at 360 °C (amorphous)
	Zhou 2008[82]	Solvothermal from the elements in 1,2-diamino-propane	1.05 eV more conductive than the S analogue
	Majsztrik 2013[87]	From the elements in a sealed tube	Young's modulus 53 GPa
			Hardness 36 GPa
	Zhang 2016[88]	Ball milling of the elements	$p = 9.8 \times 10^{16}$ cm^{-3} (Type not stated, but positive Seebeck)
			$\mu = 2.2$ cm^2/(V s)
			4–30 Ω cm

Continued

Table 3. Continued

Cmpd.	Ref.	Growth/synthesis technique	Conductivity type, band gap E_g (eV), resistivity
Cu_3SbSe_3	Pfitzner 1995.[42]	Combination of binaries: $3Cu_2Se + 1 Sb_2Se_3$ for 3 weeks at 350 °C	…
	Kirkham 2011[89]	From the elements at 900 °C, quenched and annealed at 325 °C	…
	Majsztrik 2013[87]	From the elements in a sealed tube: quench from the melt and anneal at 325–400 °C	Young's modulus 54 GPa Hardness 35 GPa
	Wei 2015[90]	From the elements in a sealed tube	p-type $p = 10^{16}$ cm^{-3} at 300 K $\rho = 2$–10 Ω cm $\mu = 10.5$ cm^2/(V s) $E_g = 0.95$ eV indirect
	Tyagi 2014[91]; and Ref. 92	From the elements with spark plasma sintering	p-type $\rho = 0.067$ Ω cm (300 K)
Cu_3SbSe_4:Al	93	From the elements in a sealed tube	$E_g = 0.29$ eV direct
	Tyagi 2014[91]	From the elements with spark plasma sintering	p-type $\rho = 0.019$ Ω cm
$CuBiS_2$	Wubet 2015[94]	Reactive sintering of Cu_2S and Bi_2S_3 at 400 °C with a CuS compensation disc	p-type p up to 2.4×10^{18} cm^{-3} $\rho = 0.23$ Ω cm Hall mobility 11.1 cm^2/(V s) Deviation from stoichiometry caused degradation of these values
Cu_3BiS_3	Mariola-cos 1998[95]	Vapor transport of sulfides with HI in a sealed tube between 440 and 400 °C	Small facetted crystallites
$CuBiSe_2$	Abdel-mohsen 1989, 1990[96,97]	From the elements in a sealed tube—melt phase at 1200 °C	Extrinsic up to mpt at 585 °C p-type until mpt $\rho = 10^{-5}$ Ω cm at ~530 °C

Table 3. Continued

Cmpd.	Ref.	Growth/synthesis technique	Conductivity type, band gap E_g (eV), resistivity
$Cu_{12}Sb_{(4-x)}Bi_{(x)}S_{13}$	Kumar 2017[27]	From the elements $0 < x \, 0.8$	ρ increases with Bi fraction
			p-type degenerate
			$p = 1.11 \times 10^{21}$ cm^{-3} ($x = 0$)
			6.74×10^{20} cm^{-3} ($x = 0.6$)

For $CuSbS_2$ see Refs. 120 and 121; Cu_3SbS_3 see Ref. 122; Cu_3SbSe_4 see Ref. 123 and (in ethylene glycol)[124]; $CuBiS_2$ see Refs. 125 and 126; Cu_3BiS_3 see Refs. 127–129; $CuBiSe_2$ see Ref. 130.

From combination of binary materials

As mentioned in section "Cu–Sb, Bi–S, Se, Te compounds: crystallographic data, stability and phase diagrams", the binaries may be expected to react to form the ternaries, for example, Nair[131] combined CBD films to exploit the reaction $Sb_2S_3 + 2CuS \rightarrow 2CuSbS_2 + S(g)$ in perhaps the earliest report of the formation of a thin film of this material. There is a similar report from Rodriguez-Lazcano.[122] Subsequent authors combined films deposited by both CBD and other methods. For Cu_3SbS_3, see Ref. 132; for Cu_3SbS_4, see Refs. 131 and 133; for Cu_3BiS_3, see Refs. 131, 134, and 135. In an unusual variation, Nair[136] combined CuO and Bi_2S_3 to form Cu_3SbS_3.

There are also solution variants: Yang[137] spun binary precursors from hydrazine to form $CuSbS_2$. McCarthy[31] formed the same material from Cu_2S and Sb_2S_3 in a thiol–amine mixture.

Combination of binaries with Cu films

This has been attempted for $CuSbS_2$ only.[26,138–140]

From solutions in hydrazine

In addition to $CuSbS_2$ (above[31]), hydrazine methods have been used for $Cu_{12}Sb_4S_{13}$[85,141] and $CuSbSe_2$.[142] While having the advantage of being a strong reducing agent for use in combination with semiconductor inks, for example, hydrazine is not popular on account of its toxicity and instability. Large area production methods for PV using it are not expected.

Spin coating

Several variations of spin coating have been used, for example, using CBD chemistry or nanoparticles. For $CuSbS_2$, Refs. 137 and 143–146 report wet chemical routes while Refs. 147 and 148 use nanoparticles in suspension. For $Cu_{12}Sb_4S_{13}$, see Ref. 145; for $CuSbSe_2$, see Ref. 14; for Cu_3SbSe_3, see Ref. 149. Since the hot injection methods can be tailored to form monophase nanoparticles, the spinning route has proved effective for forming specific phases, including $Cu_4Bi_4S_9$.[150] Multiple spin runs were needed to accrete sufficient material to anneal into a film.

Generally, spin coating is an excellent lab method but is not suitable for the large scale-up required for PV manufacturing.

Sulfurization of metal films and other starting materials

Following earlier practice with $CuInSe_2$ and CIGS, sulfurization of metal films has been used as a method of controlling the incorporation of volatile components. Use of elemental sulfur is most common. As for bulk vapor transport crystal growth of chalcogenides in sealed tubes, Colombara[151] points out that incorporation of a background pressure of an inert gas in the sulfurization tube can help maintain the composition of the thin film. However, using this method for $CuSbS_2$, it is retention of Sb that is the significant issue.[151] Indeed, Peccerillo conducted trials of the sulfurization of Cu–Sb metal stacks as a function of the Cu/Sb ratio: a 30% excess of Sb was required to achieve 1:1 Cu:Sb stoichiometry for films sulfurized at 400 °C in the particular apparatus used.[152]

Colombara also compares the use of H_2S with that of elemental S: the reduced driving force (free energy of formation) for the former allows for a more controllable reaction, but at the expense of having to handle toxic H_2S.[151,153]

Sulfurization of metal 'precursor' films has been used to form $CuSbS_2$ with sulfur[151–155]–with H_2S[156]; Cu_3SbS_3[26,157]–via sulfurization of acetates[158]; Cu_3SbS_4–from acetates[158]; $Cu_{12}SbS_{13}$–from acetates[158]; $CuSbSe_2$[159]; $CuBiS_2$[151] and Cu_3BiS_3[152,153,159–163]–with H_2S[153,160,161]–from sulfurization of oxides.[164]

Figure 4 shows microscopy and analysis of a $CuSbS_2$ film grown by H_2S sulfurization of electrochemically deposited metal films–the grains are ~1 μm in size, which is very acceptable for PV applications.

Electrodeposition

Electrodeposition of multernary materials is challenging on account of the differences in deposition potentials between the components. Nevertheless it has been tried for $CuSbS_2$[165] and $CuSbSe_2$.[166,167]

Spray pyrolysis

Most usually, this has been tried using CBD-like chemistry, i.e., using a metal salt or acetate and thiourea. The majority of reports have been for $CuSbS_2$,[168] 2007[169–174]; For $CuBiS_2$, see Ref. 175 and for Cu_3BiS_3, see Ref. 176.
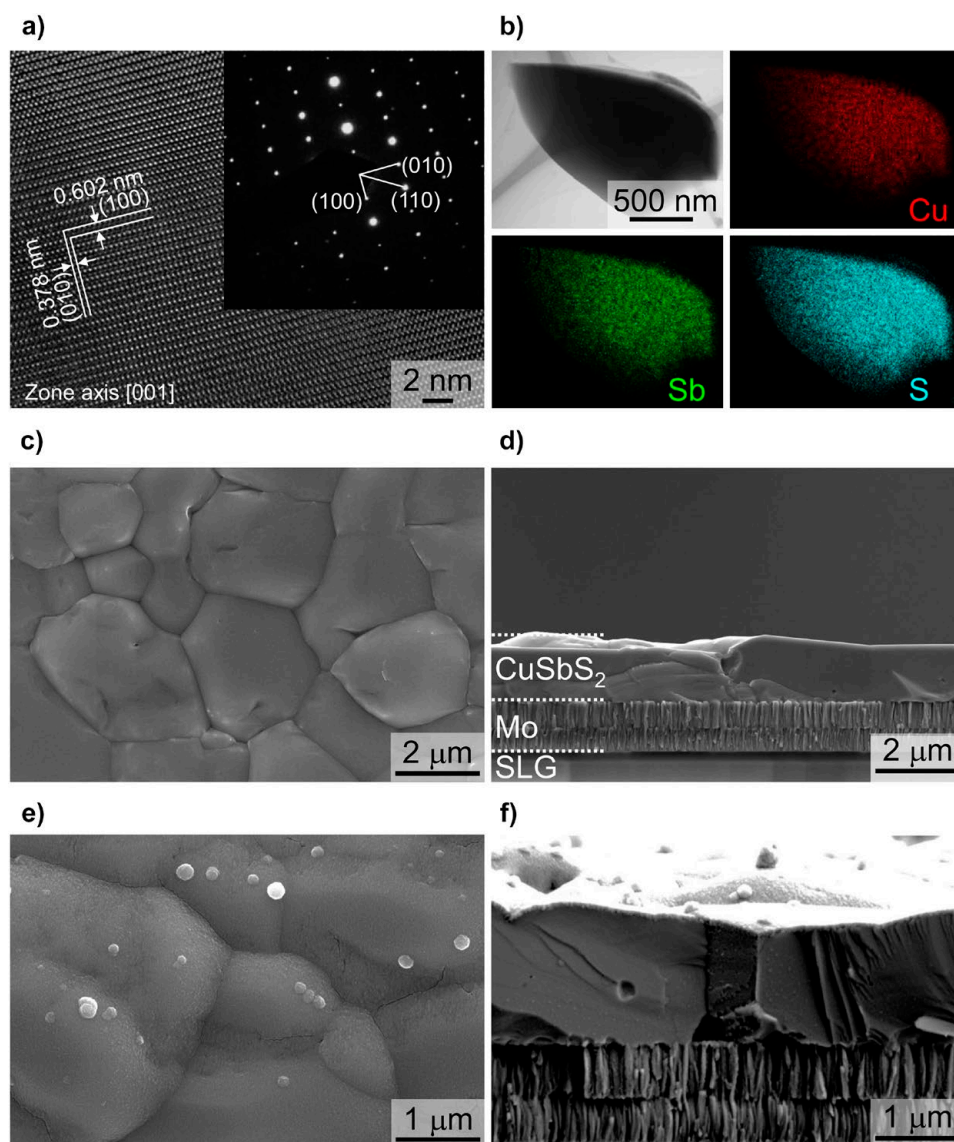
Figure 4. Microscopy of CuSbS$_2$ photocathode structure for hydrogen evolution. The film was formed by sulfurizing electrochemically deposited metal films in H$_2$S. (a) HRTEM of the lattice in [001] projection, (b) elemental mapping of a grain, (c) plan view of a CuSbS$_2$ film, (d) cross section of a 'substrate' device structure and (e and f) the same at higher magnification. The CuSbS$_2$ grains are ~1 μm in size. Figure from Zhang, 2016,[156] reproduced with permission from Elsevier.

Sputtering

Co-sputtering of the binaries is most effective and is analogous to the method of combining binary films to form the ternary. There are relatively few reports–for CuSbS$_2$, see Refs. 58, and 177–179; for CuSbSe$_2$, see Ref. 180.

Co-sputtering of Sb$_2$S$_3$ with Cu has been used to form CuSbS$_2$.[181,182] Gerein makes a number of self-similar reports of the formation of Cu$_3$BiS$_3$ by co-sputtering CuS with Bi.[160,161,183–186]

Welch[180] gives a particularly insightful study of the preparation of CuSbSe$_2$ by co-sputtering Cu$_2$Se and Sb$_2$Se$_3$: First, they recognized that the phases present in the film would be limited by both temperature and the supply of Sb$_2$Se$_3$. At high temperatures, CuSbSe$_2$ is expected to decompose, although this can be suppressed by supplying Sb$_2$Se$_3$. However, excessive pressures of Sb$_2$Se$_3$ would encourage the formation of a CuSbSe$_2$ + Sb$_2$Se$_2$ mixture. Figure 5(a) shows a calculated map of the expected phases on the T–p(Sb$_2$Se$_3$) plane and the band for which monophase CuSbSe$_2$ is expected. To explore a wide range of preparation conditions in a single run, they used nonrotating substrates to generate combinatorial samples, and their composition ranges are shown as lines in Fig. 5(a). The experimental outcome appeared to validate the phase map, with the film composition being controlled by the (spatially varying) local ratio of the supply of Sb$_2$Se$_3$ to Cu$_2$Se [Fig. 5(b)]. The resulting films had an optical
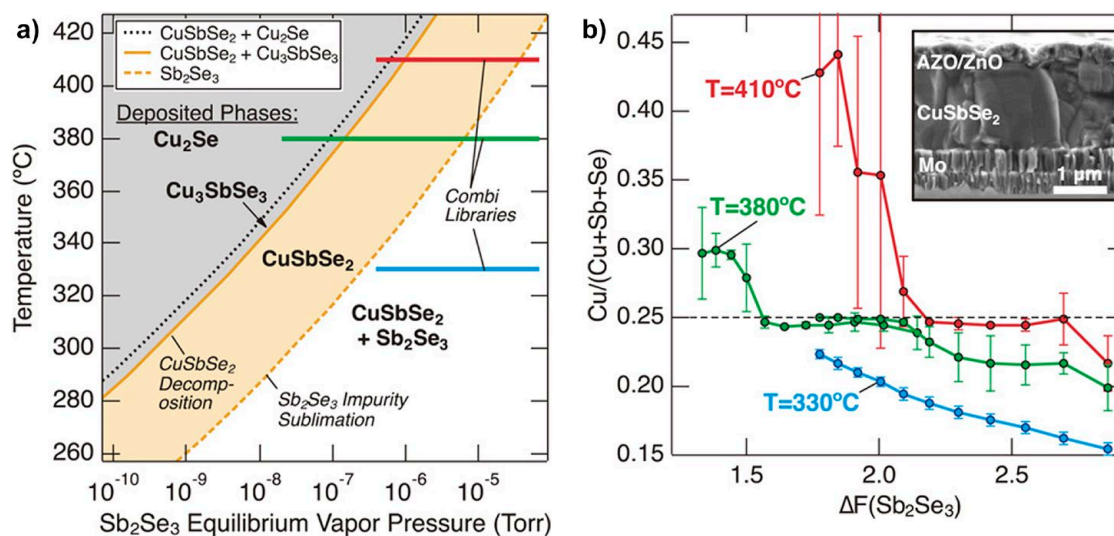
Figure 5. Preparation of $CuSbSe_2$ by co-sputtering Sb_2Se_3 and Cu_2Se on a nonrotating substrate to generate combinatorial (multicomposition) films. (a) Calculated phase map on the $T–p(Sb_2Se_3)$ plane. High temperatures are expected to cause decomposition while high pressures of Sb_2Se_3 may cause co-deposition of $CuSbSe_2$ and Sb_2Se_3. There is a central target band of growth conditions. Varying the spatially dependent flux of Sb_2Se_3 during combinatorial deposition allowed the three colored lines in (a) to be explored, and compositional analysis of them is shown in (b) as a function of the effective ratio of Sb_2Se_3/Cu_2Se (labeled ΔF). The flat regions correspond to the formation of monophase $CuSbSe_2$. Figures reproduced from Ref. 180 with permission from the Japan Society of Applied Physics. Copyright 2017 The Japan Society of Applied Physics.

band gap of 1.1 eV, an absorption coefficient of about 10^5 cm^{-1}, hole concentrations of 10^{17} cm^{-3}, and micron-sized grains.

Single target sputtering of ternaries is generally thought to be problematic, with the target composition drifting with sputtering time. The limited attempts to make it work for $CuSbS_2$ are reported in Refs. 152 and 187 and for Cu_3SbS_3,[65] it is not recommended.

CVD and ALD

$CuSbS_2$ has been made by CVD[187] from the chlorides and H_2S. ALD[188] was conducted with H_2S, bis(N,N'-disecbutylacetamidinato)dicopper(I) (CuAMD) and tris (dimethylamido)antimony(III) but required ~2500 cycles to produce usable films: it is unlikely to become popular.

Solvothermal growth

This is reported for $CuSbS_2$ ($CuCl_2–2H_2O$, potassium antimonyl tartratetrihydrate, elemental sulfur, and diethylenetriamine)[189] and Cu_3BiS_3 (from nitrates and L-cystine).[190,191] This method is more often used for nanoparticles.

Deep levels and traps

Deep levels in the fundamental gap of a semiconductor are of critical importance for the operation of solar cells since the recombination that they enable is deleterious to the voltage achievable from PV devices. Solar cells are minority carrier devices, and V_{oc} is strongly correlated with the minority carrier lifetime.

The only experimental study of deep levels reported for any of this family of materials is that by Dussan[113] for Cu_3BiS_3 using the thermally stimulated current method. The data are shown in Table 5. Nine individual traps were determined, and they have high concentrations in the material. Harm to PV performance from the traps in this particular sample is expected.

There is an important opportunity for deep level investigations to be performed on other materials in the series, particularly those that have been used in lab-scale solar cells–the efficiencies to date are not high but the underlying causes have not been identified. It must be a concern for multernary and potentially multiphase materials that deep levels are an issue, particularly in the light of the results in Table 5 for Cu_3BiS_3.

Band gaps and optical absorption/optical dispersion

All experimental reports indicate that optical absorption is high for the whole series of materials (Table 4) and that many of them have band gaps within the optimum range of 1.1–1.6 eV required for efficient PV absorber operation. Moreover, the majority are p-type, making them compatible with the industry standard n-type transparent electrodes and n-type window layers.

Nevertheless, ab initio calculations (Table 6), where they have been done, indicate that the lowest gaps for the whole series of compounds are for *indirect* transitions. However, *direct* transitions exist for energies just a fraction of an electron volt higher.

Examples include Dufton for $CuSbS_2$ and $CuBiS_2$ (Fig. 6, showing the valence band being dominated by Cu d10 states)[10] and Kehoe for Cu_3SbS_3 and Cu_3SbSe_3.[202] The solid solutions behave similarly: Takei and Wada report $CuSb(S,Se)_2$[24,25] and Chen reports both $CuSb(Se,Te)_2$ and $CuBi(S,Se)_2$.[203] An experimental determination for the solid solution series $Cu_3Sb(S,Se)_3$ demonstrated a linear Vegard's plot for band gap,[26] but did not

Table 4. Growth, band gaps, and conductivity types of films.

Compound	Method/Refs.	Optical data with E_g (eV)	Electrical data
CuSbS$_2$	Solid state reaction of binary sulfide films Nair 1997[131]; Rodriguez 2001[122]	1.52 eV[122]	p-type[122] $\rho = 33.3\ \Omega$ cm[122]
	Single source thermal evaporation Soliman 2003[98,100–104]; Suriakarthick 2015[105]; Rabhi 2015[106]; Hussain 2016[107]	1.3 eV (films only partially crystalline at 200 °C anneal)[100] Variable apparent gap (0.91–1.89) depends on substrate temp.[101] $\alpha = 10^5$–10^6 cm^{-1} at 500 nm[101] Amorphous films–apparent gap (1.36–2.21) depends on amount of material deposited[101] Apparent decrease with annealing temp from as-grown value (1.89) to 0.89 eV at 300 °C. Oxides form. $\alpha > 10^5$ cm^{-1} Ref. 103 1.36–1.61 eV n (index) 2.02–2.80[104] 1.62–2.18 eV[a] Ref. 105 1.39–1.65 depending on substrate temp. Optical dispersion graphs presented[106] 1.58 eV[107]	p-type[98,100–103,105,106] $\rho = 2\ \Omega$ cm[100] $\rho = 0.03$–$0.96\ \Omega$ cm[101] $\rho = 245$–$500\ \Omega$ cm[106] $1 \times 10^{16} < p < 8.4 \times 10^{18}$ cm^{-3} $9.8 < \mu_h < 69$ cm/(V s) $7.5 \times 10^{-2} < \rho < 8.5 \times 10^{-1}\ \Omega$ cm[105] … … … …
	Chemical bath deposition Nair 2005[120]; Ezugwu 2010[121]	1.53 eV[120] 1.3–2.3 eV depending on growth time (optical, reflectance not measured)[121]	p-type[120]
	Spray pyrolysis Manolache 2005,[168] 2007[169]; Popovici, 2012[171]; Liu, 2014[172]; Aquino, 2016[173]; Manolache, 2007[174]	1.10–1.8 eV[170] Mixed phase with Cu$_3$SbS$_4$[171] 1.72–1.75 eV[172] 1.45 eV[173] 0.92–1.15 eV[174]	p-type $2.1 \times 10^{20} < p < 5 \times 10^{20}$ $0.2 < \mu_p < 3.8$ cm^2/(V s) $0.13 < \rho < 1.34\ \Omega$ cm[173] …

Continued

Table 4. Continued

Compound	Method/Refs.	Optical data with E_g (eV)	Electrical data
	Reaction of Sb_2S_3 + Cu Garza 2011[138]; Ornelas-Acosta 2014[139]; Vinayakumar 2017[192]; Ornelas-Acosta 2015[140]	1.52–1.56 eV[138] 1.5–1.6 eV[139] 1.55 eV[140] 1.53–1.54 eV[192]	p-type[138,140] $3.9 \times 10^{18} < p < 1.4 \times 10^{20}$ $0.5 < \rho < 0.62 \ \Omega$ cm[138] …
	Sulfurization of metal films Colombara 2011[159]; Colombara 2012[153]; Ikeda 2013[154]; Peccerillo 2014, 2015[152,155]; with H_2S: Zhang 2016[156]	1.5 eV[153,154,159] 1.45 eV[156]	p-type[152,154-156,159] KCN etching improves photoresponse[159]
	Electrodeposition Rastogi 2014[165]	1.65 eV[165]	p-type[165]
	Spin coating Tian 2014[143]; Yang 2014[137]; Choi 2015[144]; Rath 2015[145]; Banu 2016[146]; from nanoparticles: Shu 2016[147]; Yddirim 2017[148]	1.4 eV[137] 1.5 eV[144] Direct 1.57 eV + Indirect 1.1 eV[145] $\alpha > 10^5$ cm^{-1} for $\lambda < 600$ nm[145] 1.58 eV[146] 1.26 eV[147] Optical dispersion measured n varies between 1.76 and 2.22[148]	p-type[137,144,146] $\tau = 1$–10 ms at TiO_2 interface (transient absorption)[145] photoconductive[147]
	Co-sputtered from binaries Zakutayev 2014[177]; Welch, 2015[58]; Lucas 2015, 2016[178,179]	1.5 eV[58,177–179]	p-type[58,178,179] $\rho = 100$–1000 Ω cm[177] $p = 10^{17}$; $\mu = 4.1$ cm^2/(V s)[178,179]
	From solution in hydrazine Yang 2014[137]; McCarthy 2016[31]	1.4 eV[137] CB is 3.85 and VB is 5.25 eV below vac level[137]	p-type[31,137] $p \sim 10^{18}$ cm^{-3} Ref. 137 $\mu = 49$ cm^2/(V s)[137] $p = 3.18 \times 10^{19}$ cm^{-3} Ref. 31 $\rho = 3.04 \times 10^3$ Ω cm[31] $\mu_h = 64.6$ cm^2/(V s)[31]

Table 4. Continued

Compound	Method/Refs.	Optical data with E_g (eV)	Electrical data
	Chloride CVD with H_2S Al-Saab 2015[187] ALD Riha 2017[188]	1.5 or 1.6 eV[188]	p-type 10^{15} cm^{-3} Ref. 188
	Single source sputtering Al-Saab 2015[187]; Peccerillo 2015[152]	1.5 eV[152]	…
	Solvothermal $CuCl_2$, potassium antimonyl tartrate trihydrate, sulfur + diethylenetriamine Shi, 2015[189]	1.45 eV[189]	Photoconductive[189]
	Co-sputtered from combined target of Cu and Sb_2S_3 Chen 2016[181]; Saragih 2017[182]	…	p-type[181,182] $p = 1.41 \times 10^{18}$ cm^{-1} $\rho = 10\ \Omega$ cm $\mu = 13$ cm^2/(V s)[182]
	Two-stage co-evaporation Wan 2016[112]	1.58 eV	p-type
Cu_3SbS_3	Chemical bath deposition Rodriguez 2001[122]	1.6 eV	…
	Sulfurization of sputtered metal films Maiello 2013[26]; Maiello 2011[157]	1.84 eV[157]	p-type[157]
	Single source thermal evaporation Nefzi 2016[108]; Nefzi 2017[109]	1.46 eV[108]	p-type[108,109] Al forms a Schottky contact $\phi_b = 0.59$ eV, $I_0 = 1.08 \times 10^{-6}$; n (index) = 1.2, $p = 2.56 \times 10^{18}$ cm^{-3} Ref. 109
	Diffusion of evaporated Cu_2S and Sb_2S_3 Hussain 2017[132]	1.6 eV $\alpha \sim 10^5$ cm^{-1}	0.2 Ω cm
	Sulfurization (elemental S) of hybrid ink from metal acetates and monoethanolamine Cho 2017[158]	1.54 eV[158]	…
Cu_3SbS_4	Solid state reaction of binary sulfide films Sb_2S_3 and CuS Nair 1997[131]; Nair 1998[133]	…	…
	Single source sputtering Franzer 2014[65]	0.94–0.97 eV[65]	…
	Sulfurization (elemental S) of hybrid ink from metal acetates and monoethanolamine Cho 2017[158]	0.81 eV[158]	…
	CBD in ethylene glycol Chen 2016[124]	1.1 eV[124]	…

Continued

Table 4. Continued

Compound	Method/Refs.	Optical data with E_g (eV)	Electrical data
$Cu_{12}Sb_4S_{13}$	Spin coating of metal xanthates Rath 2015[145]	Direct 1.74 eV $\alpha > 10^5$ cm^{-1} for $\lambda < 600$ nm[145]	$\tau = 1$–10 ms at TiO_2 interface (transient absorption)[145]
	Hydrazine solution process from Cu–S and Sb–S precursor solutions Wang 2016[85]; Wang 2016[141]	1.47 eV[85,141] CB = E_{vac} − 3.52 eV VB = E_{vac} − 4.99 eV[141]	p-type[85]
	Sulfurization of metal acetates and monoethanolamine Cho 2017[158]	1.80 eV[158]	…
$CuSbSe_2$	Selenization of metal precursors Colombara 2011[159]	1.2 eV[159]	p-type KCN etching improves photoresponse, but it remains poor[159]
	Electrodeposition + annealing Tang 2012[166]; Tang 2012[167]	1.10 eV[166,167] $\alpha = 7 \times 10^4$ cm^{-1} Ref. 167	p-type[166,167] $p = 5.8 \times 10^{17}$ cm^{-3} Ref. 167
	Co-sputtering Welch 2015[180]	1.1 eV[180]	p-type[180]
	Spin coating + annealing Xue 2015[14]	1.04 eV[14]	p-type[14]
	Hydrazine solution process starting from Cu_2S and Sb_2Se_3. Compound formed depends on temperature Yang 2017[142]	…	$p = 10^{17}$ cm^{-3} Ref. 142 sheet resistance 2.56 Ω/□[142]
	e-Beam evaporation of mechanically prepared alloy Tiwari 2017[110]	1.18 eV α up to 6×10^6 cm^{-1} Ref. 110	…
	Single source thermal evaporation Soliman 2002[99]	…	$\rho = 0.1$–0.04 Ω cm depending on film anneal temp. Conductivity in three regimes; $T > 278$ K; 278 K $> T > 200$ K; $T < 200$ K
Cu_3SbSe_3	Spun nanoparticles Liu 2014[149]	1.31 eV[a] Ref. 149	p-type[149]
Cu_3SbSe_4	CBD with microwave Ghanwat 2014[123]	1.87–1.94 eV[123]	p-type $\rho = 0.0029$–0.0032 Ω cm 310–350 S/cm (300 K)[123]

Table 4. Continued

Compound	Method/Refs.	Optical data with E_g (eV)	Electrical data
CuSbTe$_2$	Madelung 2012[46]	…	$\rho = 0.03\ \Omega$ cm
	Single source thermal evaporation Soliman 2002[99]	…	$\rho = 1.3 \times 10^{-5}$–$4 \times 10^{-4}\ \Omega$ cm depending on film annealing temp
CuBiS$_2$	Spray pyrolysis Pawar 1986[175]	1.65 eV	n-type
	CBD Sutrave 1996[125]; Sonawane 2004[126]	1.8 eV[126]	p-type $n = 10^{19}$ cm^{-3} (sic) $\mu = 6$ cm^2/(V s).[125] n-type[126]
	Sulfurization of metal precursors Colombara 2012[151]	…	…
	Co-evaporation of elements in S vapor Dussan 2012[113]	1.4 eV[113]	TSC study of trap energies[113]
Cu$_3$BiS$_3$	Reaction of CBD Bi$_2$S$_3$ and CuO Nair 1997[136]	$\alpha = 4 \times 10^4$ cm^{-1} Ref. 136	p-type $10^{-2} > \rho\ 10^{-3}\ \Omega$ cm (min for annealing 150–200 °C)[136]
	Chemical bath deposition Nair 1997[136]; Balasubramanian 2011, 2012[127,128]; Deshmukh 2016[129]	2.19–2.62 eV[a] Ref. 127 1.56–1.58 eV[129]	p-type[111,129,131] n-type[a] $n = 5.8$–14×10^{17} cm^{-3} $\mu = 5$–140 cm^2/(V s) Refs. 127 and 128[a]
	CuS film with evaporated Bi Estrella 2003[111]	1.2 eV[111]	…
	Solid state reaction of binary sulfides Nair 1997[131]; Hu 1998[134]; Hussain, 2017[135]	1.45 eV[135]	$\rho = 1\ \Omega$ cm[134]
	Sulfurization of metal films Gerein 2005[160,161]; Colombara 2011, 2012[159,162]; Colombara 2012[153]; Peccerillo[152]; Kamimura 2017[163]	1.4 eV[152,159,162] 1.63 eV[163]	p-type[152,159,162,163] $p = 3 \times 10^{17}$ cm^{-3} (est)[159,162]
	Co-sputtering of CuS and Bi Gerein 2005, 2006[160,161,183–186]	1.4 eV direct ($\alpha = 10^5$ cm^{-1} at 1.9 eV)[160,161,183–186]	p-type; $\rho = 84\ \Omega$ cm reduced to 9.6 Ω cm by annealing in H$_2$S[160,161,183–186]

Continued

Table 4. Continued

Compound	Method/Refs.	Optical data with E_g (eV)	Electrical data
	Co-evaporation of metals with sulfur Mesa 2009, 2010, 2012, 2014[114–117] Murali 2014[118]	1.41 eV[114–117] 1.45 eV[118] $\alpha > 10^4$ cm^{-1} Ref. 118	p-type[114–117] ρ = 0.24–0.45 Ω cm $T <$ 250 K variable range hopping $T >$ 350 K E_a = 0.17–0.28 eV[114–117] Hall: 2×10^{16} cm^{-3} WF = 4.37 ± 0.04 eV (4.57 ± 0.01 eV after In$_2$S$_2$ deposited)[114–117]
	Solvothermal from nitrates and L-cystine Visebicke 2013, Epstein 2015[190,191]	1.5 eV[190,191]	…
	Spray pyrolysis from chlorides and thiourea Liu, 2015[176]	1.65–1.72 eV[176]	…
	Sputtered from elements onto evaporated sulfur Yakushev 2014[193,194]	0 K band gaps of 1.24 and 1.53 eV for X and Y valence sub-bands. Direct[193,194]	p-type
	rf sputtering of CuS and Bi Gerein 2006[184]	1.4 eV	p-type
	Sulfurization of metal oxides Zhang 2016[164]	1.1–1.15 eV[164]	…
Cu$_3$BiS$_4$	…	…	…
Cu$_4$Bi$_4$S$_9$	Spun nanoparticles Liu 2013[195]; Liu 2014[196]; Liu 2015[150]; Liu 2015[197]; Liu 2016[198]; Liu 2016[199]; Wang 2016[200]	1.14 eV[201]	…
CuBiSe$_2$	Chemical bath deposition Bari 2010[130]	1.84–2.10 eV depends on stoichiometry[130]	n-type
	Co-evaporation from elements Muthukannan 2016[119]	1.84 eV $\alpha > 10^4$ cm^{-1} Ref. 119	…
	Madelung 2012[46]	…	ρ = 0.08 Ω cm
CuBiTe$_2$	Madelung 2012[46]	…	ρ = 0.05 Ω cm

CBD = chemical bath deposition.
WF = work function.
CB/VB = conduction/valence bands.
[a] Possibly unreliable.

Table 5. Trap energies in Cu_3BiS_3 as determined from thermally stimulated current measurements.[113] The temperatures T_m are the signal peaks, while the trap energies E_t were evaluated from the data by two methods and with some consistency. N_t is the trap density.

Peak	T_m (K)	E_t (eV) Initial slope method	Peak shape	N_t (cm^{-3})
T_{11}	187.8 ± 0.3	0.97 ± 0.03	1.00 ± 0.03	(1.62 ± 0.009) × 10^{17}
T_{12}	195.0 ± 0.2	1.32 ± 0.07	1.73 ± 0.10	(4.3 ± 0.2) × 10^{16}
T_{13}	205.66 ± 0.05	1.09 ± 0.03	1.15 ± 0.01	(3.48 ± 0.19) × 10^{17}
T_{21}	188.3 ± 1.6	0.517 ± 0.012	0.53 ± 0.05	(2.31 ± 0.13) × 10^{16}
T_{22}	195.6 ± 0.2	1.36 ± 0.12	1.77 ± 0.13	(6.8 ± 0.4) × 10^{15}
T_{23}	215.1 ± 2.3	1.13 ± 0.04	1.2 ± 0.2	(6.8 ± 0.4) × 10^{16}
T_{24}	224.6 ± 3.2	0.91 ± 0.03	1.0 ± 0.3	(1.53 ± 0.08) × 10^{17}
T_{31}	214.98 ± 0.13	1.13 ± 0.05	1.14 ± 0.02	(5.1 ± 0.3) × 10^{17}
T_{32}	237.2 ± 0.2	0.441 ± 0.008	0.482 ± 0.002	(9.5 ± 0.5) × 10^{18}

identify the two kinds of transition. Indeed, clear identification of direct and indirect transitions is difficult using in practice using the routine Tauc methods most commonly reported in the literature. An exception is for Cu_3BiS_3 for which the zero Kelvin band gaps of 1.24 and 1.53 eV were measured photoreflectance methods for the 'X' and 'Y' valence sub-bands.[193,194]

Xue reports the temperature dependence of the band gap of $CuSbSe_2$[14] and finds it to conform to a Varshni-type function[14]:

$$E_g(T) = 1.176 - \frac{5.486 \times 10^{-4} T^2}{T + 24.673} \text{ (eV)}.$$

Despite this family of compounds having lowest indirect rather than direct gaps, practically speaking optical absorption is strong for them all, with absorption coefficients in the range 10^4–10^5 cm^{-1} being common. The number of similar reports suggests that this high level of absorption is genuine (even though it is becoming increasingly expected to have to report the absorption coefficients in the introductions of papers on new PV materials as being >10^5 cm^{-1}, whether it has been measured or not!). Moreover, calculated absorption spectra support the finding that the absorption coefficients of $CuSbS_2$, $CuBiS_2$, and similar compounds exceed those of the better-known absorbers $CuInS_2$ and $CuInSe_2$, for example, as shown in Fig. 7.[204]

Full knowledge of the optical dispersion relations for the thin film components of PV devices is essential for the prediction and modeling of the optical performance solar cells. Full dispersion data for $CuSbS_2$ thin films are reported for a range of preparation conditions as shown in Fig. 8.[106] The data for these thin films differ slightly from that of Yddrim for nanoparticles[148] due to scattering. Apart from this, for $CuSbS_2$, there are occasional single wavelength measurements, as shown in Table 4. None of the other compounds in the series appear to have had their dispersion relations measured. This is a significant omission from the literature.

Summary of optical band gap values

Tables 4 and 6 give comprehensive lists of the experimental and theoretical band gap values reported for this class of materials while the section 'Band gaps and optical absorption/optical dispersion' has discussed the physics of the transitions. Table 7 provides a summary of the experimental values where they are available. Since there are many reports for some of the compounds (e.g. $CuSbS_2$), average values of the reported optical gaps listed in Table 4 have been shown here. In cases where the original work uses the Tauc plot method, and the resulting graph does not have a convincing straight line section for extrapolation, then that data has been excluded from the average. However, for Cu_3SbSe_3 there is a single report for which the data does not look reliable, but it has been included for completion. Bandgap measurements for $CuSbTe_2$, Cu_3BiS_4, Cu_3BiSe_3, Cu_3BiSe_4, and $CuBiTe_2$ have not been reported in the literature to date.

Conductivity type (electronic) and point defect energetics

The majority of the compounds in this family are naturally p-type. For example, there are just over 30 independent reports of hole conduction in $CuSbS_2$. Similarly, Cu_3BiS_3 is

Table 6. Ab initio theory studies of the band properties of the Cu–Sb and Cu–Bi chalcogenides. Most studies of most of the compounds concur that the lowest fundamental transition is indirect and that the lowest direct transition is a fraction of an eV higher. Nevertheless, both theory and experiment show them to be exceptionally strong absorbers and hence possible candidates for PV devices: There is no indication at present that their band properties will be disadvantageous.

Compound	Author	E_g and conductivity type (if predicted)
$CuSbS_2$	Gudelli 2013[205]	1.05 eV indirect TB-mBJ
	Kumar 2013[204,206]	1.72 eV indirect 1.83 direct HSE06
	Tablero 2015[207]	0.81–1.47 eV ($0 < U < 10$ eV) DFT + U
$CuSbSe_2$	Kumar 2013[204]	1.36 eV indirect 1.41 eV direct HSE06
$CuSb(Se_{1-x}Te_x)_2$	Chen 2017[203]	Trend of decreasing gap shown from 1.43 to 1.07 eV with increasing x
Cu_3SbSe_3	Do 2012[208]	various; n-type
Cu_3SbSe_4	Do 2012[208]	various; p-type
Cu_3SbS_3	Kehoe 2013[202]	2.02 eV indirect 2.13 eV direct HSE06
Cu_3SbSe_3	Kehoe 2013[202]	1.50 eV indirect 1.76 eV direct HSE06
$CuBiS_2$	Tablero 2015[207]	0.87–1.57 eV ($0 < U < 10$ eV) DFT + U
	Kumar 2013[204,206]	1.58 eV indirect 1.69 eV direct HSE06
	Zhang 2014[209]	...

Continued

Table 6. Continued

Compound	Author	E_g and conductivity type (if predicted)
CuBiSe$_2$	Kumar 2013[204]	1.14 eV indirect
		1.32 eV direct
		HSE06
CuBi(S$_{1-x}$Se$_x$)$_2$	Chen 2017[203]	Trend of decreasing band gaps from 1.3 to 1.07 eV with increasing x
Cu$_3$BiS$_3$	Kehoe 2013[202]	1.69 eV indirect
		1.79 eV direct
		HSE06
Cu$_3$BiS$_3$	Kumar 2013[210]	1.5–1.7 eV indirect
		1.6–1.8 eV direct
		HSE06
Cu$_3$BiSe$_3$	Kehoe 2013[202]	1.17 eV indirect
		(Direct at 1.43 eV)
		HSE06
Cu$_4$Bi$_4$S$_9$	Li 2014[211]	…

widely reported to be p-type and the isolated report from one author of its being n-type is probably in error. CuBiS$_2$ is less clear: there are two reports of n-type films[126,175] and two reports of p-type material, in thin film[125] and bulk[94] forms. Perhaps it can assume both conductivities, in any case it should be re-investigated. CuBiSe$_2$ is a similar case, one author's work on thin film[130] indicating n-type, and another's on bulk,[96,97] p-type.

The p-type conductivity of the copper chalcogenides is generally rationalized in terms of the provision of an excess of the volatile components (e.g., Sb and a chalcogen) that would encourage the formation of copper vacancy acceptors. However, density functional theory is helpful in confirming this in a more systematic way. A good example is the work of Xue 2015 who evaluated the energetics of the full set of vacancies, interstitials, and antisites for CuSbSe$_2$.[14] Of these, V$_{Cu}$ and Cu$_{Sb}$ are acceptors and Cu$_i$, V$_{Se}$, and Sb$_{Cu}$ are donors. Figure 9 shows how the energy of the defects varies as a function of the Fermi level position for the cases of Se-poor and Se-rich conditions. In Sb-rich conditions, the most easily formed defects are V$_{Cu}$ acceptors and Cu$_i$ donors, and it is the position of their balance point that determines the Fermi level position. In the case of Se-rich growth, the formation of V$_{Cu}$ is encouraged and their population grows, decreasing the Fermi level–but at the same time increasing the formation energy for V$_{Cu}$ until it is equaled by that of Cu$_i$ when $E_F = 0.2$ eV. Here, the formation energy of V$_{Cu}$ is 0.5 eV and at 300 °C, this would equate to $p = 10^{18}$ cm^{-3}. This is consistent with experimental findings. On the other hand, when growth is conducted under Se-poor conditions, the formation energies of V$_{Cu}$ and Cu$_i$ are more closely matched, and their densities become equalized near the mid-gap point. Hence the donors would compensate the acceptors and the material would be expected to be intrinsic. Xue concludes by noting that the native defects in CuSbS$_2$ and CuSbSe$_2$ are not expected to be deep, and hence would not cause recombination problems. Nevertheless, as will be seen later, recombination losses are serious in these materials, but this is at least partly due to the control of the width and position of the depletion region. A similar theoretical study showing the prevalence of copper vacancies in CuSbS$_2$ is reported by Yang et al.[137]

Experimentally it is also found that for CuSbS$_2$, the Sb/(Sb + Cu) ratio influences both the carrier concentration and mobility, but oppositely, as shown in Fig. 10.[58,177] While a
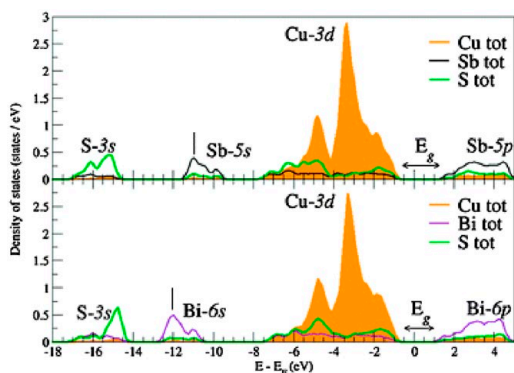
Figure 6. Density function theory calculations of the band character in $CuSbS_2$ (top) and $CuBiS_2$ (bottom). The tops of the valance bands are dominated by Cu^+ d^{10} filled states, similar to CZTS and CIGS. Figure from Dufton, 2012.[10] Reproduced by permission of the PCCP Owner Societies.
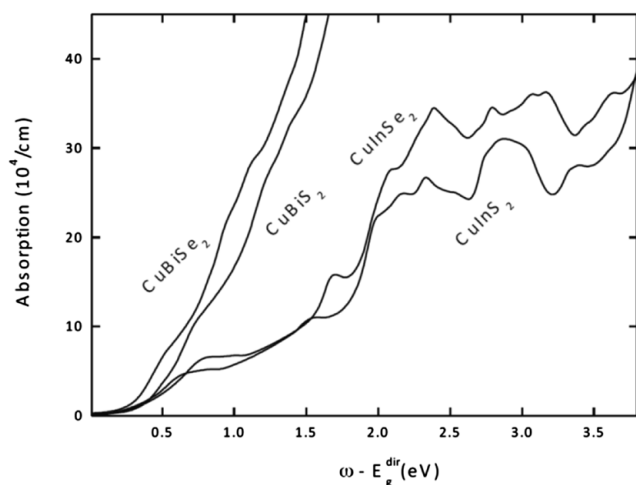

Figure 7. Calculated absorption spectra for $CuBiS_2$ and $CuBiSe_2$ in comparison to $CuInS_2$ and $CuInSe_2$. The Cu–Bi chalcogenides show stronger absorption than the Cu–In ones. Calculations also show similarly strong absorption for $CuSbS_2$ and $CuSbSe_2$. From DFT HSE06 calculations—figure from Kumar, 2014[204] reproduced with permission from Elsevier.

Figure 8. Optical dispersion relations for $CuSbS_2$ films fabricated by evaporation from bulk ingots and presented as a function of the post-growth annealing temperature.[106] Despite their value in modeling solar cell performance, there are very few reports of dispersion relation measurements for the whole family of compounds. Figure from Rabhi, 2015,[106] reproduced with permission from Elsevier.

deficiency of Cu (Sb excess) increases the carrier concentration (i.e., the population of V_{Cu}) as expected, the hole mobility rises faster as the Sb is depleted (Cu excess)–the Sb-poor samples have the highest conductivity, as shown in the figure. Welch goes on to consider the effect of Sb-rich, Cu-poor and Sb-poor, Cu-rich compositions.[212]

Note on ionic conduction

As mentioned in the introduction, Perniu[5] used the Kroger–Vink methodology to make a paper assessment of the possibility of ionic conduction in $CuSbS_2$. From the standpoint of PV devices, which operate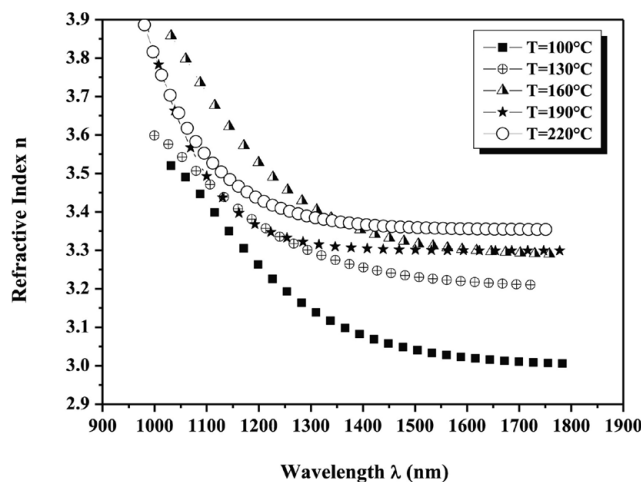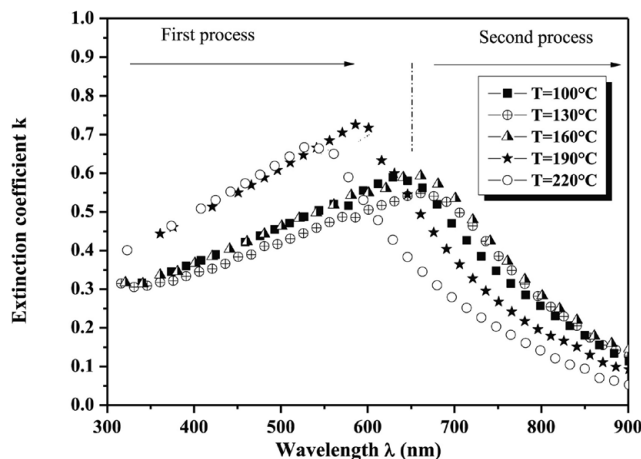 in dc conditions, the exposure to a continual field having the same polarity could cause electromigration which could be harmful to the stability of PV devices. Indeed, the once promising Cu_2S–CdS solar cell ultimately failed to get to market on account of Cu-related instability. Experimentally, ionic conduction on the mobile Cu sublattice has been seen to operate at higher temperatures ($T > 122$ °C in Cu_3SbS_3, and $T > 135$ °C Cu_3BiS_3[63]). While PV devices might not be expected to reach these temperatures in service, this does point to an increasing tendency to instability of the Cu, at least for these materials. This should be explored further by experiment in those compounds in the series that may be of interest for PV applications.

Missing nanoparticles and missing nanosolar cells

A comprehensive list of the reports of the formation of 'nano-' and other particles from the Cu-Sb- and Cu-Bi-chalcogenides is presented in Table 9. Despite there being about 70 reports, there
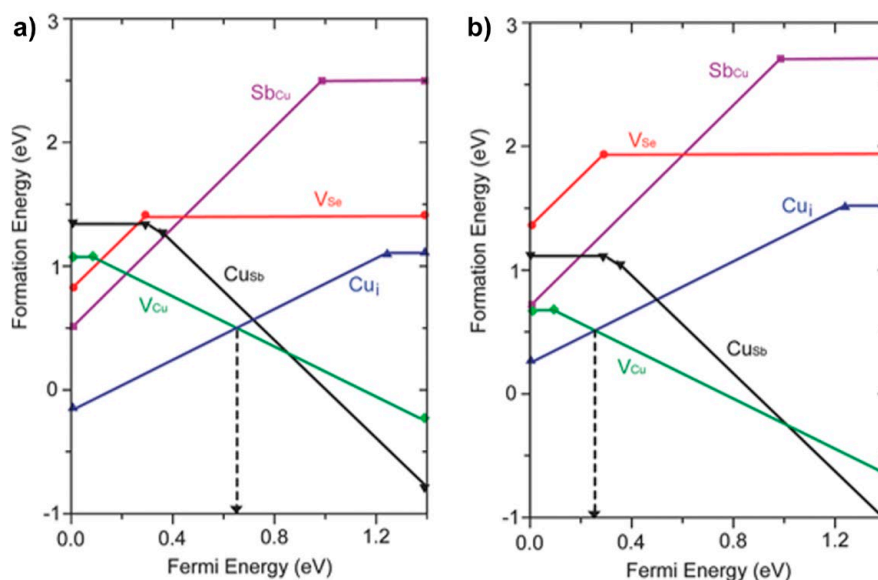
Figure 9. $CuSbSe_2$ defect chemical potentials determined by density functional theory calculations[14] for Se-poor (a) and Se-rich (b) growth conditions. For both, the lowest energy defects are V_{Cu} and Cu_i and Xue considers that the Fermi level is determined by their balance point. In the case of Se-rich material (b), the density of V_{Cu} increases from left to right until it is matched by Cu_i—at this point the carrier density due to vacancies is estimated as $p = 10^{18}$ cm^{-3}. Such high carrier concentrations are observed in practice. Figures reproduced from Xue, 2015[14] with permission from John Wiley.

are some surprising omissions from the literature. First, there are comparatively few reports of making actual solar cell devices with nanoparticles (there is one quantum dot device, two attempts at dye sensitized solar cell (DSSC) structures, and some controversial some spun film-made devices–for a full commentary see the section titled "synthesis methods for nanoparticles"). Second, to the

Figure 10. Conductivity versus antimony metal fraction for the Cu–Sb–S system, showing the positions of $CuSbS_2$ and $Cu_{12}Sb_4S_{13}$. The inset shows the hole density and carrier mobility in the vicinity of the stoichiometric $CuSbS_2$ position. Cu-poor compositions encourage the formation of V_{Cu} and hence increase p-type carrier concentration, but the mobility (inset) decreases slightly. Figure reproduced from Welch, 2015[58] with permission from Elsevier. See also Zakutayev, 2014.[177]

author's knowledge, quite a number of the family members of this chemical class have not yet been synthesized in the form of nanoparticles (Table 9). The sulfides are quite well represented (excepting $CuBiS_2$ and $Cu_{12}Bi_4S_{13}$) but only two of the selenides have been synthesized ($CuSbSe_2$ and Cu_3SbSe_3) and none of the tellurides. The entire row of $CuBiX_2$ analogues remain to be made, and the bismuthic tetrahedrites $Cu_{12}Bi_4X_{13}$, are also entirely absent.

Finally, it may be of interest to synthetic chemists that $Cu_4Bi_4X_9$ has been made by the solvothermal method but not by hot injection while for the reverse is true for $Cu_{12}Sb_4S_{13}$ and $CuSbSe_2$.

Synthesis methods for nanoparticles

'Solvothermal' and 'hot injection' synthesis methods are equally popular. The next most-reported methods, 'chemical bath' and 'thiocarbamate' routes, each have a factor of three fewer reports and others have been attempted just one or two times each. A summary of the methods follows:

Solvothermal synthesis

Copper, antimony, and bismuth present as chlorides, nitrates, or sulfates (occasionally others) are reacted with a chalcogen source, most often L-cystine for S (but occasionally thiourea, thioglycolic acid, or sulfur). Details of the variations reported and the protocols for other chalcogens are listed in Table 8.

Hot injection

This method is equally popular as the solvothermal methods. Copper, antimony, and bismuth are supplied as acetates, acetylacetonates (acac), chlorides, or nitrates and reacted
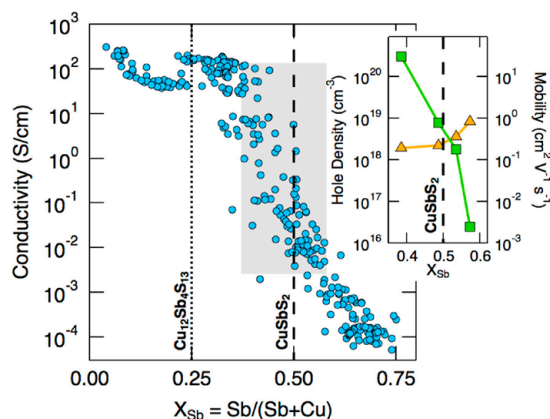
Table 7. Band gaps of the Cu–Sb and Cu–Bi chalcogenides. These are average values of the experimental optical band gaps taken from Table 4. Where the band gaps in the source papers have been from nonlinear sections of Tauc plots, the data were excluded, except for Cu_3SbSe_3 for which there is only one report. For $CuBiSe_2$, there is a single paper which reports the range of values given in the table.

Sb-compound	Band gap/eV	Bi-compound	Band gap/eV
$CuSbS_2$	1.49	$CuBiS_2$	1.61
Cu_3SbS_3	1.60	Cu_3BiS_3	1.40
Cu_3SbS_4	0.96	Cu_3BiS_4	…
…	…	$Cu_4Bi_4S_9$	1.14
$Cu_{12}Sb_4S_{13}$	1.67	…	…
$CuSbSe_2$	1.12	$CuBiSe_2$	1.84–2.1
Cu_3SbSe_3	1.31[a]	Cu_3BiSe_3	…
Cu_3SbSe_4	1.9	Cu_3BiSe_4	…
$CuSbTe_2$	…	$CuBiTe_2$	…

[a] Possibly unreliable data.

most usually with elemental sulfur in solution with oleylamine, but other sulfur sources and solvents/mixed solvents have been reported, as shown in Table 8. 1-dodecanethiol is popular.

Thermal decomposition of thiocarbamates

Since metal thiocarbamates such as $Bi(S_2CNEt_2)_3$ and $Cu(S_2CNEt_2)_2$ are a single source of both a metal and S, their thermal co-decomposition in a suitable solvent provides an opportunity for synthesis of the ternaries. As listed in Table 8, this has been demonstrated for $CuSbS_2$,[213] Cu_3SbS_3,[213] $Cu_{12}Sb_4S_{13}$,[213] Cu_3BiS_3,[214,215] and $Cu_4Bi_4S_9$.[214] Manipulation of the solvent choice can be used to tune the particle size, e.g., Deng 2014[214] changed the size and morphology from sheets (1 μm; 1.29 eV) to particles (25 nm; 1.35 eV) for Cu_3BiS_3 and recorded a corresponding change in band gap, presumably from quantum confinement (Table 8).

Chemical bath deposition-like reactions

Thermal decomposition of thiourea in the presence of the metal ions, usually in aqueous solution. The method was first developed by Kaur[216] for the formation of CdS films and is well-known. Films deposit on any surfaces in contact with the solution while the liquor itself contains nanoparticles.

Chemical conversion reactions applied to nanoparticles having a related composition

There are two reports only, and they use different methods: Guria[217] made Cu_3SbS_3 nanorods by converting Sb_2Se_3 nanorods using $CuCl_2$. They made monodisperse rods 30 × 300 nm and up to 3 μm long and having an optical band gap of 1.04 eV. Interruption of the exchange process enabled core–shell structures to be made.

Senevirathna[218] did a double conversion–Bi_2O_3 was converted to the sulfide using aryldithioic acid and then to Cu_3BiS_3 using CuCl. This formed agglomerated particles 70–80 nm in size.

Direct mechanical milling of the ternary compound

Powderization is not popular: there are just two reports. Zhang made 5 nm particles of $CuSbS_2$.[219] Marino ball milled it down to <1 μm.[220]

Iodine vapor transport

There is a single report. $Cu_4Bi_4S_9$ was transported in iodine vapor to generate rods 10–1500 nm in diameter and 0.1–10 μm in length.[221]

Phase and shape control in nanoparticle synthesis

It is a remarkable feature of nanocrystal synthesis that the reaction conditions may be selected to reproducibly control the material's phase. Whereas for the thin film methods, phase pure materials are difficult to achieve (see above), and it has been shown repeatedly that, for example, all four phases of Cu–Sb–S can be obtained. While the earliest nanoparticle papers reported single compounds ($CuSbS_2$[222]; Cu_3SbS_3[223]; Cu_3SbS_4[224]; and $Cu_{12}Sb_4S_{13}$[225]), some later papers present the full range of systematic reaction conditions required to collect the whole set. For example, Ramasamy[226] made all four phases of Cu–Sb–S by hot injection and was able to select the product by controlling the temperature, Cu/Sb ratio and the mix of thiols used. Figure 11 shows the full set of TEM images, lattice images, and XRD patterns (this is consistent with a report by Ikeda, also for hot injection[227]).

Nanoparticles in this class of compounds express the full range of shapes that may be imagined, including spheres, bricks, sheets, wires, and stellated structures. Some synthesis conditions allow the particles to assume the crystal habits observed in nature. For example, natural deposits of chalcostibite $CuSbS_2$ resemble the nanobricks and sheets shown in Fig. 12 and reported by Zhang[229] and Ramasamy.[230] Tailoring of the reaction conditions, for example, by substituting antimony acetate for the chloride, can switch the nanoparticle's crystal habit (see Fig. 12, for example). In addition, it is possible to template structures, for example, by the use of anodic aluminium oxide, as demonstrated by the oriented columnar $CuSbS_2$ structures in Fig. 12 (lower right).

A most striking example is that of 'tetrahedrite' ($Cu_{12}Sb_4S_{13}$) named for its distinctive crystal habit, and this being replicated on the 30 nm scale as shown in Fig. 13.[213] Very often though, the shapes of the particles are not so plainly crystallographic with spheres and stellated structures are common.

Table 8. Synthesis and properties of particles: microparticles, nanoparticles, powders, micro- and nanorods, and similar structures.

Compound	Ref.	Growth technique	E_g (eV); conductivity information	Size and shape
CuSbS$_2$	Su 1999[222]	Solvothermal from CuI, SbCl$_3$ and S in ethylenediamine	...	Particles 15 nm XRD 25–90 nm TEM
	An 2003[231]	Chemical bath deposition from chlorides and thiourea with cetyltrimethylammonium bromide surfactant	...	Clusters of nanorods ~100 nm ϕ; length 0.3–4.0 μm depending on surfactant conc.
	Xu 2013[213]	Thermal decomposition of copper diethyldithiocarbamate and antimony diethyldithiocarbamate	Direct 1.20 eV Indirect 1.00 eV	...
	Zhang 2013[229]	Hot injection with Cu(acac)$_2$, Sb(Ac)$_3$, oleylamine and sulfur	...	Orthorhombic-shaped nanobricks (50–200) nm × (20–50) nm × 10 nm
	Qui 2013[232]	...	1.87 eV (sic) ~1.65 eV intercept	Particles 23.0 ± 4.9 nm
	Ikeda 2014[227]	Hot injection	1.72 eV p-type	Particles 10.5 ± 1.7 nm
	Ramasamy 2014[226]	Hot injection Cu(acac)$_2$ and SbCl$_3$ with oleylamine and sulfur	Indirect 1.1	Nanoplates (325 ± 25) × (19 ± 1) nm
	Ramasamy 2014[233]	Hot injection from Cu(acac)$_2$ and SbCl$_3$ with 1- and t-dodecanethiol	...	Regular brick shapes 1 × 8 μm
	Ikeda 2014[227]	Hot injection	1.53 eV p-type	Particles 14.3 ± 1.4
	Zou 2014[234]	Hot injection from acetates with dodecanethiol	1.59 eV	Particles 50–150 nm; morphology depends on metal stoichiometry
	Zhang 2015[235]	Solvothermal from chlorides and sulfur with ethylenediamine	...	Faceted nanoblocks with feature sizes between 200 nm and 2 μm
	Ramasamy 2015[230]	Hot injection from SbCl$_3$, Cu(acac)$_2$, and 1-oleylamine with sulfur	...	Nanoplates of varying thickness (4.3 ± 1.4 to 105 ± 5.5 nm)
	Shi 2015[189]	Solvothermal CuCl$_2$, potassium antimonyl tartrate trihydrate, sulfur + diethylenetriamine (DETA) on an anodic aluminium oxide (AAO) template	1.45 eV	With AAO: Dense columnar nanowire film, wires 200 nm ϕ and >10 μm long Without AAO: Particles 50–200 nm
	Liu 2016[236]	Hot injection	1.31 eV	Particles ~30 nm
	Shu 2016[147]	Hot injection from chlorides and sulfur in oleylamine	1.26 eV	Particles 15 nm

Continued

Table 8. Continued

Compound	Ref.	Growth technique	E_g (eV); conductivity information	Size and shape
	Zhang 2016[219]	Mechanical processing	1.36 eV direct (also 0.36 *sic*—looks like an Urbach tail)	Particles 5 nm
	Yddirim 2017[148]	Hot injection	…	Nanocrystals used to make a spun film
	Shi 2017[237]	Solvothermal using $CuCl_2$, potassium antimonyl tartrate trihydrate and thiourea	1.45 eV	Particles 250 nm
	Marino 2017[220]	Ball milled from elements	…	Particles <1 μm
	Han 2017[238]	Solvothermal using metal chlorides, mercaptoethanol, and polytheleneglycol	…	Nanobricks (30 × 70 nm) capping TiO_2 nanorods
$CuSbSe_xS_{2-x}$	Ramasamy 2017[23]	Hot injection	…	$x = 0$: 10 μm × 1 μm × 45 nm; $x = 2$: 47 μm × 4.5 μm × 50 nm
Cu_3SbS_3	Wang 2008[223]	Solvothermal from chlorides and sulfur in ethylenediamine	2.95 eV[†]	Nanowires 30 nm φ up to 3 μm long
	Zhong 2010[239]	Solvothermal from metal chlorides and L-cystine. 200 °C, 12 h	PL at 356 nm (3.48 eV)	Nanorods ~100 nm wide, several μ long
	Li 2012[240]	Solvothermal from metal chlorides and a biomolecule	…	Nanorods 100–150 nm diameter, several μm long
	Xu 2013[213]	Thermal decomposition of copper diethyldithiocarbamate and antimony diethyldithiocarbamate	Direct 1.85 eV Indirect 1.52 eV	…
	Ramasamy 2014[226]	Hot injection $Cu(acac)_2$ and $SbCl_3$ with oleylamine and sulfur	Direct 1.4 eV	Spherical particles 30 ± 5 nm
	Hao 2014[241]	Solvothermal from chlorides with thioglycolic acid	Direct 0.75–1.2 eV depending on reaction time	Particles and platelets 50 – several hundred nm
Cu_3SbS_4	van Embden[224,225]	Hot injection using chlorides with $(Me_3Si)_2S$	Indirect 0.9 eV	Spherical particles 10.2 ± 1.1 nm
	Rmasamy 2014[226]	Hot injection $Cu(acac)_2$ and $SbCl_3$ with oleylamine and sulfur	Indirect 1.2 eV	Oblate spheroids 23 ± 4 nm
	Ikeda 2014[227]	Hot injection (two steps from Cu_2S and Sb_2S_3)	0.93 eV p-type	10.8 ± 1.7 nm

Continued

Table 8. Continued

Compound	Ref.	Growth technique	E_g (eV); conductivity information	Size and shape
	Shi 2017[237]	Solvothermal using $CuCl_2$, potassium antimonyl tartrate trihydrate and thiourea	1.0 eV	Particles 200 nm
$Cu_{12}Sb_4S_{13}$	van Embden 2013[225]	Hot injection using chlorides with $(Me_3Si)_2S$	Indirect	…
			1.8 eV	6.4 nm
			1.78 eV	8.8 nm
			1.69 eV	17.8 nm
	Xu 2013[213]	Thermal decomposition of copper diethyldithiocarbamate and antimony diethyldithiocarbamate	Direct 1.24 eV Indirect 0.98 eV	Particles trigonal bipyramidal 30 nm
	Ramasamy 2014[226]	Hot injection $Cu(acac)_2$ and $SbCl_3$ with oleylamine and sulfur	Direct 1.6 eV	Hollow cubic structures 100 ± 30 nm
	Chen 2015[242]	Hot injection using acetates and 1-dodecanethiol	Tunable optical gap in the range 2.45–1.82 eV	Spheres with tuneable size in the range 2.2–15.9 nm
	Chen 2016[243]	Hot injection	Direct 1.94 eV	7.96 nm
$CuSbSe_2$	Hsiang 2016[244]	Hot injection from acetates with TEG and TEGA	Direct 1.06 eV	Irregular agglomerates and rods, morphology varies with chemistry. 50–100 nm particle size
Cu_3SbSe_3	Liu 2014[149]	Hot injection from copper acetylacetonate, antimony acetate and an alkyl ammonium selenide.	1.31 eV[†]	Spherical particles 13–18 nm
	Samanta 2015[67]	Solvothermal from $SeCl_4$, $SbCl_3$ $CuSO_4 \cdot 5H_2O$ + alkali and reducing agent	…	Particles 90 nm
	Guria 2016[217]	Conversion of Sb_2Se_3 nanorods using $CuCl_2$ in wet synthesis. Sb_2Se_3 rods formed using $SbCl_3$ and selenourea with ODA, ODE, and DDT. Interruption gives core–shell structures	1.04 eV	Monodisperse rods 30×300 nm and up to 3 μm long
$CuSbTe_2$	No known reports	…	…	…
$CuBiS_2$	No known reports	…	…	…
Cu_3BiS_3	Chen 2003[245]	CBD with $CuCl_2$, $2H_2O$, $BiCl_3$ and thiourea	…	Nanorods and whiskers 35 nm diameter and 2–15 μm long

Table 8. Continued

Compound	Ref.	Growth technique	E_g (eV); conductivity information	Size and shape
	Hu 2003[246]	CBD from chlorides and thiourea	…	Nanorod agglomerates with features 10 × 50 nm
	Shen 2003[247]	Refluxing the single-source precursors, metal diethyldithiocarbamates (i.e., the Cu- and Bi-ones together).	…	Star-like assemblies of rods, ~500 nm across with 100 nm feature sizes
	Aup-Ngoen 2011[248]	Microwave assisted solvothermal from metal chlorides and L-cystine. 200 °C, 12 h	PL peak at 367 nm (3.37 eV)	Complex branched dendritic clusters – typical rod width ~80–100 nm
	Zhong 2012[249]	Solvothermal with metal chloride and nitrate + L-cystine	PL peak at 356 nm (3.48 eV)	Stellated cluster of nanorods, 150 nm in diameter
	Yan 2012[250]	CBD from metal nitrates and thiourea with hypocrellin and other modifiers	…	Rods and stellar agglomerates rod width ~50 nm and 10 μm long.
	Zeng 2012[251]	CBD with chlorides and thiourea	1.2 eV	Complex sheet structures assembled into spheres ~4–5 μm in size
	Yan 2013[252]	Hot injection copper acetylacetonate bismuth nitrate with sulfur in oleylamine	1.56 eV photoconductive	Particles 8.9–1.9 nm
	Deng 2014[214]	Co–thermal decomposition of metal diethyl dithiocarbamates with oleylamine and/or 1-dodecanethiol and/or 1-octodecene	…	Chemistry tunes morphology from sheets (1 μm; 1.29 eV) or particles (25 nm; 1.35 eV)
	Viezbicke 2013[190]	Solvothermal from nitrates with L-cystine	1.5 eV	Particles and rods 20–500 nm length scale
	Li 2015[253]	Solvothermal from $CuCl_2$ and $Bi(NO_3)_3$	PL at 982 nm (1.25 eV)	Squat cylindrical/prism particles 250 nm ϕ × 50 nm length
	Yang 2015[254]	Thermal decomposition of carbamates $Bi(S_2CNEt_2)_3$ and $Cu(S_2CNEt_2)_2$ in a mixed solvent of oleic acid 1-octodecene	…	Particles 80 nm
	Zhou 2016[215]	Solvothermal from $CuCl_2$ and $Bi(NO_3)_3$ with L-cystine in ethylene glycol	…	Hollow nanospheres 80 nm ϕ
	Senevirathna 2017[218]	Two-step solution—Bi_2O_3 + aryldithioic acids then CuCl with microwave	…	Agglomerated particles 70–80 nm
	Du 2017[255]	Hot injection with $Cu(CH_3COO)_2$ and $Bi(NO_3)_3$ with thioacetamide and oleylamine	…	Particles 19 nm

Continued

Table 8. Continued

Compound	Ref.	Growth technique	E_g (eV); conductivity information	Size and shape
	Li 2017[256]	Hot injection: copper (II) acetylacetonate, bismuth(III) neodecanoate, in oleylamine with sulfur in oleylamine	…	Nanorods ~10×40 nm
	Aup-Ngoen, 2017[257]	Hydrothermal and solvothermal methods using L-cysteine	…	Particles indirect 0.98 eV 29.8 ± 6.3 nm to 89.6 ± 17.2 nm
	Zhong 2015[258]	CBD ('solvothermal') from $CuSO_4$ and $BiCl_3$ with thiourea	…	Complex nanosheet assemblies with sheet thickness ~40 nm
	Gao 2016[259]	CBD from chlorides and thiourea	…	Complex nanosheet assemblies up to 3 µm ϕ
$Cu_4Bi_4S_9$	Kryukova 2007[221]	I_2 vapor transport of $Cu_4Bi_4S_9$ (synthesized from Cu_2S, CuS and Bi_2S_3.	…	10–1500 nm ϕ; length 0.1–10 µm
	Li 2011[201]	Solvothermal: filaments or ribbons controlled by dodecylamine linker	1.14 eV for 8 nm particles	Filaments up to 10 µm long and ribbons 150–250 nm wide
	Li 2012[260]	Solvothermal	0.93 eV semicond. 0–140 K metallic 150–300 K	100 nm ϕ, 10 µm long
	Hu 2013[70]	Solvothermal, as Li, 2011	Semicond. $T > 270$ K $E_a = 0.761$ eV	As Li, 2011
	Deng 2014[214]	Co-thermal decomposition of metal diethyl dithiocarbamates with oleylamine and/or 1-dodecanethiol and/or 1-octodecene	0.9 eV direct	20 nm ϕ, many microns long
	Li 2014[211]	Solvothermal from chlorides with CS_2. Temp controls length.	0.83 indirect 0.93 direct	1–200 nm ϕ, up to 1 cm in length
	Liu 2014[196]	Solvothermal	0.88 eV	…
$CuBiSe_2$	No known reports	…	…	…
$CuBiTe_2$	No known reports	…	…	…

CBD—chemical bath deposition.
DDT—1-dodecanethiol.
DETA—diethylenetriamine.
ODA—octadecylamine.
ODE—1-octadecene.
TEG—triethelene glycol.
TEGA—triethylenetetramine.
†Bandgap value is unreliable.

Table 9. Summary of reports of the synthesis of nanoparticles of the Cu–Sb and Cu–Bi chalcogenides, indicating which have been made using the most popular methods, and which remain to be synthesized by any method. The sulfides of both the antimony and the bismuth compounds are the most completely studied, but nanoparticles of $CuBiS_2$ and $Cu_{12}Bi_4S_{13}$ remain to be synthesized. No compound in the series $CuBiX_2$, where X is a chalcogen, has been produced in nanoparticle form, and none of the tellurides of either the Sb or the Bi compounds has been made. Similarly, only two of the selenides have been produced as nanoparticles.

	Hot injection			Solvothermal		
	S	Se	Te	S	Se	Te
$CuSbX_2$	□	□	†	□	×	†
Cu_3SbX_3	□	□	†	□	□	†
Cu_3SbX_4	□	†	†	□	†	†
$Cu_{12}Sb_4X_{13}$	□	†	†	×	†	†
$CuBiX_2$	†	†	†	†	†	†
Cu_3BiX_3	□	†	†	□	†	†
Cu_3BiX_4	□	†	†	×	†	†
$Cu_4Bi_4X_9$	×	†	†	□	†	†
$Cu_{12}Bi_4X_{13}$	†	†	†	†	†	†

□ Synthesized by this method.
× Not synthesized by this method.
† Has not been reported by any method.

PV devices—predictions of performance, design of devices, and technological status

Predictions of solar cell performance

There are several encouraging reports of predictions of the PCEs that should be achievable with compounds in the series, and these go above and beyond simply stating that the band gaps are appropriate. A summary is as follows:

(i) $CuSbS_2$ and $CuSbSe_2$: Yu et al.[261] improve on the Shockley–Queisser estimate of efficiency by including recombination and optical absorption losses–the so-called spectroscopically limited maximum efficiency (SLME). They estimate maxima for $CuSbS_2$ (23%) and $CuSbSe_2$ (27%)–see also review by Ganose.[262] Tablero[207] gives a higher estimate for $CuSbS_2$, with radiationless recombination suppressed, but it is not so realistic.

(ii) Ternaries $CuSb(Se_{1-x}Te_x)_2$ and $CuBi(S_{1-x}Se_x)_2$: Chen and Persson[203] predict performance of the quaternary alloys $CuSb(Se_{1-x}Te_x)_2$ and $CuBi(S_{1-x}Se_x)_2$ having determined their band gaps and optical absorption spectra using DFT with HSE06. The direct gaps decrease with increasing x as expected and the PCEs were determined as a function of the composition and thickness of the absorber layers. For $CuSb(Se_{1-x}Te_x)_2$, the direct gap decreased from 1.43 to 1.07 eV as x was varied from 0 to 1, while the maximum efficiency peaked at 28.3% for x = 0.75 (thickness = 200 nm). For the same thickness of $CuBi(S_{1-x}Se_x)_2$, the gap decreased from 1.30 to 1.07 eV while the efficiency increased from 20.3% to a peak for x = 1 at 24.3%. Auger losses were predicted to reduce these values by ~4% for heavily doped samples. The authors point out that since these compounds are highly absorbing, devices with absorbers in the range 50–200 nm should be viable.

(iii) Cu_3SbS_3: Tablero[263] estimates the high concentration performance of isoelectronically doped Cu_3SbS_3:O to be >40%, and in another publication[264] ~43%; isoelectronic doping with O may help. The model is similar to that in Ref. 265.

(iv) $CuBiS_2$: In a model with radiationless recombination suppressed, Tablero[207] predicts efficiencies of ~40% under AM1.5 illumination, which is unrealistic of course.

(v) Cu_3BiS_3: Mesa[266] reports a wxAMPS[267] model of a Cu_3BiS_3 device giving V_{oc} = 0.712 V, J_{sc} = 36.25 mA/cm^2, FF = 79.54%, and efficiency = 19.86%. The heterostructure partner is not named.

Device architectures

The most widely used device architectures used for these chalcogenides are now described:

'Substrate' and 'superstrate' (with comparison to normal and inverted as used in organic PV)

The two most commonly used device architectures for thin film PV are shown in Fig. 14. Both have been used for $CuSbS_2$ and the related compounds.

In the 'substrate' design (as used for CIGS), the films are deposited on an opaque substrate, in the sequence: opaque substrate/p-absorber/n-window/n-type transparent electrode (light enters through the latter). In the 'superstrate' design (as used for CdTe), the light enters through the glass and the design is named for its orientation in service. The n-type transparent electrode layers (transparent conducting oxides or TCOs) are deposited on the glass, followed by the n-type window, and the p-type absorber and its metallization. Hence the two differ in their relationship to the support glass, rather than in the sequence of layers, which is the same in both. For reference, this sequence–TCO/n-type/p-type/metal–is referred to in the organic PV community as the 'inverted' design, with the analogues of p-type being 'hole selective' or 'anode layer' and the n-type being 'electron selective' or 'cathode layer'.
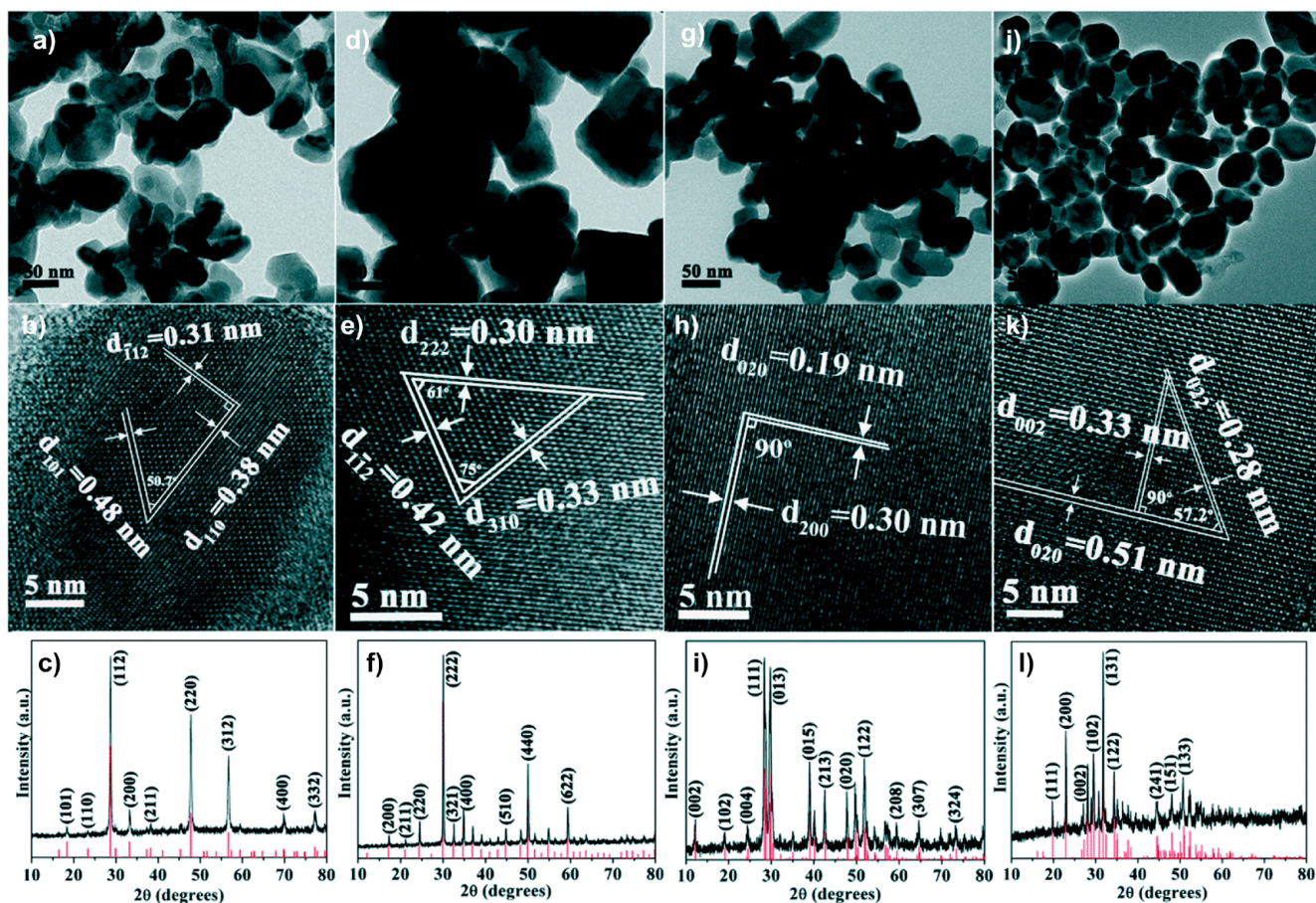
Figure 11. Nanoparticles of the full set of Cu–Sb–S phases that have been selectively synthesized by the hot injection method. Phase control was achieved by selection of the temperature, Cu/Sb ratio, and the mixture of thiols used.[228] Left to right by columns: (a–c) Cu_3SbS_4, (d–f) $Cu_{12}Sb_4S_{13}$, (g–i) $CuSbS_2$, and (j–l) Cu_3SbS_3. Top row—bright field TEM images, middle row—HRTEM lattice images, bottom row—XRD patterns. The XRD and the HRTEM confirm the phase purity of the nanoparticles. This quality is not achievable for thin film synthesis of the same materials. Figure from Liang et al., 2016[228] with permission from the Royal Society of Chemistry.

DSSC-like solar cells using nanoparticles

There is a large sub-genre of the PV literature in which the ruthenium dye in DSSCs is replaced by some other substance. For almost all absorber choices, these devices perform less well than the dye in Gratzel's original design. The single exception is 'perovskites' for which there has been both global publicity and efficiencies greater than 20%. All the others fail to outperform standard DSSC devices, including those few that use $CuSbS_2$. For example, Ramasamy's cell[233] achieved ~3%–far less than the 10–11% achieved for conventional DSSC. Han's[238] DSSC device with $CuSbS_2$ has the novelty that the electrolyte hole transporter is based on polysulfides rather than the more usual I^-/I_3^-. In a rare report of any kind of working device from Cu_3BiS_3, Yin[268] reports 1.28% (I_2/KI with Pt sensitized electrode). Overall there is no evidence at present to suggest that the use of this family of compounds in DSSC-like geometries will achieve high efficiency devices.

Device results by absorber type

Table 10 shows the device performance results for every device made from the whole class of compounds at the time of writing and listed in the order of absorber type.

These have been measured on small area contacts, typically ~0.1 cm², this being typical for technologies in development and somewhat less than the 1 cm² minimum required for verifiable performance records. For these small devices, the errors in efficiency measurement may be expected to be greater than the ±0.2% or so expected for standardized test data.

Devices with $CuSbS_2$ absorbers (including difficulties with using n-CdS window layers)

The three highest performing $CuSbS_2$ PV devices have efficiencies of between 3.1 and 3.2% making them identical within experimental error: Ikeda,[154,269] Choi,[144] and Banu.[146]

Those of Ikeda and Banu share the same 'substrate' device geometry and will be discussed first. Since the performances are
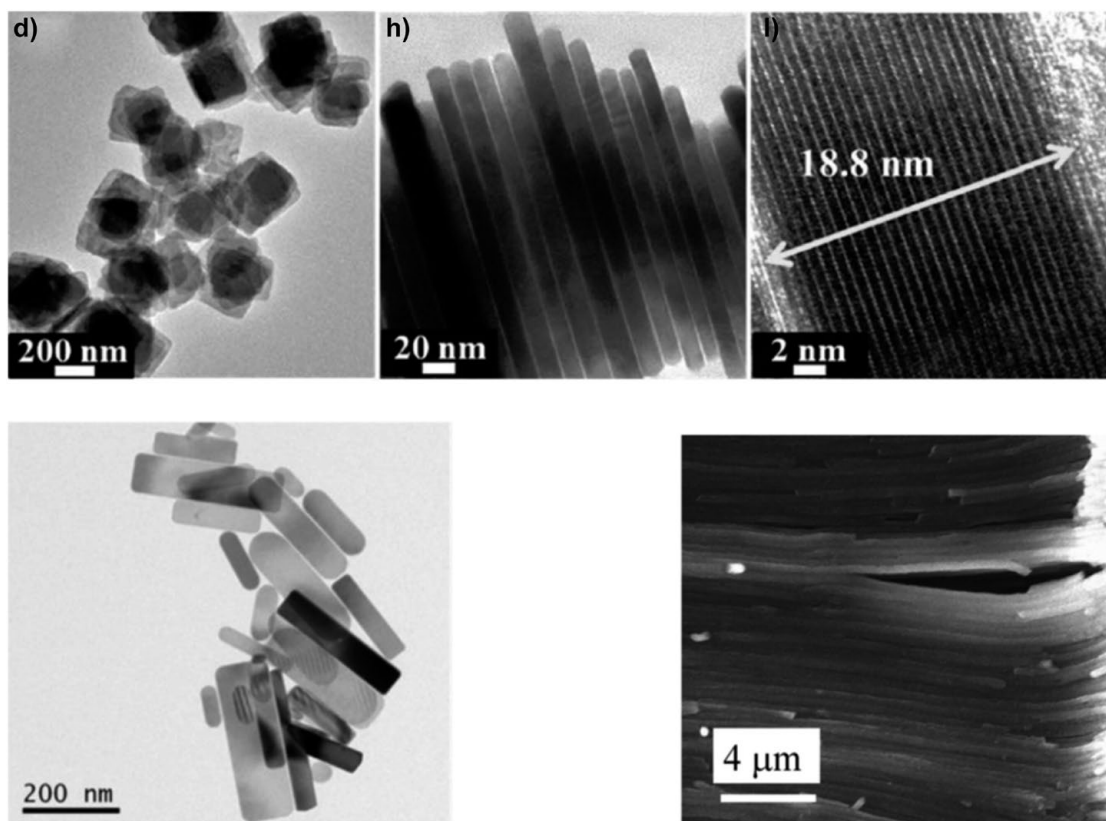
Figure 12. Nanoparticle shapes achievable for CuSbS$_2$ grown under different conditions. Top row: d, h, and l from the original figure in Ref. 230 showing top, side, and HRTEM views of CuSbS$_2$ nanoplates grown by hot injection from SbCl$_3$, Cu(acac)$_2$ and 1-oleylamine with sulfur. Reproduced with permission from Ref. 230 originally published by the Royal Society of Chemistry. Bottom left: CuSbS$_2$ 'nanobricks' formed by hot injection with copper acetylacetonate (Cu(acac)$_2$), antimony acetate (Sb(Ac)$_3$), oleylamine and sulfur. From Zhang 2013[229] originally published by ESG, Belgrade. Bottom right: CuSbS$_2$ nanowires grown on an anodic oxide template using the solvothermal method from CuCl$_2$, potassium antimonyl tartrate trihydrate, sulfur + diethylenetriamine. The template has encouraged the oriented growth. From Shi, 2015[189] with permission from Elsevier.

comparable, there is no obvious advantage in the use of one deposition technique over the other (H$_2$S sulfurization of metals or sulfurization of spun metal acetates). However, the conversion efficiencies are low and have not been bettered. The shortfall lies in the low J_{sc} values–there is current loss in these devices. The V_{oc} and FF values are respectable for prototype devices, but the current–normally the easiest parameter to increase–is low. Indeed, the deficit in J_{sc} is reflected in the experimental external quantum efficiency (EQE) curves (see Fig. 15). Most authors show curves similar to the one in Fig. 15: there is a (relatively low) peak at about 520 nm–its left flank corresponds to the onset of absorption by the CdS window layer (its band gap corresponds to about 510 nm). In common with the CdTe/CdS solar cell, this absorption is parasitic and does not contribute to the photocurrent. As expected, there is no photocurrent above 830 nm, the band gap of CuSbS$_2$. Between the peak and 830 nm, the EQE is diminished, and this has been attributed to recombination losses in the absorber itself.[270]

Further confirmation of the optical loss due to CdS window layers may be seen by comparison with the EQE curves reported

for cell designs that do not contain it. For example, Choi's cell[144] (Fig. 16) has a DSSC design in which the light enters through coated glass and TiO$_2$ (there is no CdS). Accordingly, the EQE values hold up between 450 nm and the lower limit of ~325 nm (the onset of absorption in the glass and the transparent electrode).

There is a further complication from using CdS: of the 24 reports of CdS/CuSbS$_2$ devices, half have the 'substrate' and half the 'superstrate' design. However, the 'substrate' ones outperform the 'superstrate' ones with 92% of the former and only 33% of the latter exceeding 1% efficiency. This difference is caused by diffusion of Cu into the CdS–in 'substrate' cells, the CdS is an overlayer, while in 'superstrate' ones, it is buried beneath the CuSbS$_2$ and therefore susceptible to diffusion during thermal processing. Cu is known to poison CdS by introducing a deep hole trap[271]–it is the same effect that made the extensive development of the Cu$_x$S–CdS device fail in the 1980s.

Evaluation of the band line-ups for CdS with CuSbS$_2$[179] indicates a sharp 'cliff-like' step which Lucas[179] points out is linked to high levels of recombination and low V_{oc}. Indeed,
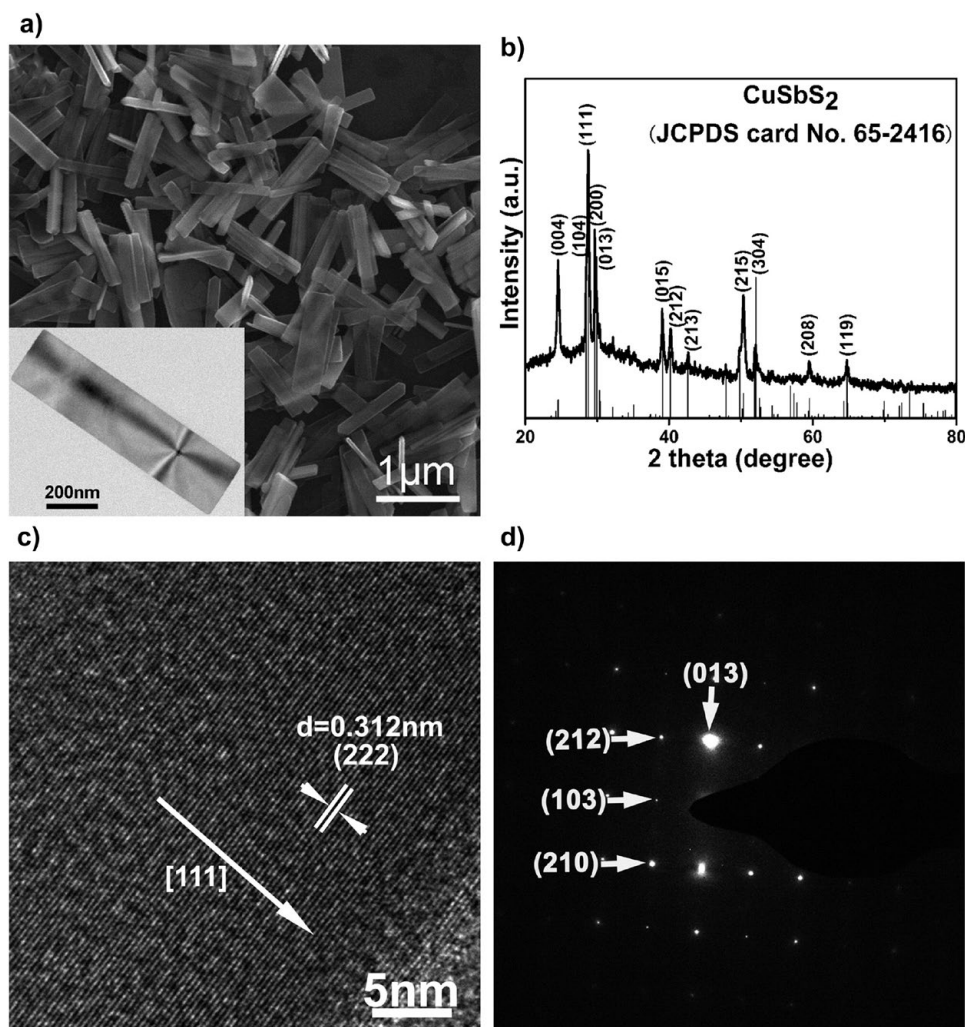
Figure 13. Nanoparticles of $Cu_{12}Sb_4S_{13}$ ('tetrahedrite') synthesized by thermal decomposition of copper diethyldithiocarbamate and antimony diethyldithiocarbamate. (a) Bright field TEM—the tetrahedra characteristic of macroscopic mineral deposits are clearly visible on the 30 nm scale, (b) confirmation of the XRD crystal structure, (c) HRTEM confirming the d_{220} and d_{222} interplanar spacings, and (d) transmission electron diffraction pattern of the assembly. Reprinted with permission from Xu et al., 2013.[213] Copyright (2013) American Chemical Society.

temperature-dependent measurements gave a 0 K value of V_{oc} = 0.7 V, which is smaller than for mainstream thin film technologies. Lucas concludes that CdS is unlikely to be a good heterojunction partner for $CuSbS_2$.

However, efforts to replace the CdS in conventional planar devices with alternative window layers have not met with success: Peccerillo[152] evaluated the band line-ups with ZnS, ZnSe, and ZnTe with $CuSbS_2$ and found them to be favorable before embarking on a program of making and testing both substrate and superstrate designs of devices. The $CuSbS_2$ was formed by sulfurization of sputtered metals. The film properties were typical for the material (optical band gap 1.45 eV, p = 1.5–3.5 × 10^{17} cm^{-3}, mobility 6–13 cm^2/(V s), resistivity 2–4 Ω cm). Spurious above-gap photoluminescence was identified by XPS as being due to oxides and efforts were made to remove any Sb_2O_3 by etching.

The result was that none of the trial devices achieved efficiencies greater than the CdS device, i.e., none exceeded ~1%.

Lucas[179] focused on making improvements to the $CuSbS_2$ absorber layer itself by thermal treatment in the presence of Sb_2S_3 which was effective in protecting against both Sb and S loss and phase decomposition. This had the effect of increasing the carrier lifetime from 0.5 to 0.7 ns. There was a concomitant rise in V_{oc} from 121 to 350 mV, but the low value of J_{sc} was still the limiting factor (up to 5.20 from 3.31 mA/cm^2) and hence the efficiency increased from 0.113 to 1.02%.

This is a common research outcome for $CuSbS_2$: many authors give credible accounts of efforts to improve the material preparation (film growth, second phase elimination) and device fabrication, only for their work to hit a rather low ceiling (1 or 2%) in device efficiency. Despite their being 20–30 published accounts
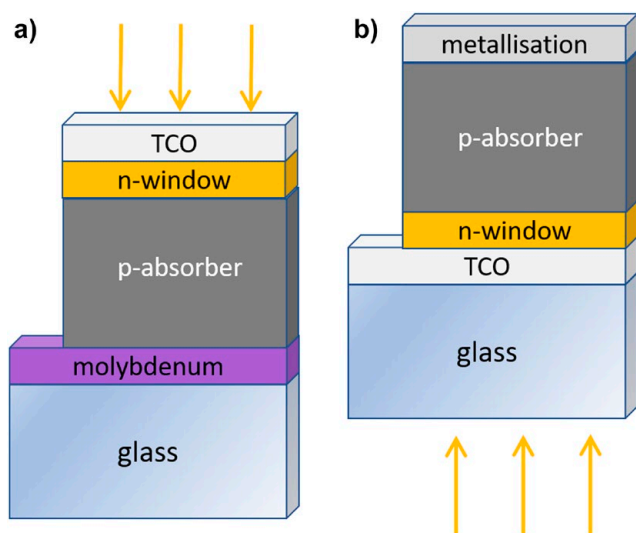
Figure 14. Thin film PV device designs. (a) 'Substrate' design used for CIGS and CZTS and (b) the 'superstrate' design used industrially for CdTe. The two designs uphold the same sequence of films, i.e., TCO/n-type/p-type/contact, and differ only in their relationship to the support glass: for 'substrate' cells, the light passes only thought the TCO and the window layer, whereas for 'superstrate' cells, the light also passes through the glass. For reference, the sequence of layers in the figures is commensurate with the so-called 'inverted' design used in organic PVs. Both types of device configuration have been used for copper antimony sulfide-based solar cells.

of devices, few provide evidence of the physical mechanisms that are so evidently limiting the performance. In particular, with the exception of Lucas,[179] there are no published reports of carrier lifetime (e.g., time resolved photoluminescence), none of the energies and capture cross sections of the carrier trapping levels that mediate recombination (e.g., by deep level transient spectroscopy) and none of direct measurements of the electrical junction position [e.g., by electron beam induced current (EBIC)]. Each of these could provide some insight into how to improve the device performance. There are some insights to be gained by comparison with $CuSbSe_2$ (see below), but overall it may only be said that $CuSbS_2$ is a difficult material and that progress in developing its PV devices has hit a roadblock.

Devices with Cu_3SbS_3, Cu_3SbS_4, and $Cu_{12}Sb_4S_{12}$ absorbers

There is one report for each of these three compounds: Cu_3SbS_3,[26] Cu_3SbS_4,[65] and $Cu_{12}Sb_4S_{12}$.[141] Only Cu_3SbS_4 comes close to performance at the 0.5% level, and the other compounds lag behind by a factor of ten at least. Presumably similar problems to those of $CuSbS_2$ (above) are compounded by the paucity of studies.

Devices with $CuSbSe_2$ and $CuSb(Se,S)_2$

While the band gap of $CuSbSe_2$ (1.1 eV) is lower than that of $CuSbS_2$ (1.49 eV), it is still in the peak region of the Shockley–Queisser performance/band gap curve, and despite there being

few reports of devices, progress has been relatively rapid. Having developed a co-sputtering route for 1% $CuSbS_2$ cells (using MoO_x back contacts), Welch[270] translated the same growth conditions and structure to $CuSbSe_2$ directly and obtained ~3% efficiency–the $J–V$ and EQE results for both structures are compared in Fig. 17. The enhanced current collection in the Se-device is seen in the differences between the EQE curves–that for $CuSbSe_2$ is extended in wavelength due to the lower band gap and is also higher. Welch[180] attributes the sharp peak in EQE for both devices as corresponding to generation and drift collection in the depletion region of the device itself. $C–V$ measurements indicate that the depletion region itself is narrow (135 nm at zero bias). To the right of the peak, the EQE is diminished by recombination, i.e., carrier diffusion is limited by short diffusion lengths and short minority carrier lifetimes. Indeed, the lifetimes were measured for $CuSbSe_2$ as $\tau_e = 190$ ps (using optical pump Terahertz probe spectroscopy–OPTP at 805 nm). This is short in comparison to mainstream thin film semiconductors for which ns timescales are more common. Further insight to the factors limiting device performance were obtained using a combinatorial experiment in which the ratio of Cu_2Se and Sb_2Se_3 supplied to the substrate varied with position, allowing the effects of composition on device performance to be systematically explored–as shown in Fig. 18. Slightly Cu-poor compositions work best, and there is a dramatic drop-off in performance as the Cu-rich threshold is crossed. Moreover, while this material is expected to be highly conductive (see section "Formation and properties of bulk, thin film and nanoparticle materials"), the local flux ratio $[Sb_2Se_3]/[Cu_2Se]$ has been shown to control the carrier density by manipulating the population of V_{Cu}. So, while the photocurrents obtained are limited by the narrow depletion regions, when the depletion region is expanded by decreasing the carrier density, this has the unwanted effect of reducing the band bending and hence reducing V_{oc}. The reviewer speculates that expansion of the field region by adopting a p–i–n junction may be necessary to increase performance more effectively.

Both the direct comparison between $CuSbS_2$ and $CuSbSe_2$ devices,[270] and the fact that the selenide has achieved higher efficiencies with five times fewer papers imply that $CuSbSe_2$ has some advantage. Recombination appears to be lessened. However, comparison of the limited studies of minority carrier lifetimes ($\tau_e = 190$ ps–selenide; $\tau_e = 500$–700 ps–sulfide), would suggest that the sulfide should give superior performance–but this has not been achieved at present. Further lifetime measurements and device fabrication would be necessary to clear up this point.

Yang[142] provides the only report to date of a mixed sulfoselenide device, with 4% S, and achieved 2.7%. Its voltage and current were comparable to the best $CuSbSe_2$ ones, but it was let down by a poor fill factor (36%) and a high reverse bias leakage current (i.e., low R_{shunt}–value not reported). Improving the material integrity would allow this to be improved upon. It would be valuable to explore a wider range of compositions of $CuSb(S,Se)_2$ so as to determine whether the voltage–current combination could be optimized, and whether there are any systematic variations in recombination behavior.

Table 10. Solar PV devices from the Cu–(Sb,Bi)–(S,Se,Te) materials family.

Reference	Structure	Configuration	Absorber deposition technique	η (%)	V_{oc} (mV)	J_{sc} (mA/cm^2)	FF (%)
CuSbS$_2$							
Rodriguez 2005[275]	Glass/SnO$_2$/CdS/Sb$_2$S$_3$/ CuSbS$_2$/Ag	Superstrate p–i–n	From CBD CuS and Sb$_2$S$_3$	0.017%	345	0.2	25
Manoclache 2005, 2007[168–170]	Glass/FTO/TiO$_2$/ TiO$_2$(porous)/ CuSbS$_2$/Au	Superstrate	Spray pyrolysis	Rectifying but not photoactive			
Manolache 2007[174]	Glass/FTO/TiO$_2$/CuSbS$_2$/ graphite	Superstrate	Spray pyrolysis	nr	90	nr	28.6
Dutta 2007[276]	Glass/FTO/In$_2$S$_3$/CuSbS$_2$/ graphite NB. This paper reports trials of various window layers, but none gave photoactive devices.	Superstrate	Spray pyrolysis	nr	210	$J_{sc} = 8.13 \times 10^{-2}$ mA	31.8
Ikeda 2013; Septina 2014[154,269]	Glass/Mo/CuSbS$_2$/CdS/ ZnO:Al	Substrate	H$_2$S sulfurization of metal precursor	3.1%	490	14.73	44
Ornelas 2014[139]	Glass/FTO/CdS/ CuSbS$_2$/C/Ag	Superstrate	Reaction of Sb$_2$S$_3$ and Cu	0.26%	294	1.55	57
Rastogi 2014[165]	Glass/FTO/ZnO/CuSbS$_2$/Ag	...	Electrodeposition	0	0	0	0
Yang 2014[137]	FTO/CuSbS$_2$/CdS/ZnO/ ZnO:Al/Au	...	Spin coating	0.5%	440	3.65	31
Ramasamy 2014[233]	In a DSSC configuration with CuSbS$_2$ in place of the dye and in the Pt-electrode position	DSSC	Hot injection from Cu(acac)$_2$ and SbCl$_3$ with 1- and t-dodecanethiol	2.61%	709	6.765	54.9
Ornelas 2015[140]	Glass/FTO/CdS/CuSbS$_2$/ Ag reaction at 350 °C works best	Superstrate	Sb$_2$S$_3$ + Cu reaction	0.44%	327	3.77	47
Al-Saab 2015[187]	TCO/CdS/CuSbS$_2$/Mo	Superstrate	Sputtering from single source	0.007%	90	0.07	25
Choi 2015[144]	Glass/FTO/compact TiO$_2$/ mesoporous TiO$_2$/ CuSbS$_2$/PCPDTBT/Au	Superstrate	Spun-on CBD	3.1%	304	21.5	46.8
Suehiro 2015[277]	Glass/ITO/ZnO/CdS/ CuSbS$_2$ NC/Au	Superstrate	Spin coating	0.01%	220	0.16	26

Continued

Table 10. Continued

Reference	Structure	Configuration	Absorber deposition technique	η (%)	V_{oc} (mV)	J_{sc} (mA/cm^2)	FF (%)
Peccerillo 2015[155]	Glass/Mo/CuSbS$_2$/CdS/i-ZnO/ITO	Substrate	Sulfurization of metal precursor	1%	120	3.1	25
Wan 2015[112]	Mo/CuSbS$_2$/CdS/ZnO/ZnO:Al/Au	Substrate	Two-stage co-evaporation	1.9%	526	9.57	37.4
Welch 2015[270]	Glass/Mo/MoO$_x$/CuSbS$_2$/CdS/i-ZnO/AZO/Al	Substrate	Co-sputtering of the binaries	~1%	~380	~10	~30
Welch 2016[278]	Glass/Mo/CuSbS$_2$/CdS/i-ZnO/ZnO:Al/Al	Substrate	Co-sputtering	0.86%	309	8.91	31
Liu 2016[236]	ITO/ZnO NR/CuSbS$_2$/P3HT/Pt	...	SILAR formation of CuS and Sb$_2$S$_3$ intermediate	1.61%	491	5.87	56
Banu 2016[146]	Glass/Mo/CuSbS$_2$/CdS/i-ZnO/n-ZnO/Al	Substrate	Spin coating of metal acetates then sulfurization	3.22%	470	15.64	43.56
Lucas 2016[179]	Glass/Mo/CuSSb$_2$/CdS/i-ZnO/AZO	Substrate	Co-sputtered from Cu$_2$S and Sb$_2$S$_3$ then annealed with Sb$_2$S$_3$ vapor and etched with KOH. The post growth treatments improve performance	1.02%	350	5.20	55
Chen 2016[181]	Glass/Mo/TiN/p-CuSbS$_2$/n-In$_{0.3}$Ga$_{0.7}$N/ITO/Ag glass/Mo/TiN/p-CuSbS$_2$/n-CdS/n-ZnO/ITO/Ag	Substrate	Co-sputtered from Cu and Sb$_2$S$_3$	0.76%	251	8.58	31
				0.16%	120	5.14	27
Marcias 2017[279]	Glass/SnO$_2$:F/CdS/Sb$_2$S$_3$/CuSbS$_2$/C:Ag	Superstrate	Chemical bath	0.66%	382	5.32	32
Vinayakumar 2017[192]	Glass/FTO/CdS/CuSbS$_2$/Ag	Superstrate	Sb$_2$S$_3$ + Cu reaction, with RTP	0.6%	665	1.35	62
Riha 2017[188]	Glass/ITO/TiO$_2$/CuSbS$_2$/Au	Superstrate	ALD from H$_2$S and bis(*N,N'*-disecbutyl acetamidinato) dicopper(I) (CuAMD) and tris(dimethylamido) antimony(III) (SbTDMA)	0.0023%	29	0.0463	30.22
	Glass/ITO/TiO$_2$/CuSbS$_2$/Spiro-OMeTAD/Au			0.0219%	31	0.04	30.70

Table 10. Continued

Reference	Structure	Configuration	Absorber deposition technique	η (%)	V_{oc} (mV)	J_{sc} (mA/cm^2)	FF (%)
Han 2017[238]	Pt activated electrode/ S^{2-}–S$_n^{2-}$/CuSbS$_2$ nanoparticles/TiO$_2$ nanorods/FTO/glass	Polysulfide electrolyte analogue of a DSSC device	Solvothermal using metal chlorides, mercaptoethanol and polytheleneglycol	1.51%	0.37	8.08	51
Saragih 2017[182]	Glass/Mo/TiN/CuSbS$_2$/ GaN/In$_{0.15}$Ga$_{0.85}$ N/ITO	Substrate	Co sputtered from Cu and Sb$_2$S$_3$ + sputtered nitride	2.99%	295	33.78	30
	Glass/Mo/TiN/CuSbS$_2$/ CdS/ZnO/ITO.	Substrate		0.78%	205	13.48	28

Cu$_3$SbS$_3$

Reference	Structure	Configuration	Absorber deposition technique	η (%)	V_{oc} (mV)	J_{sc} (mA/cm^2)	FF (%)
Maiello 2013[26]	Ni–Al/ITO/i-ZnO/CdS/ Cu$_3$Sb(Se$_x$S$_{1-x}$)$_3$/Mo/ Glass $x = 0.08$	Substrate	Sulfurization of sputtered metal films; CBD CdS; sputtered TCOs	Very low	3.5	1.6	nr

Cu$_3$SbS$_4$

Reference	Structure	Configuration	Absorber deposition technique	η (%)	V_{oc} (mV)	J_{sc} (mA/cm^2)	FF (%)
Franzer 2014[65]	Glass/FTO/CdS/ Cu$_3$SbS$_4$/Cu/Ag	Superstrate	Co-sputtering	0.45%	244	7.1	26.4

Cu$_{12}$Sb$_4$S$_{13}$

Reference	Structure	Configuration	Absorber deposition technique	η (%)	V_{oc} (mV)	J_{sc} (mA/cm^2)	FF (%)
Wang 2016[141]	Glass/FTO/ZnMgO/ Cu$_{12}$Sb$_4$S$_{13}$/gold	Superstrate	Hydrazine solution process from Cu–S and Sb–S precursor solutions	0.04%	30	7.65	24

CuSbSe$_2$

Reference	Structure	Configuration	Absorber deposition technique	η (%)	V_{oc} (mV)	J_{sc} (mA/cm^2)	FF (%)
Welch 2015[270]	Glass/Mo/MoO$_x$/CuSbSe$_2$/ CdS/i-ZnO/AZO/Al	Substrate	Co-sputtering of the binaries	~3%	344	21.9	40
Welch 2015[180]	Glass/Mo/CuSbSe$_2$/ CdS/i-ZnO/ZnO:Al/Al	Substrate	Co-sputtering of the binaries	3.12%	346	20.5	43.9
Xue 2016[14]	Glass/FTO/CuSbSe$_2$/ CdS/ZnO/ITO/Al	Substrate	Spin coating of complexes with hydrazine + annealing	1.32%	274	11.84	40.51
Yang 2017[142]	Glass/Mo/CuSb (Se$_{0.96}$S$_{0.04}$)$_2$ (950 nm)/CdS/ IZI/AZO/	Substrate	Hydrazine solution process starting from Cu$_2$S and Sb$_2$Se$_3$. Compound formed depends on temperature	2.7%	360	20.52	36.68

Table 10. Continued

Reference	Structure	Configuration	Absorber deposition technique	η (%)	V_{oc} (mV)	J_{sc} (mA/cm^2)	FF (%)
Welch 2017[212]	Glass/Mo/CuSbSe$_2$/ CdS/i-ZnO/ZnO:Al/Al as above with NaF	Substrate	Co-sputtering of the binaries	4.7%	336	26	53
				4.28%	394	19	57.1
CuBiS$_2$							
Suiyawong 2016[272]	Quantum dots with TiO$_2$ and Cu$_2$S electrode – DSSC type with polysulfide electrolyte	Quantum dot sensitized DSSC	CBD	0.62%	250	6.87	36.1
Cu$_3$BiS$_3$							
Mesa 2012[273]	Glass/Al/Cu$_3$BiS$_3$/ In$_2$S$_3$/ZnO	Substrate	Co-evaporation of metals with S effusion source	TEM study only. Absorber grains 6.5–20 nm, In$_2$S$_3$ crystalline, ZnS amorphous			
	Glass/Al/Cu$_3$BiS$_3$/ZnS/ZnO						
Mesa 2012[273]	Glass/Al/Cu$_3$BiS$_3$/ZnS or In$_2$S$_3$/ZnO	Substrate	Co-evaporation of metals with S effusion source	nr	nr	nr	nr
Yin 2014[268]	Glass/SnO$_2$:F/TiO$_2$/ Cu$_3$BiS$_3$/Pt with I$_2$–KI	Superstrate 'dye cell'	Solution growth from CuCl and Bi(NO$_3$)$_3$ in glycerol and ethanol with C$_2$H$_6$OS added in. Forms nanosheet textured coating	1.28%	448	4.5	60.8
Cu$_4$Bi$_4$S$_9$							
Liu 2013[195]	Glass/FTO/In$_2$O$_3$/In$_2$S$_3$/ Cu$_4$Bi$_4$S$_9$	Superstrate	Spin coating of Cu$_4$Bi$_4$S$_9$ nanowires	6.2%[a]	540	18	64
	Glass/FTO/ZnO/In$_2$S$_3$/ Cu$_4$Bi$_4$S$_9$			4.8%[a]	580	15	55
	Glass/FTO/TiO$_2$/In$_2$S$_3$/ Cu$_4$Bi$_4$S$_9$			5.5%[a]	520	17	62
	Glass/FTO/SnO$_2$/In$_2$S$_3$/ Cu$_4$Bi$_4$S$_9$			3.9%[a]	540	12	60
Liu 2014[196]	Glass/ITO/ZnO NW/In$_2$O$_3$/ Cu$_4$Bi$_4$S$_9$	Superstrate	Spin coating of Cu$_4$Bi$_4$S$_9$ nanowires	6.4%[a]	540	18.5	64
	Glass/ITO/ZnO NW/Cu$_4$Bi$_4$S$_9$			5.2%[a]	580	16.3	55

Table 10. Continued

Reference	Structure	Configuration	Absorber deposition technique	η (%)	V_{oc} (mV)	J_{sc} (mA/cm^2)	FF (%)
Liu 2015[150]	Glass/ITO/ZnO nanotubes/ In$_2$O$_3$/Cu$_4$Bi$_4$S$_9$	Superstrate	Spin coating of Cu$_4$Bi$_4$S$_9$ nanowires	6.8%[a]	580	18.3	64
	Glass/ITO/ZnO nanotubes/Cu$_4$Bi$_4$S$_9$			6.2%[a]	580	16.7	64
Liu 2015[197]	Glass/ITO/Zn$_2$SnO$_4$/ Cu$_4$Bi$_4$S$_9$-RGO	Superstrate	Spin coating of Cu$_4$Bi$_4$S$_9$ nanowires	2.8%[a]	630	7.2	63
	Glass/ITO/Zn$_2$SnO$_4$/ Cu$_4$Bi$_4$S$_9$			1.2%[a]	630	3.1	63
Liu 2016[198]	Glass/ITO/Zn$_2$SnO$_4$ nanoparticles/ Cu$_4$Bi$_4$S$_9$-GN	Superstrate	Spin coating of Cu$_4$Bi$_4$S$_9$ nanowires	8.6%[a]	680	18.4	69
	Glass/ITO/Zn$_2$SnO$_4$ nanoparticles/ Cu$_4$Bi$_4$S$_9$			1.3%[a]	640	3.3	61
Liu 2016[199]	Glass/ITO/ZnO NW/ Cu$_4$Bi$_4$S$_9$-GN	Superstrate	Spin coating of Cu$_4$Bi$_4$S$_9$ nanowires	10.9%[a]	780	19.8	71
	Glass/ITO/ZnO NW/ Cu$_4$Bi$_4$S$_9$			3.7%[a]	770	7.6	63
Wang 2016[200]	Glass/ITO/α-Fe$_2$O$_3$/ Cu$_4$Bi$_4$S$_9$	Superstrate BHJ type	Spin coating of Cu$_4$Bi$_4$S$_9$ nanowires	6.8%[a]	560	19.3	63
	Glass/ITO/α-Fe$_2$O$_3$/ Cu$_4$Bi$_4$S$_9$-RGO			3.1%[a]	560	8.8	31

BHJ—bulk heterojunction.
CBD—chemical bath deposition.
GN—graphene nanosheets.
RGO—reduced graphene oxide.
SILAR—successive ionic layer adsorption and reaction.
[a] Not verified by a test facility or another group—see text.

Devices with Cu$_3$SbSe$_3$, Cu$_{12}$Sb$_4$Se$_{13}$, and Cu–Sb–Te compounds

There are no reports to the author's knowledge.

Devices with CuBiS$_2$

There is just a single report of its use in solar cells,[272] that being for a CuBiS$_2$ quantum dot sensitized DSSC with a polysulfide electrolyte and trials of various electrode types on the liquid side. Probably, researchers are discouraged from making further devices (e.g., thin film structures) on account of the band gap of 1.61 eV, which is slightly higher than is usually sought for single junction PV. Nevertheless, this is the ideal gap for forming a tandem device with silicon (1.1 eV).

Devices with Cu$_3$BiS$_3$

Given that Cu$_3$BiS$_3$ is the second most researched compound in the family after CuSbS$_2$, and that 75% of the papers on it mention solar PV, it is a surprise that there is just one report of a working device.

Mesa reports an electron microscopy study of a substrate-geometry device, but it was not photoactive.[273] In other work, solution growth of the compound into a dye cell structure
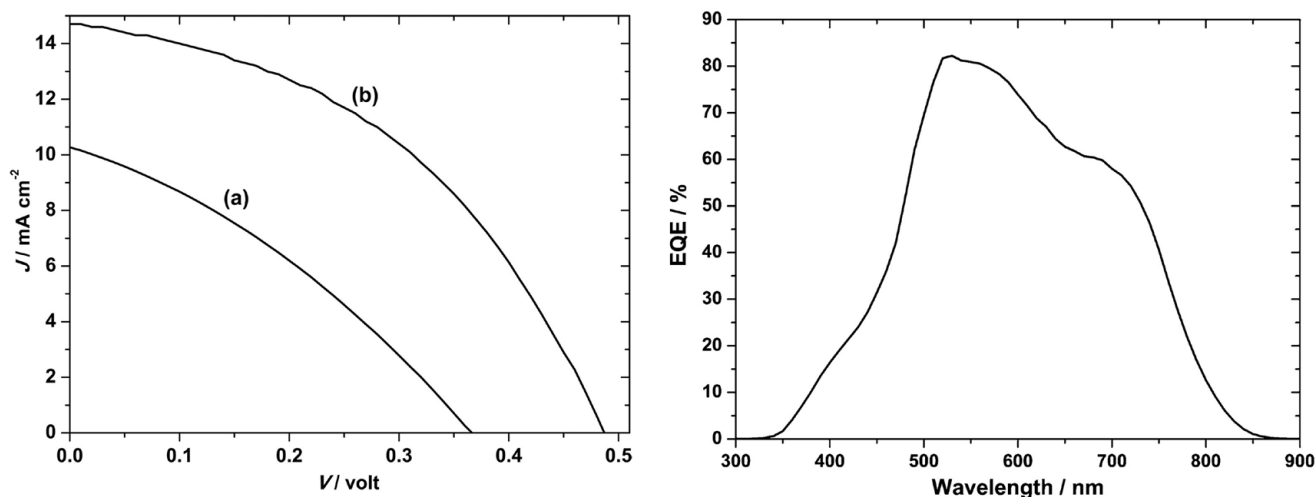
Figure 15. CuSbS$_2$ device characterization results for a substrate design glass/Mo/CuSbS$_2$/CdS/ZnO:Al solar cell. Ikeda's best device (curve b, left-hand panel)[154,269] performed with $V_{oc} = 490$ mV, $J_{sc} = 14.7$ mA cm^2, FF = 44% and had an efficiency of 3.1%. The EQE is shown in the right-hand panel. To the left of the peak at 520 nm, there is EQE loss that corresponds to parasitic absorption in the n-CdS 'window' layer. Between ~550 and 750 nm, the loss is attributed to recombination.[180] Figure from Septina, 2014[269] reproduced with permission from Elsevier.

yielded 1.28% conversion efficiency, a respectable voltage of 448 mV, an excellent fill factor (61%), but was let down by a low photocurrent of 4.5 mA/cm^2.

Further studies of the roles of heterojunctions and grain boundaries in Cu$_3$BiS$_3$ are reported by Mesa,[116] who measured the surface electronic properties of NH$_3$-cleaned Cu$_3$BiS$_3$ films and also with overlayers of CdS, ZnS, and In$_2$S$_3$ using Kelvin probe microscopy and surface photovoltage measurements. While the grain boundaries in the Cu$_3$BiS$_3$ itself were found to be positively charged, a different behavior was seen when there was an over-layer of either CdS or In$_2$S$_3$ (but not ZnS): the more positive work function at the positions of the grain boundaries in the underlying Cu$_3$BiS$_3$ was taken as evidence that the over-layers changed the grain boundary charge state from negative to positive. Further contact potential difference (CPD) measurement[117] of grain boundary positions in clean and CdS-coated Cu$_3$BiS$_3$ was interpreted using Seto's grain boundary model.[274] For Cu$_3$BiS$_3$, they found the bulk p-type carrier concentration to be 3.86×10^{16} cm^{-3} with the grain boundary charge density (p-type) being 4.19×10^{11} cm^{-2} (reduced CPD at the grain boundaries). For the CdS over-layer, the bulk carrier concentration was found to be 2.9×10^{16} cm^{-3} with the grain boundary charge density (negative) being 3.2×10^{11} cm^{-2} (increased CPD at the grain boundaries). Overall, the authors considered CdS and In$_2$S$_3$ as being able to invert the charge of underlying grain boundaries, but ZnS not.

The papers do not speculate on the reason for the zero and low device efficiencies reported. Fundamental experimental studies of the carrier lifetimes and of deep levels are absent from the literature. Certainly, devices from this material should be explored more thoroughly–its band gap of 1.40 eV should attract more interest. It is speculated anecdotally that

further labs may have attempted to make devices but did not report them due to their very low performance. This is one instance where the reporting of negative results would have been useful to form an overview of the potential of Cu$_3$BiS$_3$ in PV.

Devices with Cu$_4$Bi$_4$S$_9$

Crystallographic studies of Cu$_4$Bi$_4$S$_9$ confirm it as a bona-fide phase even though it has no recorded Sb analogue. It has a thin film band gap of 1.14 eV, or 0.96 eV as the average reported for nanoparticles. This puts it at the low end of the Shockley–Queisser curve but it is potentially viable for PV applications. It appears to be readily produced in nanowire form (see above), and Liu and co-workers at Henan University, China, have exploited this by forming spun nanowire films to produce a remarkable set of device results[150,195-200]–but not without stirring some controversy. The papers give clear accounts of the formation of 'superstrate' style devices, mostly grown on ITO-glass, and with some on FTO-glass. A wide range of intermediate layers were introduced between the TCO and the Cu$_4$Bi$_4$S$_9$ nanowire film. These include In$_2$O$_3$, In$_2$S$_3$, ZnO nanowires, Zn$_2$SnO$_4$, and α-Fe$_2$O$_3$. The Cu$_4$Bi$_4$S$_9$ nanowire film itself was variously infiltrated with reduced graphene oxide or else graphene nanosheets. The evolution of the devices has been rationalized with energy diagrams describing a cascade of electron (conduction band) levels from the absorber through the various intermediate layers. As shown in Table 10, the device results are remarkable and reach 10.9% for the glass/ITO/ZnO NW/Cu$_4$Bi$_4$S$_9$-GN substrate geometry device shown in Fig. 19.

Criticism has arisen for several reasons. First, the V_{oc} achieved (780 mV) is 70–80% of the band gap value, comparable to the
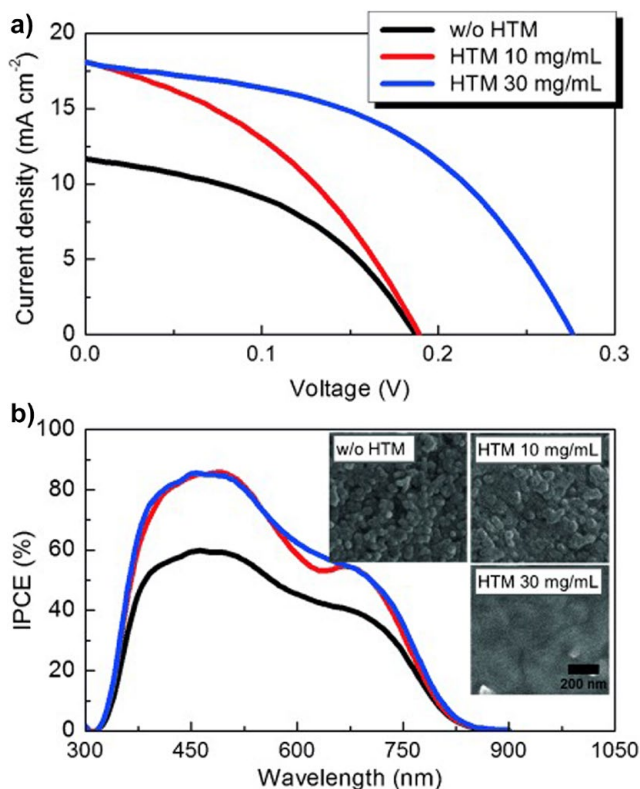
Figure 17. A comparison of similar 'substrate' geometry $CuSbS_2$ and $CuSbSe_2$ devices. Welch[270] optimized a co-sputtered $CuSbS_2$ device and then created a $CuSbSe_2$ under similar conditions for comparison. There is a significant difference in current collection, with the lower gap of the selenide (1.1 eV) extending the collection beyond that of the sulfide (1.45 eV). Both show a sharp peak in EQE attributed to drift of carriers excited in a narrow depletion region. However, the EQE on the right flank is higher for the selenide, implying that the recombination losses in the sulfide are higher. The structure is glass/Mo/MoO$_x$/CuSbS$_2$/CdS/i-ZnO/AZO/Al (and its Se analogue). Figure from Welch, 2015,[270] with permission from IEEE.

Figure 16. Device performance results for a DSSC design of $CuSbS_2$ solar cell comprising glass/FTO/compact TiO_2/mesoporous TiO_2/CuSbS$_2$/PCPDTBT/Au.[144] (a) The best device performed with V_{oc} = 304 mV, J_{sc} = 21.5 mA.cm^2, FF = 47% and had an efficiency of 3.1%. (b) Since this design has no CdS window layer, the EQE (here called 'incident PCE') holds up below 500 nm and the current is raised to 21.5 mA/cm^2 from the lower level of 15–16 mA cm^2 reported for conventional heterojunction devices with CdS. Figure from Choi, 2015.[144] Reproduced with permission from John Wiley.

best GaAs, even though the open network of $Cu_4Bi_4S_9$ nanowires may be expected to give low shunt and high series resistances that make this voltage unlikely. Second, the data presented in the papers is unusual in that there are few *J-V* curves shown, and the photoresponse spectra are not shown in the conventional units of EQE. Third, only one group has achieved these results, and the papers do not report any independent testing. As is usual for any new technology in PVs, repetition of the device by another group and verification of the device performance result by an accredited test center would be helpful in this case. Until these actions are complete, unfortunately these results will be met with skepticism.

Devices with $Cu_{12}Bi_4S_{13}$ and all other Cu–Bi–Se and Te compounds

There are no published reports to the author's knowledge.

Summary of device performance achievements to date

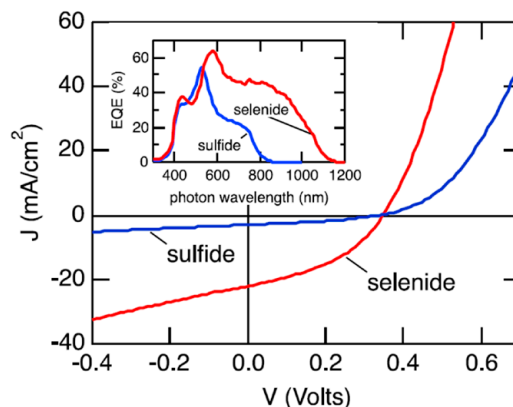Table 10 gives a comprehensive overview of all device results published at the time of writing.

Of the dozen or so compounds in the family with potential to be PV absorber materials, it is remarkable how few have been tested and demonstrated to function in laboratory-scale devices. From these, the most successful to date has been $CuSbS_2$–$CuSbSe_2$, with there being several independent reports of each having achieved efficiencies of greater than 3%. The high points are 3.22% for $CuSbS_2$[146] and 4.7% for $CuSbSe_2$.[212] Devices having the 'substrate' configuration (Fig. 14) in which the CdS window layer is not buried beneath the absorber, perform better–presumably since the CdS is not poisoned by Cu diffusion. Also, devices having CdS window layers are optically limited since absorption in the CdS does not generate carriers that are collected by the junction.

Devices have been made from Cu_3SbS_3, Cu_3SbS_4, $Cu_{12}Sb_4S_{13}$, and $CuBiS_2$, but they struggle to reach 0.5% PCE. While Cu_3BiS_3 is the second most researched material in the whole family, there is one single report of a working device made from it. This is a 'dye cell' type device having an I_2–KI electrolyte–it achieved 1.28%.[268] Within the context of research that seeks to improve on the original dye cell design by replacing the ruthenium-based dye with another absorber, the result is unremarkable: the original design achieves efficiencies of >10% and this does not represent an improvement. Conventional structures should be investigated. Finally, the apparently impressive results of up to 10.9% reported for $Cu_4Bi_4S_9$[199] are not generally considered to be reliable and would certainly need to be verified in order for this to be confirmed as a significant direction for future research.
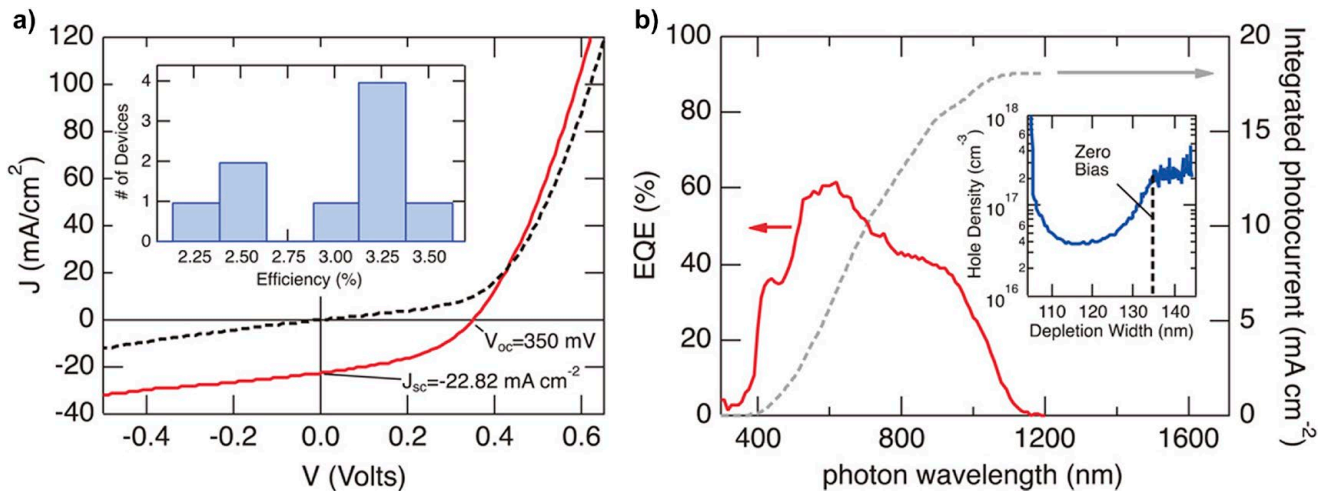
Figure 18. CuSbSe$_2$ (a) device results and (b) EQE for material formed in a combinatorial experiment by co-sputtering Cu$_2$Se and Sb$_2$Se$_3$.[180] The highest performance was Cu-poor material, with Cu-rich material causing a significant drop-off in performance. Figures reproduced from Welch et al, 2015[180] with permission from the Japan Society of Applied Physics. Copyright 2017 The Japan Society of Applied Physics.

Other applications

Photocatalysis

The visible region band gaps of these compounds have generated some interest for hydrogen evolution and photoactivity tests with dyes, although there are few reports to date:

(i)   CuSbS$_2$: Reported for hydrogen generation with a CdS/Pt partner layer.[156]

(ii) CuBiS$_2$: Photodegradation of dyes demonstrated for SiO$_2$ nanospheres coated with TiO$_2$ and with an outer layer of CuBiS$_2$.[280-282]

(iii) Cu$_3$BiS$_3$: Hydrogen evolution under AM1.5 illumination was demonstrated for a Pt–In$_2$S$_3$/Cu$_3$BiS$_3$ electrode combined with a Pt electrode.[163]

Thermoelectrics

Since these compounds have mixed van der Waals and co-valent bonding, they have the potential for the high electrical and low thermal conductivity required for maximization of the dimensionless figure of merit (ZT) that indicates high thermoelectric performance. The highest ZT reported was for Cu$_{12}$Sb$_{(4-x)}$Bi$_{(x)}$S$_{13}$ (x = 0.2) ZT = 0.84,[27] which is within the range of values reported for the classic thermoelectric, Bi$_2$S$_3$ (0.8–1), but reports for other materials in the family fall short of this–they are not prime candidates for thermoelectric applications. A summary is as follows:

(i)   CuSbS$_2$: Gudelli's theoretical evaluation[205] suggests that p-type will perform better than n-type, which is just as well since it is naturally p-type. Further theory from Alsaleh[283] highlights the role of interlayer coupling in thermal conductivity and also for CuSbSe$_2$.

(ii) CuSbSe$_2$: Zhang[88] increased ZT by a factor of 1.6 at 623 K, from 0.25 to 0.41 by introducing a small fraction of Cu$_3$SbSe$_4$ which acts to tune the conductivity since it affects both the carrier concentration and mobility.

(iii) Cu$_3$SbSe$_3$: Kirkham[89] reports a minimum in thermal conductivity at 423–448 K of 0.3 W/(m K), associated with an order–disorder transformation. See later work by Samanta below. For nanoparticles, Samanta[67] reports a thermal conductivity ~2.04 W/(m K) at 300 K reducing to 1.9 W/(m K) above 380 K where there is an order–disorder transformation and anharmonic behavior begins. Wei[90] reports ZT ~0.25 at 650 K; Liu[84] reports 0.42 at 653 K and Tyagi[91] reports 0.03 at 550 K. Tyagi[92] attributes the low ZT values to low electrical conductivity.

(iv) Cu$_3$SbSe$_4$: ZT values as high as unity are reported by Li and by Skoug,[284,285] but lower values were measured by Ghanwat[123] (0.141 at 300 K) and Tyagi[91] (0.3 at 550 K).

(v)   CuBiS$_2$: theoretical evaluation puts ZT at ~0.5.[286]

(vi) Cu$_{12}$Sb$_4$S$_{13}$: Wang[85] found ZT to be maximum at 600 K at 0.52.

(vii) Cu$_{12}$Sb$_{(4-x)}$Bi$_{(x)}$S$_{13}$: Kumar used solid state reaction to prepare compositions with x = 0, 0.2, 0.4, 0.6, and 0.8.[27] Higher concentrations of bismuth increased the electrical resistivity. The highest ZT was 0.84 at 673 K for x = 0.2 and this was attributed to the low thermal conductivity of this composition [1.17 W/(m K)].

Medical and thermo-therapeutic

Since Cu, Bi, and S are nontoxic, Cu$_3$BiS$_3$ is the most widely investigated member of the family of compounds to be investigated for medical applications.
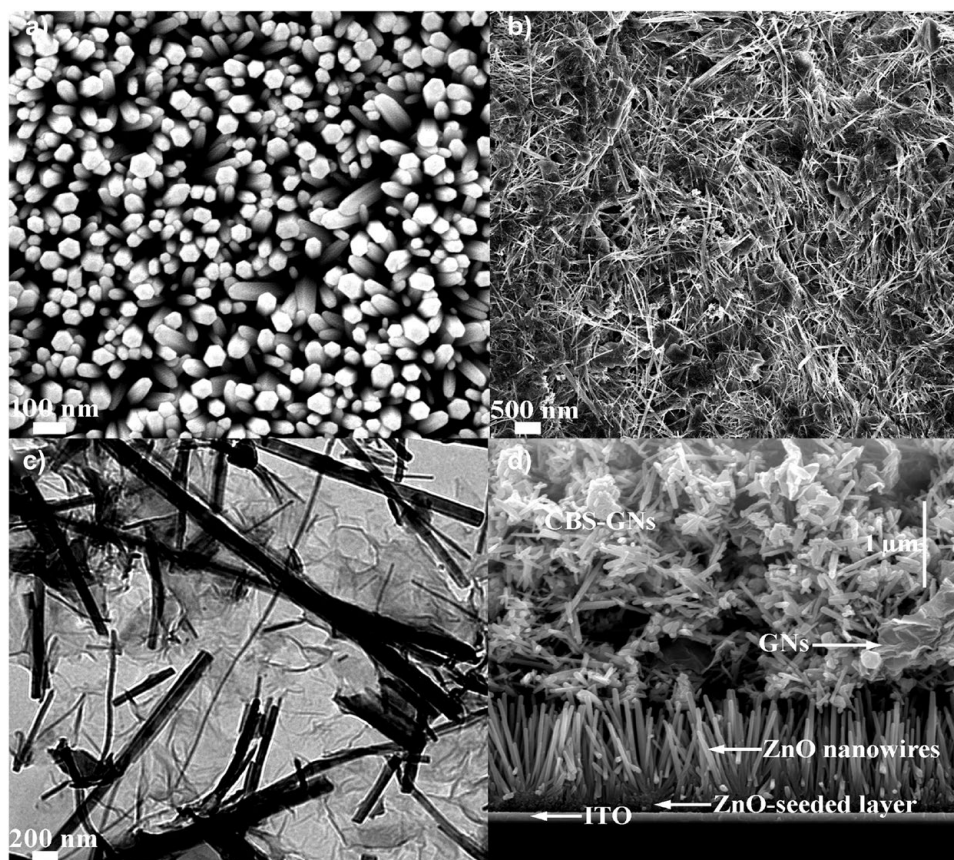
Figure 19. A 'superstrate' cell comprising a $Cu_4Bi_4S_9$ (CBS in the figure) nanowire absorber loaded with graphene nanoplates, i.e., glass/ITO/ZnO NW/$Cu_4Bi_4S_9$-GN. The authors claim 10.9% efficiency, V_{oc} = 780 mV, J_{sc} = 19.8 mA/cm^2, and a fill factor of 71%, but not without stirring some controversy. (a) ZnO nanowires, (b and c) $Cu_4Bi_4S_9$ + graphene SEM and TEM, and (d) cross section of the device structure. Figure from Liu et al, 2016;[199] used in accordance with the Creative Commons Attribution (CC BY) license (https://creativecommons.org/licenses/by/4.0/).

Its high optical absorption has seen it used in animal trials of photothermal therapy, i.e., attempts to damage cancerous structures by localized laser heating directed by concentrations of nanoparticles.[215,253,254] The ability of the heavy bismuth to provide additional contrast in X-ray computer tomographic images, and to link this to the photothermal therapy has been recognized.[215,254]

Hollow nanospheres of Cu_3BiS_3 have also been proposed for drug delivery,[215] including with functionalized coatings.[255]

Capacitors with nanomaterials

Ramasamy[230] highlights the potential importance of layered structures as supercapacitors since they may offer additional redox sites. Of the $CuSbS_2$, Cu_3SbS_3, Cu_3SbS_4, and $Cu_{12}Sb_4S_{13}$ tested, nanoparticles of $CuSbS_2$ gave the highest specific capacitance, 120 F/g with a LiOH electrolyte.

Anandraj[287] evaluated the dielectric response of Cu_3BiS_3/ polyvinylalcohol composites and concluded that they may be most suited to low frequency applications.

Battery materials

There have been attempts to use the $CuSbS_2$ nanoparticles[220,229,235] and Cu_3BiS_3 films[251] as electrodes in sodium and lithium ion batteries. The compounds may be able to intercalate the group I ions. The latter showed a first discharge capacity of 676 mA/(h g). Gao used a Cu_3BiS_3/S couple which had an initial capacity of 1343 mA/(h g), but this faded rapidly due to polysulfide dissolution. Prospects for batteries appear to be limited at present.

Conclusions and research recommendations for solar PV devices from the Cu–Sb- and Cu–Bi-chalcogenides

The following summarizes the main issues for development of this family of materials and makes specific recommendations for research targets indicated by the bullet points.

Selections of viable compounds for PVs and missing data

The family of Cu–Sb- and Cu–Bi-chalcogenides provides a rich palate of materials from which to choose potential candidates for PV device absorbers. An initial selection may be made

from the band gaps. Materials having band gaps in the range 1–1.5 eV (Table 7) include, $CuSbS_2$, Cu_3SbS_3, Cu_3SbS_4, Cu_2SbSe_2, Cu_3SbSe_3, Cu_3BiS_3, and $Cu_4Bi_4S_9$. These materials are therefore potentially viable for single junction solar cell devices according to the simple band gap criterion of the Shockley–Queisser analysis. Of these, $CuSbS_2$ and $CuSbSe_2$ have had a full "SLME" evaluation indicating their potential for PCEs of 23 and 27%, respectively. $CuSbS_2$, the most widely studied, is less efficient than is desirable. Nevertheless, it may be viable, if either a substantial fraction of the SLME efficiency can be realized, or it may be improved upon by alloying with Se, or else its specific cost ($/W_p$) is low enough to make it competitive. Materials having band gaps >1.5 eV, and which may possibly be appropriate for use in the high-gap junction of tandem cells include Cu_3SbS_3, Cu_3SbS_4, Cu_3SbSe_2, $CuBiS_2$, and $CuBiSe_2$.

(1) Materials for which the band gaps are uncertain are $CuBiS_2$ and $CuBiSe_2$–there is just one report for each. Further verification would be valuable.

(2) Materials for which the band gap has not been measured to the author's knowledge include $CuSbTe_2$, Cu_3BiS_4, $Cu_{12}Bi_4S_{13}$, Cu_3BiSe_3, Cu_3BiSe_4, and Cu_3BiTe_4.

DFT evaluations especially, and a limited number of experiments, demonstrate that many of these materials (including $CuSbS_2$ and Cu_3BiS_3) have an *indirect* rather than a *direct* transition at their lowest band gaps, and a direct transition a fraction of an eV higher. While this could be a disadvantage for PV devices, it turns out not to be: The Cu–Sb- and Cu–Bi-chalcogenides have exceptionally strong optical absorption, which exceeds both that of CIGS. Since the promotion of photogenerated carriers is efficient even for very thin films, this peculiarity of the band structures need not be a disadvantage to PV operation.

While there are many simple absorption spectra in the literature and some single wavelength refractive index measurements, there is a paucity of full optical dispersion relation measurements. Knowledge of the dispersion relations is valuable in designing multilayer structures using, for example, the optical transfer matrix method.

(3) With the exception of $CuSbS_2$, there are no experimental evaluations of the optical dispersion relations for this family of compounds. Their measurement for those compounds that are viable for PV would be valuable for use in device design and performance modeling.

Of the materials listed above as being appropriate for single-junction devices, Cu_3SbS_3 undergoes a phase change from monoclinic to orthorhombic at −9 °C. This could result in instability of a PV device during service, and since this temperature is often reached environmentally, it rules out Cu_3SbS_3 on practical grounds.

Most thin-film PV devices use p-type absorbers so as to be compatible with n-type transparent electrodes (and hence n-type window layers). For the majority of this class of materials, conductivity is indeed p-type and is dominated by V_{Cu}, as is

the case for CIGS and CZTS. Where DFT evaluations have been carried out, they confirm that V_{Cu} is the lowest energy defect, and moreover that the balance point between V_{Cu} and Cu_i controls the Fermi level to a position for which high carrier concentrations are expected. Indeed, experimental carrier densities of $p \sim 10^{18}$ cm^{-3} are frequently recorded. For $CuSbS_2$, it has been shown that Cu-poor growth is required for the highest efficiency devices, and that Cu-rich growth kills the performance–this is consistent with the model of V_{Cu} dominated conductivity. The high level of carrier concentration resulting contrasts with the case of CdTe, for example, for which p is limited to <10^{16} cm^{-3} by self-compensation. PV device designs may have to be adjusted as a result (see below). Although there is consensus on the conductivity type for most materials in the family, there are exceptions:

(4) For $CuBiS_2$ and $CuBiSe_2$, there are equal numbers of reports of n- and p-type conductivity and the conductivity type therefore remains uncertain. This should be investigated further.

Ionic conductivity has been studied in Cu_3SbS_3 and Cu_3BiS_3 and has been postulated for $CuSbS_2$. Where it occurs at operating temperatures, it will have the potential to cause ion migration and therefore instability of DC PV devices during service.

(5) Ionic conductivity and the potential for the resulting ion migration during service should be investigated at operating temperatures–it is a possible show-stopper for materials in this family under consideration for PV technologies.

PV devices

Given the extent of the literature (>300 papers), and the high fraction that invoke PV to justify their interest, surprisingly few venture so far as to make actual PV devices. The most widely investigated material, $CuSbS_2$ is mentioned in >125 papers, of which ~20 report devices. Surprisingly, for the second most investigated material, Cu_3BiS_3 only three papers report attempts to make devices from a total of >80, and only one was photoactive. Apart from the extended work on $CuSbS_2$ and $CuSbSe_2$, the other compounds in the family have been the subject of just one or two device papers each, if any. The highest efficiencies reported (Table 10) at the time of writing, for each absorber are as follows: $CuSbS_2$ 3.22%; $CuSbSe_2$ 4.77%; Cu_3SbS_3 v.low; Cu_3SbS_4 0.45%; $Cu_{12}Sb_4S_{13}$ 0.04%; $CuBiS_2$ 0.62%; Cu_3BiS_3 1.28%. Much higher efficiencies have been reported by one research group for $Cu_4Bi_4S_9$, but the results have not been independently verified and are controversial.

(6) With the exception of $CuSbS_2$ and $CuSbSe_2$, there are very few reports of PV device fabrication and testing, even though many authors invoke PV as a motivation for their work. The absence of device studies for Cu_3BiS_3 is significant since it is the second most studied material in the family. There is an opportunity for more reports of

device studies including negative results, on a wider range of compounds to demonstrate their viability or otherwise for PV.

Device studies of CuSbS$_2$ (max. efficiency 3.22%) and CuSbSe$_2$ (4.7%) provide the most insight into the evident limitations to the performance of this class of materials. The most serious outstanding issue is the low photocurrents achievable for these materials. Table 10 gives many examples of low photocurrent, and many more go unreported. To date, the cause has not been properly identified. One possibility arises from the high optical absorption and high carrier concentrations in CuSbS$_2$ and CuSbSe$_2$, which are often of the order of 10^{18} cm^{-3} or greater: this would lead to narrow depletion widths in the heterojunctions–estimated as being as low as 135 nm in CuSbSe$_2$, for example. It is possible that photogeneration of carriers does not take place close to the junction field, and that the minority carrier diffusion length is too short to enable collection. The result would be that recombination loss would limit the photocurrent, which is what happens in practice. The very few studies of minority carrier lifetime suggest that lifetimes are shorter than the values of >~2 ns reported for established thin film materials (for CuSbS$_2$–0.5-0.7 ns and for CuSbSe$_2$–0.19 ns). This indicates that recombination could be a problem, although it should be remembered that carrier lifetime measurements are notoriously susceptible to systematic errors from, for example, the influence of surfaces.

The recommendations below explore these themes:

(7) The most serious limitation to device performance for CuSbS$_2$ and related materials is the photocurrent, with J_{sc} falling far short of theoretical values. The causes of this should be investigated.

(8) Spatially resolved measurement of the junction position and width should be attempted, using EBIC measurement, for example.

(9) There are few measurements of minority carrier lifetime and none of minority carrier diffusion length in these materials even, though they are critical parameters to understand PV device performance. These should be measured experimentally.

(10) Deep level data is the subject of just one paper, for Cu$_3$BiS$_3$. Deep level transient spectroscopy or a similar method is recommended to determine whether or not killer defect states are important in these materials.

(11) Alternative junction designs may need to be considered for devices, especially p–i–n junctions that could increase the spatial extent of the collection of photogenerated carriers.

The combined research experience of CuSbS$_2$ and CuSbSe$_2$ provides some practical insights into factors that affect device performance.

First, to ensure V$_{Cu}$-driven p-type conduction, Cu-poor material is essential (Fig. 10), and this translates into device performance. More generally, control of the phase of the material and

the phase impurities is a significant issue for the whole class of materials. Formation of the ternary compounds from pairs of binaries appears to be a successful strategy. It is nevertheless possible to achieve good device results from the post-growth sulfurization of metal films for which there appears to be no distinction between sulfurization with either elemental S or H$_2$S. Clear benefits to PV device operation (increases in V_{oc} and minority carrier lifetime) have been demonstrated by stoichiometric correction by annealing in Sb$_2$S$_3$.

Comparing the performances of CuSbS$_2$ and CuSbSe$_2$, they are influenced by the band gaps: CuSbS$_2$ (1.49 eV) yields the higher voltage and lower current (V_{oc} = 470 mV, J_{sc} = 15.6 mA/cm^2) and CuSbSe$_2$ (1.12 eV) yields the lower voltage and higher current (V_{oc} = 336 mV, J_{sc} = 26 mA/cm^2). Alloying to form the solid solution may yield an optimum composition for high device performance, as has been found for CZTS and CIGS.

There are a number of reasons why CdS is a less than ideal n-type heterojunction partner for CuSbS$_2$, and presumably also for other compounds in the family: As with CdTe/CdS, light absorbed in the CdS does not contribute to the photocurrent; CdS can be poisoned by Cu-diffusion from the absorber, and while this may be lessened by using the 'substrate' rather than the 'superstrate' device geometry, it may cause stability issues; the band line-ups between CdS and the absorber may not be optimal.

Generally, the fill factors of the reported devices are low and are mostly less than 50%. Often low fill factors are caused by materials inhomogeneity, and in extreme cases, pinholes. Although it is not often reported, films of CuSbS$_S$ and Cu$_3$BiS$_3$, for example, suffer from adhesion and nonuniformity problems. Often, they display a visible texture and are prone to flake off their substrates. Material preparation by post-growth sulfurization is likely to exacerbate exfoliation by changing the unit cell size.

(12) Phase control of thin films for all materials in the class remains an issue. Scalable and reproducible protocols for phase and stoichiometry control for these materials are probably the most serious challenge to be addressed. This is important for conductivity control, the elimination of phases that could participate in recombination and to ensure materials homogeneity and integrity (e.g., adhesion).

(13) For phase control, even when the XRD spectra are monophase, photoluminescence spectra contain peaks having energies in excess of the band gap of the target phase. High resolution analytical TEM or other methods capable of identifying low volumes of unwanted phases should be deployed to determine the extent and character of phase issues.

(14) Alternative n-type heterostructure partners (i.e., alternatives to CdS) for the absorber should be sought, with higher band gaps, more optimal band line-ups, and which do not interact with the absorber to generate deep levels or else second phases. The experience with CdTe/CdS demonstrates that alternative windows such as

(ZnMg)O can provide superior device performance to the traditional favorites.

(15) Solid solutions of the S and Se analogues of the absorbers, e.g., $CuSb(S,Se)_2$, should be investigated as they may result in more optimized performance, as has been demonstrated for other multernary chalcogenides.

(16) Grain boundary passivation (section "Introduction and scope"), while possible in principle for these materials, remains a pipedream until more serious performance-limiting factors are overcome.

Nanoparticles

There is a rich literature study on the formation and properties of nanoparticles, particularly for the Cu-Sb- and Cu-Bi-*sulfides*. It is a remarkable feature of the process control that it is possible to make monophase samples of any desired phase. For example, $CuSbS_2$, Cu_3SbS_3, Cu_3SbS_4, and $Cu_{12}Sb_4S_{13}$ may each be made by controlling the process chemistry–this being in stark contrast to the experience of making thin films where parasitic phases are deeply problematic. Nevertheless, of the 27 compositions of the Cu–Sb- and Cu–Bi-chalcogenides listed in Table 9, only 9 have been synthesized in nanoparticle form. Moreover, there have been relatively few attempts to make PV devices using nanoparticles from this family of compounds. The significant exception is for $Cu_4Bi_4S_9$ for which the nanoparticle-fabricated thin film devices have achieved excellent, but controversial results.

(1) The excellent phase control offered by nanoparticle synthesis methods should be exploited in making thin-film PV devices with monophase absorbers (not least to provide demonstrations of the capability of the materials given the problems in making thin films).

(2) There is significant scope to use nanoparticles in PV devices of all kinds since there are very few reports in the literature, e.g., to exploit the physics of quantum dots, or any other nanoparticle concept.

(3) The 18 'unmade nanoparticle materials' listed in Table 9 remain to be synthesized. This includes all of the tellurides and most of the selenides.

(4) Results with $Cu_4Bi_4S_9$ should be independently verified and/or repeated by other teams.

Overall conclusion on prospects for PVs

Seven materials in the family of Cu-(Sb, Bi)-chalcogenides have band gaps in the range 1–1.5 eV making them potential candidates for the absorber materials in solar PV devices. These are as follows: $CuSbS_2$, Cu_3SbS_3, Cu_3SbS_4, Cu_3SbSe_2, Cu_3SbSe_3, Cu_3BiS_3, and $Cu_4Bi_4S_9$. They comprise elements that are sufficiently Earth abundant for them to be able to make a viable contribution to the future mass market needs for PV devices. The present day thin-film leaders CdTe and CIGS will struggle to fulfill this need due to the scarcity of tellurium and the cost of indium. However, of these materials, only $CuSbS_2$ and $CuSbSe_2$ have demonstrated credible PCEs of >3%, and none have exceeded 5%. The principal device constraint is the low generation of photocurrent. Section "Conclusions and research recommendations for solar PV devices from the Cu-Sb- and Cu-Bi-chalcogenides" of this review offers clear pointers toward missing knowledge that could help resolve this issue: the field is quite immature at this stage, and a significant step change in understanding will be required in order for the Cu-(Sb,Bi)–chalcogenides to realize their potential contribution to large scale PV power generation.

Acknowledgments

REFERENCES:

1. *BP Statistical Review of World Energy*, 67th ed., June 2018. Available at: https://www.bp.com/content/dam/bp/en/corporate/pdf/energy-economics/statistical-review/bp-stats-review-2018-full-report.pdf.

2. Peter L.: Towards sustainable photovoltaics: The search for new materials. *Philos. Trans. R. Soc., A* 369, 1840–1856 (2011).

3. Zinke R.K. and Werkheiser W.H.: U.S. Geological Survey, 2018, Mineral Commodity Summaries 2018: U.S. Geological Survey, 200 p., https://doi.org/10.3133/70194932.

4. Shockley W. and Queisser H.J.: Detailed balance limit of efficiency of pn junction solar cells. *J. Appl. Phys.* 32, 510 (1961).

5. Perniu D., Duta A., and Schoonman J.: *2006 International Semiconductor Conference*, Vol. 1 and 2 (IEEE, New York, 2007).

6. Krishnan B., Shaji S., and Ornelas R.E.: Progress in development of copper antimony sulfide thin films as an alternative material for solar energy harvesting. *J. Mater. Sci.: Mater. Electron.* 26, 4770–4781 (2015).

7. Moelo Y., Makovicky E., Mozgova N.N., Jambor J.L., Cook N., Pring A., Paar W., Nickel E.H., Graeser S., Karup-Moller S., Balic-Zunic T., Mumme W.G., Vurro F., Topa D., Bindi L., Bente K., and Shimizu M.: Sulfosalt systematics: A review. Report of the sulfosalt sub-committee of the IMA Commission on Ore Mineralogy. *Eur. J. Mineral.* 20, 7–46 (2008).

8. Lane D.W., Hutchings K.J., McCracken R., and Forbes I.: New chalcogenide materials for thin film solar cells. In *Materials Challenges: Inorganic Photovoltaic Solar Energy*, Irvine S.J.C., ed. (Royal Soc Chemistry, Cambridge, 2015); pp. 160–208.

9. Walsh A., Payne D.J., Egdell R.G., and Watson G.W.: Stereochemistry of post-transition metal oxides: Revision of the classical lone pair model. *Chem. Soc. Rev.* 40, 4455–4463 (2011).

10. Dufton J.T.R., Walsh A., Panchmatia P.M., Peter L.M., Colombara D., and Islam M.S.: Structural and electronic properties of $CuSbS_2$ and $CuBiS_2$: Potential absorber materials for thin-film solar cells. *Phys. Chem. Chem. Phys.* 14, 7229–7233 (2012).

11. Skinner B.J., Luce F.D., and Makovcky E.: Studies of sulfosalts of copper 3: Phases and phase relations in the system Cu–Sb–S. *Econ. Geol.* 67, 924 (1972).

12. Karup-Moller S.: The Cu–Sb–Se phase system at temperatures between 350° and 700 °C. *Neues Jahrb. Mineral., Abh.* 174, 277–292 (1999).

13. Wang N.D.: The Cu–Bi–S system–Results from low-temperature experiments. *Mineral. Mag.* 58, 201–204 (1994).

14. Xue D.J., Yang B., Yuan Z.K., Wang G., Liu X.S., Zhou Y., Hu L., Pan D.C., Chen S.Y., and Tang J.: $CuSbSe_2$ as a potential photovoltaic absorber material: Studies from theory to experiment. *Adv. Energy Mater.* 5, 1501203 (2015).

15. Zhou Y., Wang L., Chen S., Qin S., Liu X., Chen J., Xue D-J., Luo M., Cao Y., Cheng Y., Sargent E.H., and Tang J.: Thin-film Sb_2Se_3 photovoltaics

with oriented one-dimensional ribbons and benign grain boundaries. *Nat. Photonics* 9, 409 (2015).

16. Messier R., Giri A.P., and Roy R.A.: Revised structure zone model for thin-film physical structure. *J. Vac. Sci. Technol., A* 2, 500–503 (1984).

17. Du B.L., Zhang R.Z., Chen K., Mahajan A., and Reece M.J.: The impact of lone-pair electrons on the lattice thermal conductivity of the thermoelectric compound CuSbS$_2$. *J. Mater. Chem. A* 5, 3249–3259 (2017).

18. Takeuchi Y. and Ozawa T.: Structure of Cu$_4$Bi$_4$S$_9$. *Proc. Jpn. Acad.* 50, 751 (1974).

19. Takeuchi Y. and Ozawa T.: Structure of Cu$_4$Bi$_4$S$_9$ and its relation to structures of covellite, CuS and busmuthite Bi$_2$S$_3$. *Z. Kristallogr.* 141, 217–232 (1975).

20. Bente K. and Kupcik V.: Redetermination and refinement of the structure of tetrabismuth tetracopper ennasulfide, Cu$_4$Bi$_4$S$_9$. *Acta Crystallogr., Sect. C: Cryst. Struct. Commun.* 40, 1985–1986 (1984).

21. Razmara M.F., Henderson C.M.B., Pattrick R.A.D., Bell A.M.T., and Charnock J.M.: The crystal chemistry of the solid solution series between chalcostibite (CuSbS$_2$) and emplectite (CuBiS$_2$). *Mineral. Mag.* 61, 79–88 (1997).

22. Meyer B., Zhang S., and Scholz F.: The quantitative analysis of mixed crystals CuS$_x$Se$_{1-x}$ with abrasive stripping voltammetry and a redetermination of the solubility product of CuSe and the standard potential of the Cu/CuSe electrode. *Fresenius. J. Anal. Chem.* 356, 267–270 (1996).

23. Ramasamy K., Gupta R.K., Palchoudhury S., Ivanov S., and Gupta A.: Layer-structured copper antimony chalcogenides (CuSbSe$_x$S$_{2-x}$): Stable electrode materials for supercapacitors. *Chem. Mater.* 27, 379–386 (2015).

24. Takei K., Maeda T., and Wada T.: Crystallographic and optical properties of CuSbS$_2$ and CuSb(S$_{1-x}$Se$_x$)$_2$ solid solution. *Thin Solid Films* 582, 263–268 (2015).

25. Wada T. and Maeda T.: Optical properties and electronic structures of CuSbS$_2$, CuSbSe$_2$, and CuSb(S$_{1-x}$Se$_x$)$_2$ solid solution. In *Physica Status Solidi C: Current Topics in Solid State Physics*, Vol. 14, No. 6, Maiberg M., Franzel W., and Scheer R., eds. (Wiley-VCH Verlag Gmbh, Weinheim, 2017); p. 1600196.

26. Maiello P., Zoppi G., Miles R.W., Pearsall N., and Forbes I.: Chalcogenisation of Cu–Sb metallic precursors into Cu$_3$Sb(Se$_x$S$_{1-x}$)$_3$. *Sol. Energy Mater. Sol. Cells* 113, 186–194 (2013).

27. Kumar D.S.P., Chetty R., Femi O.E., Chattopadhyay K., Malar P., and Mallik R.C.: Thermoelectric properties of Bi doped tetrahedrite. *J. Electron. Mater.* 46, 2616–2622 (2017).

28. Mindat.org: Open database of minerals, rocks, meteorites and the localities they come from. Available at http://www.mindat.org (accessed August 23, 2018).

29. Hofmann W.: Structural and morphological correlations in ores of formula type ABC$_2$. I. The structure of wolfsbergite CuSbS$_2$ and emplektite CuBiS$_2$ and their relationships to the structure of antimonite Sb$_2$S$_3$. *Z. Kristallogr.* 84, 177–203 (1933).

30. Kyono A. and Kimata M.: Crystal structures of chalcostibite (CuSbS$_2$) and emplectite (CuBiS$_2$): Structural relationship of stereochemical activity between chalcostibite and emplectite. *Am. Mineral.* 90, 162–165 (2005).

31. McCarthy C.L., Cottingham P., Abuyen K., Schueller E.C., Culver S.P., and Brutchey R.L.: Earth abundant CuSbS$_2$ thin films solution processed from thiol–amine mixtures. *J. Mater. Chem. C* 4, 6230–6233 (2016).

32. Nespolo M. and Ferraris G.: A survey of hybrid twins in non-silicate minerals. *Eur. J. Mineral.* 21, 673–690 (2009).

33. Ungemach H. and Hebd C.R.: A remarkable deposit of chalcostibite in Morocco. *C. R. Hebd. Seances Acad. Sci.* 169, 918–919 (1919).

34. Karupmoller S. and Makovicky E.: Skinnerite, Cu$_3$SbS$_3$, a new sulfosalt from Llimaussaq alkaline intrusion, South Greenland. *Am. Mineral.* 59, 889–895 (1974).

35. Pfitzner A.: Cu$_3$BiS$_3$–Crystal structure and polymorphism. *Z. Anorg. Allg. Chem.* 620, 1992–1997 (1994).

36. Pfitzner A.: Disorder of Cu$^+$ in Cu$_3$SbS$_3$: Structural investigations of the high- and low-temperature modification. *Z. Kristallogr.* 213, 228–236 (1998).

37. Zunic T.B. and Makovicky E.: Determination of the crystal structures of α-TlPbSbS$_3$, trigonal (Tl,K)Fe$_3$(SO$_4$)$_2$(OH)$_6$ and Cu$_3$SbS$_3$ from X-ray powder diffraction data. In *Epdic 3, Pts 1 and 2: Proceedings of the 3rd European Powder Diffraction Conference*, Delhez R. and Mittemeijer E.J., eds. (Transtec Publications Ltd., Zurich-Uetikon, 1994); pp. 659–664.

38. Makovicky E. and Baliczunic T.: The crystal structure of skinnerite, P2(1)/C Cu$_3$SbS$_3$ from powder data. *Can. Mineral.* 33, 655–663 (1995).

39. Palache C., Berman H., and Frondel C.: The System of Mineralogy of James Dwight Dana and Edward Salisbury Dana, Yale University 1837–1892, Volume I: Elements, Sulfides, Sulfosalts, Oxides, 7th ed. (John Wiley and Sons, Inc., New York, 1944); pp. 433–435.

40. Lemoine P., Bourges C., Barbier T., Nassif V., Cordier S., and Guilmeau E.: High temperature neutron powder diffraction study of the Cu$_{12}$Sb$_4$S$_{13}$ and Cu$_4$Sn$_7$S$_{16}$ phases. *J. Solid State Chem.* 247, 83–89 (2017).

41. Škácha P., Sejkora J., and Plášil J.: Příbramite, CuSbSe$_2$, the Se-analogue of chalcostibite, a new mineral from Příbram. *Eur. J. Mineral.* 29, 653–661 (2017).

42. Pfitzner A.: The crystal structure of Cu$_3$SbSe$_3$ *sic* (Cu$_3$SbSe$_3$: Synthese und Kristallstruktur). *Z. Anorg. Allg. Chem.* 621, 685–688 (1995).

43. Škácha P., Sejkora J., and Bytízite P.J.: IMA 2016-044. CNMNC Newsletter No. 33, October 2016, page 1138. *Mineral. Mag.* 80, 1135–1144 (2016).

44. Fischer K.F. and Pilz K.: A method for obtaining a possibly unique (unambiguous) crystal structure solution using multiple resonant scattering data. *Acta Crystallogr., Sect. A: Found. Crystallogr.* 53, 475–483 (1997).

45. Johan Z., Picot P., Pierrot R., and Kvaček M.: A method for obtaining a possibly unique (unambiguous) crystal structure solution using multiple resonant scattering data. *Bull. Soc. Fr. Mineral.* 94, 162–165 (1971).

46. Madelung O., ed.: *Semiconductors—Basic Data*, 2nd ed. (Springer Science & Business Media, Berlin, 2012).

47. Portheine J.C. and Nowacki W.: Refinement of the crystal structure of emplectite, CuBiS$_2$. *Z. Kristallogr.* 141, 387–402 (1975).

48. Kocman V. and Nuffield E.W.: Crystal structure of wittichenite, Cu$_3$BiS$_3$. *Acta Crystallogr., Sect. B: Struct. Sci.* 29, 2528–2535 (1973).

49. Torneoka K.: The modulated structure of cubic Cu$_9$BiS$_6$. *Am. Mineral.* 67, 360–372 (1982).

50. Zeng Y.P., Li H.X., Xiang B.Y., Ma H.Q., Qu B.H., Xia M.X., Wang Y.C., Zhang Q.L., and Wang Y.G.: Synthesis and characterization of phase-purity Cu$_9$BiS$_6$ nanoplates. *Mater. Lett.* 64, 1091–1094 (2010).

51. Kodêra M., Kupcik V., and Makovicky E.: Hodrushite–A new sulphosalt. *Mineral. Mag.* 37, 641–648 (1970).

52. Topa D., Makovicky E., and Balić-Žunić T.: Crystal structures and crystal chemistry of members of the cuprobismutite homologous series of sulfosalts. *Can. Mineral.* 41, 1481–1501 (2004).

53. Forster H.J., Bindi L., and Stanley C.J.: Grundmannite, CuBiSe$_2$, the Se-analogue of emplectite, a new mineral from the El Dragon mine, Potosi, Bolivia. *Eur. J. Mineral.* 28, 467–477 (2016).

54. Makovicky E., Sotofte I., and Karup-Moller S.: The crystal structure of Cu$_4$Bi$_4$Se$_9$. *Z. Kristallogr.* 217, 597–604 (2002).

55. Paar W.H., Cooper M.A., Moelo Y., Stanley C.J., Putz H., Topa D., Roberts A.C., Stirling J., Raith J.G., and Rowe R.: Eldragonite, Cu$_6$BiSe$_4$(Se$_2$), a new mineral species from the El Dragon mine, Potosi, Bolivia, and its crystal structure. *Can. Mineral.* 50, 281–294 (2012).

56. Lind I.L. and Makovicky E.: Phase relation in the system Cu-Sb-S at 200 °C, 10^8 Pa by hydrothermal synthesis: Microprobe analyses of tetrahedrite–A warning. *Neues Jahrb. Mineral., Abh.* 145, 134–156 (1982).

57. Baker J., Kumar R.S., Sneed D., Connolly A., Zhang Y., Velisavljevic N., Paladugu J., Pravica M., Chen C.F., Cornelius A., and Zhao Y.S.: Pressure induced structural transitions in CuSbS$_2$ and CuSbSe$_2$ thermoelectric compounds. *J. Alloys Compd.* 643, 186–194 (2015).

58. Welch A.W., Zawadzki P.P., Lany S., Wolden C.A., and Zakutayev A.: Self-regulated growth and tunable properties of CuSbS$_2$ solar absorbers. *Sol. Energy Mater. Sol. Cells* 132, 499–506 (2015).

59. Craig J.R. and Lees W.R.: Thermochemical data for sulfosalt ore minerals–Formation of simple sulfides. *Econ. Geol.* 67, 373 (1972).

60. Seal R.R., Robie R.A., Barton P.B., and Hemingway B.S.: Superambient heat-capacities of synthetice stibnite, berthierite, and chalcostibite–Revised thermodynamic properties and implications for phase-equilibria. *Econ. Geol. Bull. Soc. Econ. Geol.* 87, 1911–1918 (1992).

61. Tesfeye Firdu F.T.P.: *Thermodynamics and Phase Equilibria in the (Ni, Cu, Zn)–(As, Sb, Bi)S Systems at Elevated Temperatures (300–900 °C)* (Aalto University, Aalto, Finland, 2010).

62. Whitfield H.J.: Polymorphism in skinnerite, Cu_3SbS_3. *Solid State Commun.* 33, 747–748 (1980).

63. Makovicky E.: Polymorphism in Cu_3SbS_3 and $CuBuS_3$–The ordering schemes for copper atoms and electron microscope observations. *Neues Jahrb. Mineral., Abh.* 168, 185–212 (1994).

64. Seal R.R., Essene E.J., and Kelly W.C.: Tetrahedrite and tennantite–Evaluation of thermodynamic data and phase equilibria. *Can. Mineral.* 28, 725–738 (1990).

65. Franzer N.D., Paudel N.R., Xiao C.X., and Yan Y.F.: *2014 IEEE 40th Photovoltaic Specialist Conference* (IEEE, New York, NY, 2014); pp. 2326–2328.

66. Tatsuka K. and Morimoto N.: Composition variation and polymorphism of tetrahedrite in Cu–Sb–S system below 400 °C. *Am. Mineral.* 58, 425–434 (1973).

67. Samanta K., Gupta N., Kaur H., Sharma L., Pandey S.D., Singh J., Senguttuvan T.D., Sharma N.D., and Bandyopadhyay A.K.: Order-disorder transition and Fano-interference in thermoelectric Cu_3SbSe_3 nanoparticles. *Mater. Chem. Phys.* 151, 99–104 (2015).

68. Makovicky E.: The phase-transformations and thermal-expansion of the solid electrolyte Cu_3BiS_3 between 25 °C and 300 °C. *J. Solid State Chem.* 49, 85–92 (1983).

69. Chang Y.A., Neumann J.P., and Choudary U.V.: *Phase Diagrams and Thermodynamic Properties of Ternary Copper–Sulfur–Metal Systems* (International Copper Research Association, Milwaukee, Wisconsin, 1979).

70. Hu J.Y., Li J., Zhang S.J., Zhao H.F., Zhang Q.H., Yao Y., Zhao Q., Shi L.J., Zou B.S., Li Y.C., Li X.D., Liu J., Zhu K., Liu Y.L., Jin C.Q., and Yu R.C.: Pressure-induced phase transitions in single-crystalline $Cu_4Bi_4S_9$ nanoribbons. *Chin. Phys. B* 22, 5 (2013).

71. Braga M.H., Ferreira J.A., Lopes C., and Malheiros L.F.: Phase transitions in the Cu–Sb–S system. In *Advanced Materials Forum IV*, Marques A.T., Silva A.F., Baptista A.P.M., Sa C., Alves F., Malheiros L.F., and Vieira M., eds.; Materials Science Forum, Vol. 587–588 (Trans Tech Publications Ltd., Durnten-Zurich, 2008); p. 435.

72. Cambi L. and Elli M.: Processi idrotermali, sintesi di solfosali da ossidi di metalli e metalloidi, nota II–Cuprosolfoantimoniti. *La Chimica el'Industria* 47, 136–147 (1965).

73. Chakrabarti D.J. and Laughlin D.E.: The Cu–S (copper–sulfur) system. *Bull. Alloy Phase Diagrams* 4, 254 (1983).

74. Schmidt J.A., Sagua A.E., and Lescano G.: Electrochemical investigation of the equilibria (covellite plus anilite) and (covellite plus digenite). *J. Chem. Thermodyn.* 30, 283–290 (1998).

75. Taras Bryndzia L. and Kleppa O.J.: High-temperature reaction calorimetry of solid and liquid phases inpart of the quasi-binary system Cu_2S–Sb_2S_3. *Am. Mineral.* 73, 707–713 (1988).

76. Yang C.Y., Wang Y.M., Li S.T., Wan D.Y., and Huang F.Q.: $CuSbSe_2$-assisted sintering of $CuInSe_2$ at low temperature. *J. Mater. Sci.* 47, 7085–7089 (2012).

77. Korzun B.V., Gavrilenko A.N., Fadzeyeva A.A., Ignatenko O.V., Maroz I.I., Sobol V.R., Rusu M., Klenk R., Merschjann C., Schedel-Niedrig T., and Lux-Steiner M.C.: T(x) phase diagram of the $CuSbS_2$–$CuInS_2$ system and solubility limit of Sb in $CuInS_2$. *Cryst. Res. Technol.* 48, 641–648 (2013).

78. Xiang Y., Zhang X.K., and Zhang S.: Insight into the mechanism of Sb promoted $Cu(In,Ga)Se_2$ formation. *J. Solid State Chem.* 204, 278–282 (2013).

79. Guo H.L., Cui Y., Tian Q.W., Gao S., Wang G., and Pan D.C.: Significantly enhancing grain growth in $Cu_2ZnSn(S,Se)_4$ absorber layers by insetting Sb_2S_3, $CuSbS_2$, and $NaSb_5S_8$ thin films. *Cryst. Growth Des.* 15, 771–777 (2015).

80. Wachtel A. and Noreika A.: Growth and characterisation of $CuSbS_2$ crystals. *J. Electron. Mater.* 9, 281–297 (1980).

81. Durant B. and Parkinson B.A.: Photovoltaic response of naturally occurring semiconducting sulfide minerals. In *2016 IEEE 43rd Photovoltaic Specialists Conference* (IEEE, New York, 2016); pp. 2774–2779.

82. Zhou J., Bian G.Q., Zhu Q.Y., Zhang Y., Li C.Y., and Dai J.: Solvothermal crystal growth of $CuSbQ_2$ (Q = S, Se) and the correlation between macroscopic morphology and microscopic structure. *J. Solid State Chem.* 182, 259–264 (2009).

83. Wubet W. and Kuo D.H.: Process limitation for p-type $CuSbS_2$ semiconductor with high electrical mobility of 20 $cm^2 V^{-1} s^{-1}$. *Mater. Res. Bull.* 53, 290–294 (2014).

84. Liu R., Ren G., Tan X., Lin Y., and Nan C.: Enhanced thermoelectric properties of Cu_3SbSe_3-based composites with inclusion phases. *Energies* 9, 7 (2016).

85. Wang J.Y., Gu M., Bao Y.F., Li X.Y., and Chen L.D.: Quick fabrication and thermoelectric properties of $Cu_{12}Sb_4S_{13}$ tetrahedrite. *J. Electron. Mater.* 45, 2274–2277 (2016).

86. Abdelghany A., Abdelmohsen N., Abouelela A.H., and Abdelwahab D.M.: Dielectric-relaxation study of $CuBiSe_2$ in the solid and liquid-phases. *Indian J. Pure Appl. Phys.* 28, 329–333 (1990).

87. Majsztrik P.W., Kirkham M., Garcia-Negron V., Lara-Curzio E., Skoug E.J., and Morelli D.T.: Effect of thermal processing on the microstructure and composition of Cu–Sb–Se compounds. *J. Mater. Sci.* 48, 2188–2198 (2013).

88. Zhang D., Yang J.Y., Jiang Q.H., Fu L.W., Xiao Y., Luo Y.B., and Zhou Z.W.: Ternary $CuSbSe_2$ chalcostibite: Facile synthesis, electronic-structure and thermoelectric performance enhancement. *J. Mater. Chem. A* 4, 4188–4193 (2016).

89. Kirkham M., Majsztrik P., Skoug E., Morelli D., Wang H., Porter W.D., Payzant E.A., and Lara-Curzio E.: High-temperature order/disorder transition in the thermoelectric Cu_3SbSe_3. *J. Mater. Res.* 26, 2001–2005 (2011).

90. Wei T.R., Wu C.F., Sun W., Pan Y., and Li J.F.: Is Cu_3SbSe_3 a promising thermoelectric material? *RSC Adv.* 5, 42848–42854 (2015).

91. Tyagi K., Gahtori B., Bathula S., Toutam V., Sharma S., Singh N.K., and Dhar A.: Thermoelectric and mechanical properties of spark plasma sintered Cu_3SbSe_3 and Cu_3SbSe_4: Promising thermoelectric materials. *Appl. Phys. Lett.* 105, 5 (2014).

92. Tyagi K., Gahtori B., Bathula S., Srivastava A.K., Shukla A.K., Auluck S., and Dhar A.: Thermoelectric properties of Cu_3SbSe_3 with intrinsically ultralow lattice thermal conductivity. *J. Mater. Chem. A* 2, 15829–15835 (2014).

93. Wei T-R., Li F., and Li J-F.: Transport properties and enhanced thermoelectric performance of aluminum doped Cu_3SbSe_4. *J. Electron. Mater.* 43, (2015).

94. Wubet W., Kuo D.H., and Abdullah H.: Effects of sintering temperature and duration on the structural and electrical properties of $CuBiS_2$ bulks. *J. Solid State Chem.* 230, 237–242 (2015).

95. Mariolacos K.: Single crystal synthesis of ternary mineral phases in the temperature gradient: Wittichenite, Cu_3BiS_3, dolerophanite, $CuO·CuSO_4$, bismoclite, $BiOCl$. *Neues Jahrb. Mineral., Monatsh.* 164–170 (1998).

96. Abdelmohsen N., Abdelghany A., and Sharaf K.: Thermal conductivity of $CuSbSe_2$ and $CuBiSe_2$ in the solid and liquid-state. *Phys. Chem. Liq.* 20, 131–134 (1989).

97. Abdelmohsen N., Abdelghany A., Abouelela A.H., and Abdelwahab D.M.: Electrical-conductivity and thermoelectric-power of $CuBiSe_2$ in the solid and liquid states. *Indian J. Pure Appl. Phys.* 28, 360–361 (1990).

98. Soliman L.I., Zayed H.A., El Soad A.M.A., and El Ghafar S.A.: Study of optical properties of $CuSbTe_2$, $CuSbSe_2$ and $CuSbS_2$ this (*sic*) films. *Phys. Low-Dimens. Struct.* 5-6, 31–41 (2003).

99. Soliman L.I., Aziza M., El-Soad A., Zayed H.A., and El-Ghfar S.A.: Structural and electrical properties of $CuSbTe_2$, $CuSbSe_2$ and $CuSbS_2$ chalcogenide this (*sic*) films. *Fiz. A*, 11, 139–152 (2002).

100. Rabhi A., Kanzari M., and Rezig B.: Growth and vacuum post-annealing effect on the properties of the new absorber $CuSbS_2$ thin films. *Mater. Lett.* 62, 3576–3578 (2008).

101. Rabhi A., Kanzari M., and Rezig B.: Optical and structural properties of $CuSbS_2$ thin films grown by thermal evaporation method. *Thin Solid Films* 517, 2477–2480 (2009).

102. Rabhi A. and Kanzari M.: Structural, optical and electrical properties of $CuSbS_2$ these amorphous films: Effect of thickness variation. *Chalcogenide Lett.* 8, 383–390 (2011).

103. Rabhi A. and Kanzari M.: Effect of air annealing on $CuSbS_2$ thin film grown by vacuum thermal evaporation. *Chalcogenide Lett.* 8, 255–262 (2011).

104. Fadhli Y., Rabhi A., and Kanzari M.: Effect of annealing time and substrates nature on the physical properties of $CuSbS_2$ thin films. *J. Mater. Sci.: Mater. Electron.* 25, 4767–4773 (2014).

105. Suriakarthick R., Kumar V.N., Shyju T.S., and Gopalakrishnan R.: Effect of substrate temperature on copper antimony sulphide thin films from thermal evaporation. *J. Alloys Compd.* 651, 423–433 (2015).

106. Rabhi A., Fadhli Y., and Kanzari M.: Investigation on dispersive optical constants and microstructural parameters of the absorber CuSbS$_2$ thin films. *Vacuum* 112, 59–65 (2015).

107. Hussain A., Ahmed R., Ali N., Butt F.K., Shaari A., Shamsuri W.N.W., Khenata R., Prakash D., and Verma K.D.: Post annealing effects on structural, optical and electrical properties of CuSbS$_2$ thin films fabricated by combinatorial thermal evaporation technique. *Superlattices Microstruct.* 89, 136–144 (2016).

108. Nefzi K., Rabhi A., and Kanzari M.: Investigation of physical properties and impedance spectroscopy study of Cu$_3$SbS$_3$ thin films. *J. Mater. Sci.: Mater. Electron.* 27, 1888–1896 (2016).

109. Nefzi K., Rabhi A., and Kanzari M.: Effect of substrate temperature on electrical properties of (Al/p-Cu$_3$SbS$_3$/Mo) Schottky diodes grown by vacuum thermal evaporation. *J. Mater. Sci.: Mater. Electron.* 28, 8733–8738 (2017).

110. Tiwari K.J., Vinod V., Subrahmanyam A., and Malar P.: Growth and characterization of chalcostibite CuSbSe$_2$ thin films for photovoltaic application. *Appl. Surf. Sci.* 418, 216–224 (2017).

111. Estrella V., Nair M.T.S., and Nair P.K.: Semiconducting Cu$_3$BiS$_3$ thin films formed by the solid-state reaction of CuS and bismuth thin films. *Semicond. Sci. Technol.* 18, 190–194 (2003).

112. Wan L., Ma C., Hu K., Zhou R., Mao X.L., Pan S.H., Wong L.H., and Xu J.Z.: Two-stage co-evaporated CuSbS$_2$ thin films for solar cells. *J. Alloys Compd.* 680, 182–190 (2016).

113. Dussan A., Murillo J.M., and Mesa F.: Thermally stimulated conductivity of Cu$_3$BiS$_3$ thin films deposited by co-evaporation: determination of trap parameters related to defects in the gap. *J. Mater. Sci.* 47, 6688–6692 (2012).

114. Mesa F., Dussan A., and Gordillo G.: Evidence of trapping levels and photoelectric properties of Cu$_3$BiS$_3$ thin films. *Physica B* 404, 5227–5230 (2009).

115. Mesa F., Gordillo G., Dittrich T., Ellmer K., Baier R., and Sadewasser S.: Transient surface photovoltage of p-type Cu$_3$BiS$_3$. *Appl. Phys. Lett.* 96, 3 (2010).

116. Mesa F., Chamorro W., Vallejo W., Baier R., Dittrich T., Grimm A., Lux-Steiner M.C., and Sadewasser S.: Junction formation of Cu$_3$BiS$_3$ investigated by Kelvin probe force microscopy and surface photovoltage measurements. *Beilstein J. Nanotechnol.* 3, 277–284 (2012).

117. Mesa F. and Fajardo D.: Study of heterostructures of Cu$_3$BiS$_3$-buffer layer measured by Kelvin probe force microscopy measurements (KPFM). *Can. J. Phys.* 92, 892–895 (2014).

118. Murali B., Madhuri M., and Krupanidhi S.B.: Near-infrared photoactive Cu$_3$BiS$_3$ thin films by co-evaporation. *J. Appl. Phys.* 115, 8 (2014).

119. Muthukannan A., Prema P., Henry J., Mohanraj K., and Sivakumar G.: Photosensitivity of CuBiSe$_2$ thin film deposited by vacuum evaporation technique. *J. Chin. Chem. Soc.* 63, 841–846 (2016).

120. Nair M.T.S., Rodriguez-Lazcano Y., Pena Y., Messina S., Campos J., and Nair P.K.: Absorber films of antimony chalcogenides via chemical deposition for photovoltaic application. In *Materials for Photovoltaics*, Durstock M., Friedman D., Gaudiana R., and Rockett A., eds. (Materials Research Society, Warrendale, 2005); pp. 167–172.

121. Ezugwu S.C., Ezema F.I., and Asogwa P.U.: Synthesis and characterisation of ternary CuSbS$_2$ thin films: The effect of deposition time. *Chalcogenide Lett.* 7, 369–376 (2010).

122. Rodriguez-Lazcano Y., Nair M.T.S., and Nair P.K.: CuSbS$_2$ thin film formed through annealing chemically deposited Sb$_2$S$_3$–CuS thin films. *J. Cryst. Growth* 223, 399–406 (2001).

123. Ghanwat V.B., Mali S.S., Kharade S.D., Pawar N.B., Patil S.V., Mane R.M., Patil P.S., Hong C.K., and Bhosale P.N.: Microwave assisted synthesis, characterization and thermoelectric properties of nanocrystalline copper antimony selenide thin films. *RSC Adv.* 4, 51632–51639 (2014).

124. Chen G.L., Wang W.H., Zhao J.F., Yang W.Y., Chen S.Y., Huang Z.G., Jian R.K., and Ruan H.R.: Study on the synthesis and formation mechanism of flower-like Cu$_3$SbS$_4$ particles via microwave irradiation. *J. Alloys Compd.* 679, 218–224 (2016).

125. Sutrave D.S., Shahane G.S., Dargad J.S., and Deshmukh L.P.: Electrical transport properties of chemically prepared CuBiS$_2$ thin films. *Indian J. Pure Appl. Phys.* 34, 506–508 (1996).

126. Sonawane P.S., Wani P.A., Patil L.A., and Seth T.: Growth of CuBiS$_2$ thin films by chemical bath deposition technique from an acidic bath. *Mater. Chem. Phys.* 84, 221–227 (2004).

127. Balasubramanian V., Suriyanarayanan N., Prabahar S., and Srikanth S.: Structural and optical properties of chemically deposited CuBiS$_2$ thin films. *Chalcogenide Lett.* 8, 637–648 (2011).

128. Balasubramanian V., Suriyanarayanan N., Prabahar S., Srikanth S., and Ravi P.: Temperature- and time-dependent Hall effect studies on chemically deposited CuBiS$_2$ thin films. *Optoelectron. Adv. Mater., Rapid Commun.* 6, 104–106 (2012).

129. Deshmukh S.G., Panchal A.K., and Vipul K.: Chemical bath deposition of C$_3$BiS$_3$ thin films. In *International Conference on Condensed Matter and Applied Physics*, Shekhawat M.S., Bhardwaj S., and Suthar B., eds. (Amer Inst Physics, Melville, 2016); p. 020023.

130. Bari R.H. and Patil L.A.: Preparation and characterization of nanostructured copper bismuth diselenide thin films from a chemical route. *Bull. Mater. Sci.* 33, 663–670 (2010).

131. Nair M.T.S., Nair P.K., Garcia V.M., Pena Y., Arenas I.K., Garcia J.C., and GomezDaza O.: *Chemically Deposited Thin Films of Sulfides and Selenides of Antimony and Bismuth as Solar Energy Materials* (SPIE-International Society Optical Engineering, Bellingham, 1997).

132. Hussain A., Ahmed R., Ali N., Shaari A., Luo J.T., and Fu Y.Q.: Characterization of Cu$_3$SbS$_3$ thin films grown by thermally diffusing Cu$_2$S and Sb$_2$S$_3$ layers. *Surf. Coat. Technol.* 319, 294–300 (2017).

133. Nair M.T.S., Pena Y., Campos J., Garcia V.M., and Nair P.K.: Chemically deposited Sb$_2$S$_3$ and Sb$_2$S$_3$–CuS thin films. *J. Electrochem. Soc.* 145, 2113–2120 (1998).

134. Hu H., Gomez-Daza O., and Nair P.K.: Screen-printed Cu$_3$BiS$_3$–polyacrylic acid composite coatings. *J. Mater. Res.* 13, 2453–2456 (1998).

135. Hussain A., Ahmed R., Ali N., Abdel-Salam N.M., bin Deraman K., and Fu Y.Q.: Synthesis and characterization of thermally evaporated copper bismuth sulphide thin films. *Surf. Coat. Technol.* 320, 404–408 (2017).

136. Nair P.K., Huang L., Nair M.T.S., Hu H.L., Meyers E.A., and Zingaro R.A.: Formation of p-type Cu$_3$BiS$_3$ absorber thin films by annealing chemically deposited Bi$_2$S$_3$–CuS thin films. *J. Mater. Res.* 12, 651–656 (1997).

137. Yang B., Wang L., Han J., Zhou Y., Song H.B., Chen S.Y., Zhong J., Lv L., Niu D.M., and Tang J.: CuSbS$_2$ as a promising earth-abundant photovoltaic absorber material: A combined theoretical and experimental study. *Chem. Mater.* 26, 3135–3143 (2014).

138. Garza C., Shaji S., Arato A., Tijerina E.P., Castillo G.A., Das Roy T.K., and Krishnan B.: p-Type CuSbS$_2$ thin films by thermal diffusion of copper into Sb$_2$S$_3$. *Sol. Energy Mater. Sol. Cells* 95, 2001–2005 (2011).

139. Ornelas-Acosta R.E., Avellaneda D., Shaji S., Castillo G.A., Roy T.K., and Krishnan B.: CuSbS$_2$ thin films by heating Sb$_2$S$_3$/Cu layers for PV applications. *J. Mater. Sci.: Mater. Electron.* 25, 4356–4362 (2014).

140. Ornelas-Acosta R.E., Shaji S., Avellaneda D., Castillo G.A., Das Roy T.K., and Krishnan B.: Thin films of copper antimony sulfide: A photovoltaic absorber material. *Mater. Res. Bull.* 61, 215–225 (2015).

141. Wang L., Yang B., Xia Z., Leng M.Y., Zhou Y., Xue D.J., Zhong J., Gao L., Song H.S., and Tang J.: Synthesis and characterization of hydrazine solution processed Cu$_{12}$Sb$_4$S$_{13}$ film. *Sol. Energy Mater. Sol. Cells* 144, 33–39 (2016).

142. Yang B., Wang C., Yuan Z.K., Chen S.Y., He Y.S., Song H.B., Ding R.Q., Zhao Y., and Tang J.: Hydrazine solution processed CuSbSe$_2$: Temperature dependent phase and crystal orientation evolution. *Sol. Energy Mater. Sol. Cells* 168, 112–118 (2017).

143. Tian Q.W., Wang G., Zhao W.G., Chen Y.Y., Yang Y.C., Huang L.J., and Pan D.C.: Versatile and low-toxic solution approach to binary, ternary, and quaternary metal sulfide thin films and its application in Cu$_2$ZnSn(S,Se)$_4$ solar cells. *Chem. Mater.* 26, 3098–3103 (2014).

144. Choi Y.C., Yeom E.J., Ahn T.K., and Seok S.I.: CuSbS$_2$-sensitized inorganic–organic heterojunction solar cells fabricated using a metal–thiourea complex solution. *Angew. Chem., Int. Ed.* 54, 4005–4009 (2015).

145. Rath T., MacLachlan A.J., Brown M.D., and Hague S.A.: Structural, optical and charge generation properties of chalcostibite and tetrahedrite copper antimony sulfide thin films prepared from metal xanthates. *J. Mater. Chem. A* 3, 24155–24162 (2015).

146. Banu S., Ahn S.J., Ahn S.K., Yoon K., and Cho A.: Fabrication and characterization of cost-efficient CuSbS₂ thin film solar cells using hybrid inks. *Sol. Energy Mater. Sol. Cells* 151, 14–23 (2016).

147. Shu B. and Han Q.: Studies on structural, optical and electrical properties of CuSbS₂ nanoparticles. *Chalcogenide Lett.* 13, 46–53 (2016).

148. Yddirim M., Aljabour A., Sarilmaz A., and Ozel F.: Investigation of optical framework of chalcostibite nanocrystal thin films: An insight into refractive index dispersion, optical band gap and single-oscillator parameters. *J. Alloys Compd.* 722, 420–426 (2017).

149. Liu Y.K., Yang J., Gu E.N., Cao T.T., Su Z.H., Jiang L.X., Yan C., Hao X.J., Liu F.Y., and Liu Y.X.: Colloidal synthesis and characterisation of Cu₃SbSe₃ nanocrystals. *J. Mater. Chem. A* 2, 6363–6367 (2014).

150. Liu X.Y., Cheng X.Y., Wang S., Zhang K., and Gu Y.Z.: Transport of photogenerated charges and photoelectric properties in two types of heterostructures with different ZnO microstructures. *Phys. Chem. Chem. Phys.* 17, 17041–17052 (2015).

151. Colombara D.: Investigation of chalcogenide absorber materials for photovoltaic applications. Ph.D. thesis, Department of Chemistry, University of Bath, U.K., 2012.

152. Peccerillo E.: CuSbS₂ and related chalcogenides for sustainable photovoltaics. Ph.D. thesis, Department of Physics, University of Liverpool, U.K. 2015.

153. Colombara D., Peter L.M., Rogers K.D., and Hutchings K.: Thermochemical and kinetic aspects of the sulfurization of Cu–Sb and Cu–Bi thin films. *J. Solid State Chem.* 186, 36–46 (2012).

154. Ikeda S., Iga Y., Septina W., Harada T., and Matsumura M.: CuSbS₂-based thin film solar cells prepared from electrodeposited metallic stacks composed of Cu and Sb layers. In *2013 IEEE 39th Photovoltaic Specialists Conference* (IEEE, New York, 2013); pp. 2598–2601.

155. Peccerillo E., Major J., Phillips L., Treharne R., Whittles T.J., Dhanak V., Halliday D., and Durose K., *IEEE, 2014 IEEE 40th Photovoltaic Specialist Conference* (PVSC, New York, NY, 2014); pp. 257–260.

156. Zhang L., Li Y.B., Li X., Li C.L., Zhang R.J., Delaunay J.J., and Zhu H.W.: Solution-processed CuSbS₂ thin film: A promising earth-abundant photocathode for efficient visible-light-driven hydrogen evolution. *Nano Energy* 28, 135–142 (2016).

157. Maiello P., Zoppi G., Miles R., Pearsall N., and Forbes I.: *The 7th Photovoltaic Science Applications and Technology Conference and Exhibition (PVSAT-7), the Solar Energy Society* (Heriot Watt University, Edinburgh, 2011); p. 229.

158. Cho A., Banu S., Kim K., Park J.H., Yun J.H., Cho J.S., and Yoo J.: Selective thin film synthesis of copper–antimony–sulfide using hybrid ink. *Sol. Energy* 145, 42–51 (2017).

159. Colombara D., Peter L.M., Rogers K.D., Painter J.D., and Roncallo S.: Formation of CuSbS₂ and CuSbSe₂ thin films via chalcogenisation of Sb–Cu metal precursors. *Thin Solid Films* 519, 7438–7443 (2011).

160. Gerein N.J. and Haber J.A.: Physical vapor deposition synthesis of Cu₃BiS₃ for application in thin film photovoltaics. In *Thin-Film Compound Semiconductor Photovoltaics*, Shafarman W., Gessert T., Niki S., and Siebentritt S., eds. (Materials Research Society, Warrendale, 2005); pp. 119–124.

161. Gerein N.J. and Haber J.A.: Cu₃BiS₃, Cu₃BiS₄, Ga₃BiS₃, and Cu₅Ga₂BiS₈ as potential solar absorbers for thin film photovoltaics. In *Conference Record of the Thirty-First IEEE Photovoltaic Specialists Conference–2005* (IEEE, New York, 2005); pp. 159–162.

162. Colombara D., Peter L.M., Hutchings K., Rogers K.D., Schafer S., Dufton J.T.R., and Islam M.S.: Formation of Cu₃BiS₃ thin films via sulfurization of Bi–Cu metal precursors. *Thin Solid Films* 520, 5165–5171 (2012).

163. Kamimura S., Beppu N., Sasaki Y., Tsubota T., and Ohno T.: Platinum and indium sulfide-modified Cu₃BiS₃ photocathode for photoelectrochemical hydrogen evolution. *J. Mater. Chem. A* 5, 10450–10456 (2017).

164. Zhang L.J., Jin X., Yuan C.C., Jiang G.S., Liu W.F., and Zhu C.F.: The effect of the sulfur concentration on the phase transformation from the mixed CuO–Bi₂O₃ system to Cu₃BiS₃ during the sulfurization process. *Appl. Surf. Sci.* 389, 858–864 (2016).

165. Rastogi A.C. and Janardhana N.R.: Properties of CuSbS₂ thin films electrodeposited from ionic liquids as p-type absorber for photovoltaic solar cells. *Thin Solid Films* 565, 285–292 (2014).

166. Tang D., Yang J., Liu F.Y., Lai Y.Q., Li J., and Liu Y.X.: Growth and characterization of CuSbSe₂ thin films prepared by electrodeposition. *Electrochim. Acta* 76, 480–486 (2012).

167. Tang D., Yang J., Liu F.Y., Lai Y.Q., Jia M., Li J., and Liu Y.X.: One-step electrodeposition and annealing of CuSbSe₂ thin films. *Electrochem. Solid State Lett.* 15, D11–D13 (2012).

168. Manolache S.A., Nanu M., Duta A., Goossens A., and Schoonman J.: *CAS 2005: International Semiconductor Conference* (IEEE, New York, 2005); pp. 145–148.

169. Manolache S., Duta A., Isac L., Nanu M., Goossens A., and Schoonman J.: The influence of the precursor concentration on CuSbS₂ thin films deposited from aqueous solutions. *Thin Solid Films* 515, 5957–5960 (2007).

170. Manolache S.A., Andronic L., Duta A., and Enesca A.: The influence of the deposition condition on crystal growth and on the band gap of CuSbS₂ thin film absorber used for solid state solar cells (SSSC). *J. Optoelectron. Adv. Mater.* 9, 1269–1272 (2007).

171. Popovici I. and Duta A.: Tailoring the composition and properties of sprayed CuSbS₂ thin films by using polymeric additives. *Int. J. Photoenergy* 2012, 1–6 (2012).

172. Liu S., Chen L., Nie L., Wang X., and Yuan R.: The influence of the substrate temperature on spray-deposited CuSbS₂ thin films. *Chalcogenide Lett.* 11, 639–644 (2014).

173. Aquino J.A.R., Vela D.L.R., Shaji S., Avellaneda D.A., and Krishnan B.: Spray pyrolysed thin films of copper antimony sulfide as photovoltaic absorber. In *Physica Status Solidi C: Current Topics in Solid State Physics*, Vol. 13, No. 1, Gershon T. and Scanlon D.O., eds. (Wiley-VCH Verlag Gmbh, Weinheim, 2016); pp. 24–29.

174. Manolache S.A. and Duta A.: The influence of the spray deposition parameters in the photovoltaic response of the three-dimensional solar cell: TCO/dense TiO₂/CuSbS₂/graphite. *J. Optoelectron. Adv. Mater.* 9, 3219–3222 (2007).

175. Pawar S.H., Pawar A.J., and Bhosale P.N.: Spray pyrolytic deposition of CuBiS₂ thin-films. *Bull. Mater. Sci.* 8, 423–426 (1986).

176. Liu S., Wang X.B., Nie L.Y., Chen L., and Yuan R.: Spray pyrolysis deposition of Cu₃BiS₃ thin films. *Thin Solid Films* 585, 72–75 (2015).

177. Zakutayev A., Baranowski L.L., Welch A.W., Wolden C.A., and Toberer E.S.: *2014 IEEE 40th Photovoltaic Specialist Conference* (IEEE, New York, NY, 2014); pp. 2436–2438.

178. Lucas F.W.D., Welch A.W., Baranowski L.L., Dippo P.C., Mascaro L.H., and Zakutayev A.: Thermal treatment improvement of CuSbS₂ absorbers. In *2015 IEEE 42nd Photovoltaic Specialist Conference* (IEEE, New York, 2015).

179. Lucas F.W.D., Welch A.W., Baranowski L.L., Dippo P.C., Hempel H., Unold T., Eichberger R., Blank B., Rau U., Mascaro L.H., and Zakutayev A.: Effects of thermochemical treatment on CuSbS₂ photovoltaic absorber quality and solar cell reproducibility. *J. Phys. Chem. C* 120, 18377–18385 (2016).

180. Welch A.W., Baranowski L.L., Zawadzki P., Lany S., Wolden C.A., and Zakutayev A.: CuSbSe₂ photovoltaic devices with 3% efficiency. *Appl. Phys. Express* 8, 082301 (2015).

181. Chen W.L., Kuo D.H., and Tuan T.T.A.: Preparation of CuSbS₂ thin films by co-sputtering and solar cell devices with band gap-adjustable n-type InGaN as a substitute of ZnO. *J. Electron. Mater.* 45, 688–694 (2016).

182. Saragih A.D., Kuo D.H., and Tuan T.T.A.: Thin film solar cell based on p-CuSbS₂ together with Cd-free GaN/InGaN bilayer. *J. Mater. Sci.: Mater. Electron.* 28, 2996–3003 (2017).

183. Gerein N.J. and Haber J.A.: Synthesis of Cu₃BiS₃ thin films by heating metal and metal sulfide precursor films under hydrogen sulfide. *Chem. Mater.* 18, 6289–6296 (2006).

184. Gerein N.J. and Haber J.A.: One-step synthesis and optical and electrical properties of thin film Cu₃BiS₃ for use as a solar absorber in photovoltaic devices. *Chem. Mater.* 18, 6297–6302 (2006).

185. Gerein N.J. and Haber J.A.: INOR 861-synthesis and characterization of Cu₃BiS₃ for use as a solar absorber layer in thin film photovoltaic devices. *Abstr. Pap. Am. Chem. Soc.* 232, 1 (2006).

186. Gerein N.J. and Haber J.A.: *Synthesis and Optical and Electrical Properties of Thin Film Cu₃BiS₃: A Potential Solar Absorber for Photovoltaic Devices* (IEEE, New York, 2006).

187. Al-Saab F.: *Optoelectronics Research Centre* (University of Southampton, U.K. 2015).

188. Riha S.C., Koegel A.A., Emery J.D., Pellin M.J., and Martinson A.B.F.: Low-temperature atomic layer deposition of $CuSbS_2$ for thin-film photovoltaics. *ACS Appl. Mater. Interfaces* 9, 4667–4673 (2017).

189. Shi L., Li Y.N., Wu C.Y., and Dai Y.M.: Preparation, formation mechanism and photoelectric properties of well-aligned $CuSbS_2$ nanowires. *J. Alloys Compd.* 648, 507–511 (2015).

190. Viezbicke B.D. and Birnie D.P.: Solvothermal synthesis of Cu_3BiS_3 enabled by precursor complexing. *ACS Sustain. Chem. Eng.* 1, 306–308 (2013).

191. Epstein J.A., Castellano R.J., Shan J.W., and Birnie D.P.: Benchtop microreactor built for diagnostic deposition of Cu_3BiS_3 for use in photovoltaic devices. *Comput. Therm. Sci.* 7, 501–513 (2015).

192. Vinayakumar V., Shaji S., Avellaneda D., Das Roy T.K., Castillo G.A., Martinez J.A.A., and Krishnan B.: $CuSbS_2$ thin films by rapid thermal processing of Sb_2S_3–Cu stack layers for photovoltaic application. *Sol. Energy Mater. Sol. Cells* 164, 19–27 (2017).

193. Yakushev M.V., Maiello P., Raadik T., Shaw M.J., Edwards P.R., Krustok J., Mudryi A.V., Forbes I., and Martin R.W.: Electronic and structural characterisation of Cu_3BiS_3 thin films for the absorber layer of sustainable photovoltaics. *Thin Solid Films* 562, 195–199 (2014).

194. Yakushev M.V., Maiello P., Raadik T., Shaw M.J., Edwards P.R., Krustok J., Mudryi A.V., Forbes I., and Martin R.W.: Investigation of the structural, optical and electrical properties of Cu_3BiS_3 semiconducting thin films. In *Advanced Materials and Characterization Techniques for Solar Cells II*, Gordon I., Valenta J., Turan R., Atwater H., and Mirabella S., eds. (Elsevier Science Bv, Amsterdam, 2014); pp. 166–172.

195. Liu X.Y., Zheng H.W., Zhang J.W., Xiao Y., and Wang Z.Y.: Photoelectric properties and charge dynamics for a set of solid state solar cells with $Cu_4Bi_4S_9$ as the absorber layer. *J. Mater. Chem. A* 1, 10703–10712 (2013).

196. Liu X.Y., Wang S., Zhang J.W., Zhang J.W., and Gu Y.Z.: Photoelectric properties and charge dynamics in ZnO nanowires/$Cu_4Bi_4S_9$ and ZnO nanowires/In_2O_3/$Cu_4Bi_4S_9$ heterostructures. *J. Appl. Phys.* 116, 9 (2014).

197. Liu X.Y., Wang S., Zheng H.W., Cheng X.Y., and Gu Y.Z.: Photochemical charges separation and photoelectric properties of flexible solar cells with two types of heterostructures. *Appl. Phys. Lett.* 107, 5 (2015).

198. Liu X.Y., Wang S., Zheng H.W., Cheng X.Y., and Gu Y.Z.: Comprehensive insights into charge dynamics and improved photoelectric properties of well-designed solar cells. *ACS Appl. Mater. Interfaces* 8, 20701–20709 (2016).

199. Liu X.Y., Wang S., Zheng H.W., and Gu Y.Z.: Insights into collaborative separation process of photogenerated charges and superior performance of solar cells. *Appl. Phys. Lett.* 109, 043906 (2016).

200. Wang S., Liu X.Y., and Gu Y.Z.: Excellent photoelectric properties and charge dynamics of two types of bulk heterojunction solar cells. *Mater. Lett.* 166, 251–254 (2016).

201. Li H.X., Zhang Q.L., Pan A.L., Wang Y.G., Zou B.S., and Fan H.J.: Single-crystalline $Cu_4Bi_4S_9$ nanoribbons: Facile aynthesis, growth mechanism, and surface photovoltaic properties. *Chem. Mater.* 23, 1299–1305 (2011).

202. Kehoe A.B., Temple D.J., Watson G.W., and Scanlon D.O.: Cu_3MCh_3 (M = Sb, Bi; Ch = S, Se) as candidate solar cell absorbers: Insights from theory. *Phys. Chem. Chem. Phys.* 15, 15477–15484 (2013).

203. Chen R.Z. and Persson C.: High absorption coefficients of the $CuSb(Se,Te)_2$ and $CuBi(S,Se)_2$ alloys enable high-efficient 100 nm thin-film photovoltaics. *EPJ Photovoltaics* 8, 8 (2017).

204. Kumar M. and Persson C.: $Cu(Sb,Bi)(S,Se)_2$ as indium-free absorber material with high optical efficiency. *Energy Procedia (Proceedings of E-MRS Spring Meeting 2013 Symposium D Advanced Inorganic Materials and Structures for Photovoltaics)* 44, 176–183 (2014).

205. Gudelli V.K., Kanchana V., Vaitheeswaran G., Svane A., and Christensen N.E.: Thermoelectric properties of chalcopyrite type $CuGaTe_2$ and chalcostibite $CuSbS_2$. *J. Appl. Phys.* 114, 8 (2013).

206. Kumar M. and Persson C.: $CuSbS_2$ and $CuBiS_2$ as potential absorber materials for thin-film solar cells. *J. Renewable Sustainable Energy* 5, 6 (2013).

207. Tablero C.: Microscopic analysis and applications of the $Cu(Sb,Bi)S_2$ high optical absorption. *J. Phys. Chem. C* 119, 8857–8863 (2015).

208. Do D., Ozolins V., Mahanti S.D., Lee M.S., Zhang Y.S., and Wolverton C.: Physics of bandgap formation in Cu–Sb–Se based novel thermoelectrics: The role of Sb valency and Cu d levels. *J. Phys.: Condens. Matter* 24, 7 (2012).

209. Zhang S.R., Zeng D.P., Xie L.H., Deng X.P., and Song K.H.: First-principles study of the elastic and thermodynamic properties of $CuBiS_2$ photovoltaic absorber material. *Chalcogenide Lett.* 11, 661–670 (2014).

210. Kumar M. and Persson C.: Cu_3BiS_3 as a potential photovoltaic absorber with high optical efficiency. *Appl. Phys. Lett.* 102, 4 (2013).

211. Li J., Wang X.X., Liu R.B., Shi L.J., Kamran M.A., Zhong H.Z., and Zou B.S.: The length controllable synthesis and near-infrared photoluminescence of one-dimensional ternary $Cu_4Bi_4S_9$ semiconductor nanobelts. *Mater. Res. Bull.* 49, 180–186 (2014).

212. Welch A.W., Baranowski L.L., Peng H.W., Hempel H., Eichberger R., Unold T., Lany S., Wolden C., and Zakutayev A.: Trade-offs in thin film solar cells with layered chalcostibite photovoltaic absorbers. *Adv. Energy Mater.* 7, 7 (2017).

213. Xu D.Y., Shen S.L., Zhang Y.J., Gu H.W., and Wang Q.B.: Selective synthesis of ternary copper–antimony sulfide nanocrystals. *Inorg. Chem.* 52, 12958–12962 (2013).

214. Deng M.J., Shen S.L., Zhang Y.J., Xu H.R., and Wang Q.B.: A generalized strategy for controlled synthesis of ternary metal sulfide nanocrystals. *New J. Chem.* 38, 77–83 (2014).

215. Zhou S.M., Ma D.K., Zhang S.H., Wang W., Chen W., Huang S.M., and Yu K.: PEGylated Cu_3BiS_3 hollow nanospheres as a new photothermal agent for 980 nm-laser-driven photothermochemotherapy and a contrast agent for X-ray computed tomography imaging. *Nanoscale* 8, 1374–1382 (2016).

216. Kaur D.K.P.I. and Chopra K.L.: Growth kinetics and polymorphism of chemically deposited CdS films. *J. Electrochem. Soc.* 127, 943–948 (1980).

217. Guria A.K., Prusty G., Chacrabarty S., and Pradhan N.: Fixed aspect ratio rod-to-rod conversion and localized surface plasmon resonance in semiconducting I-V-VI nanorods. *Adv. Mater.* 28, 447 (2016).

218. Senevirathna D.C., Werrett M.V., Pai N., Blair V.L., Spiccia L., and Andrews P.C.: Formation of group 11 bismuth sulfide nanoparticles using bismuth dithioates under mild conditions. *Chem.–Eur. J.* 23, 8171–8175 (2017).

219. Zhang H.H., Xu Q.S., and Tan G.L.: Physical preparation and optical properties of $CuSbS_2$ nanocrystals by mechanical alloying process. *Electron. Mater. Lett.* 12, 568–573 (2016).

220. Marino C., Block T., Pottgen R., and Villevieille C.: $CuSbS_2$ as a negative electrode material for sodium ion batteries. *J. Power Sources* 342, 616–622 (2017).

221. Kryukova G., Heuer M., Doering T., and Bente K.: Micro- and nanowires of iodine-containing $Cu_4Bi_4S_4$. *J. Cryst. Growth* 306, 212–216 (2007).

222. Su H.L., Xie Y., Wan S.K., Li B., and Qian Y.T.: A novel one-step solvothermal route to nanocrystalline $CuSbS_2$ and Ag_3SbS_3. *Solid State Ionics* 123, 319–324 (1999).

223. Wang M.X., Yue G.H., Fan X.Y., and Yan P.X.: Properties and characterization of Cu_3SbS_3 nanowires synthesized by solvothermal route. *J. Cryst. Growth* 310, 3062–3066 (2008).

224. van Embden J. and Tachibana Y.: Synthesis and characterisation of famatinite copper antimony sulfide nanocrystals. *J. Mater. Chem.* 22, 11466–11469 (2012).

225. van Embden J., Latham K., Duffy N.W., and Tachibana Y.: Near-infrared absorbing $Cu_{12}Sb_4S_{13}$ and Cu_3SbS_4 nanocrystals: Synthesis, characterization, and photoelectrochemistry. *J. Am. Chem. Soc.* 135, 11562–11571 (2013).

226. Ramasamy K., Sims H., Butler W.H., and Gupta A.: Selective nanocrystal synthesis and calculated electronic structure of all four phases of copper–antimony–sulfide. *Chem. Mater.* 26, 2891–2899 (2014).

227. Ikeda S., Sogawa S., Tokai Y., Septina W., Harada T., and Matsumura M.: Selective production of $CuSbS_2$, Cu_3SbS_3, and Cu_3SbS_4 nanoparticles using a hot injection protocol. *RSC Adv.* 4, 40969–40972 (2014).

228. Liang Q.S., Huang K.K., Ren X.R., Zhang W., Xie R.G., and Feng S.H.: Synthesis of Cu–Sb–S nanocrystals: Insight into the mechanism of composition and crystal phase selection. *CrystEngComm* 18, 3703–3710 (2016).

229. Zhang Z.A., Zhou C.K., Liu Y.K., Li J., Lai Y.Q., and Jia M.: CuSbS₂ nanobricks as electrode materials for lithium ion batteries. *Int. J. Electrochem. Sci.* 8, 10059–10067 (2013).

230. Ramasamy K., Gupta R.K., Sims H., Palchoudhury S., Ivanov S., and Gupta A.: Layered ternary sulfide CuSbS₂ nanoplates for flexible solid-state supercapacitors. *J. Mater. Chem. A* 3, 13263–13274 (2015).

231. An C.H., Liu Q.C., Tang K.B., Yang Q., Chen X.Y., Liu J.W., and Qian Y.T.: The influences of surfactant concentration on the quality of chalcostibite nanorods. *J. Cryst. Growth* 256, 128–133 (2003).

232. Qiu X.D., Ji S.L., Chen C., Liu G.Q., and Ye C.H.: Synthesis, characterization, and surface-enhanced Raman scattering of near infrared absorbing Cu₃SbS₃ nanocrystals. *CrystEngComm* 15, 10431–10434 (2013).

233. Ramasamy K., Tien B., Archana P.S., and Gupta A.: Copper antimony sulfide (CuSbS₂) mesocrystals: A potential counter electrode material for dye-sensitized solar cells. *Mater. Lett.* 124, 227–230 (2014).

234. Zou Y. and Jiang J.: Colloidal synthesis of chalcostibite copper antimony sulfide nanocrystals. *Mater. Lett.* 123, 66–69 (2014).

235. Zhang Z., Fu Y., Zhou C.K., and Lai Y.Q.: Facile synthesis of CuSbS₂ blocks, and their lithium ion storage performance. *J. Electron. Mater.* 44, 252–257 (2015).

236. Liu Z.F., Huang J.J., Han J.H., Hong T.T., Zhang J., and Liu Z.H.: CuSbS₂: A promising semiconductor photo-absorber material for quantum dot sensitized solar cells. *Phys. Chem. Chem. Phys.* 18, 16615–16620 (2016).

237. Shi L., Wu C.Y., Li J.J., and Ding J.: Selective synthesis and photoelectric properties of Cu₃SbS₄ and CuSbS₂ nanocrystals. *J. Alloys Compd.* 694, 132–135 (2017).

238. Han M.M., Jia J.H., and Wang W.Z.: A novel CuSbS₂ hexagonal nanobricks @ TiO₂ nanorods heterostructure for enhanced photoelectrochemical characteristics. *J. Alloys Compd.* 705, 356–362 (2017).

239. Zhong J.S., Xiang W.D., Jin H.D., Cai W., Liu L.J., Yang X.Y., Liang X.J., and Liu H.T.: A simple L-cystine-assisted solvothermal approach to Cu₃SbS₃ nanorods. *Mater. Lett.* 64, 1499–1502 (2010).

240. Li Z.R., Zhong J.S., Chen Z.P., Cai Q., Liang X.J., and Xiang W.D.: Preparation and formation mechanism of Cu₃SbS₃ nanorods. *Rare Met. Mater. Eng.* 41, 1–5 (2012).

241. Hao Z.M., Zeng D.M., Chen L.M., and Huang F.J.: Synthesis and characterization of Cu₃SbS₃ nanocrystallites: Effect of reaction time. *Mater. Lett.* 122, 338–340 (2014).

242. Chen K.Q., Zhou J., Chen W., Zhou P., He F., and Liu Y.L.: Size-dependent synthesis of Cu₁₂Sb₄S₁₃ nanocrystals with bandgap tunability. *Part. Part. Syst. Charact.* 32, 999–1005 (2015).

243. Chen K.Q., Zhou J., Chen W., Chen Q., Zhou P., and Liu Y.L.: A green synthesis route for the phase and size tunability of copper antimony sulfide nanocrystals with high yield. *Nanoscale* 8, 5146–5152 (2016).

244. Hsiang H.I., Yang C.T., and Tu J.H.: Characterization of CuSbSe₂ crystallites synthesized using a hot injection method. *RSC Adv.* 6, 99297–99305 (2016).

245. Chen D., Shen G.Z., Tang K.B., Liu X.M., Qian Y.T., and Zhou G.E.: The synthesis of Cu₃BiS₃ nanorods via a simple ethanol-thermal route. *J. Cryst. Growth* 253, 512–516 (2003).

246. Hu J.Q., Deng B., Wang C.R., Tang K.B., and Qian Y.T.: Convenient hydrothermal decomposition process for preparation of nanocrystalline mineral Cu₃BiS₃ and Pb₁₋ₓBi₂ₓ/₃S. *Mater. Chem. Phys.* 78, 650–654 (2003).

247. Shen G.Z., Chen D., Tang K.B., and Qian Y.T.: Synthesis of ternary sulfides Cu(Ag)–Bi–S coral-shaped crystals from single-source precursors. *J. Cryst. Growth* 257, 293–296 (2003).

248. Aup-Ngoen K., Thongtem S., and Thongtem T.: Cyclic microwave-assisted synthesis of Cu₃BiS₃ dendrites using L-cysteine as a sulfur source and complexing agent. *Mater. Lett.* 65, 442–445 (2011).

249. Zhong J.S., Xiang W.D., Cai Q., and Liang X.J.: Synthesis, characterization and optical properties of flower-like Cu₃BiS₃ nanorods. *Mater. Lett.* 70, 63–66 (2012).

250. Yan J.M., Yu J., Zhang W.J., Li Y.N., Yang X.Y., Li A.M., Yang X.K., Wang W., and Wang J.Q.: Synthesis of Cu₃BiS₃ and AgBiS₂ crystallites with controlled morphology using hypocrellin template and their catalytic role in the polymerization of alkylsilane. *J. Mater. Sci.* 47, 4159–4166 (2012).

251. Zeng Y.P., Li H.X., Qu B.H., Xiang B.Y., Wang L., Zhang Q.L., Li Q.H., Wang T.H., and Wang Y.G.: Facile synthesis of flower-like Cu₃BiS₃ hierarchical nanostructures and their electrochemical properties for lithium-ion batteries. *CrystEngComm* 14, 550–554 (2012).

252. Yan C., Gu E.N., Liu F.Y., Lai Y.Q., Li J., and Liu Y.X.: Colloidal synthesis and characterizations of wittichenite copper bismuth sulphide nanocrystals. *Nanoscale* 5, 1789–1792 (2013).

253. Li B., Ye K.C., Zhang Y.X., Qin J.B., Zou R.J., Xu K.B., Huang X.J., Xiao Z.Y., Zhang W.J., Lu X.W., and Hu J.Q.: Photothermal theragnosis synergistic therapy based on bimetal sulphide nanocrystals rather than nanocomposites. *Adv. Mater.* 27, 1339 (2015).

254. Yang Y., Wu H.X., Shi B.Z., Guo L.L., Zhang Y.J., An X., Zhang H., and Yang S.P.: Hydrophilic Cu₃BiS₃ nanoparticles for computed tomography imaging and photothermal therapy. *Part. Part. Syst. Charact.* 32, 668–679 (2015).

255. Du J.F., Zheng X.P., Yong Y., Yu J., Dong X.H., Zhang C.Y., Zhou R.Y., Li B., Yan L., Chen C.Y., Gu Z.J., and Zhao Y.L.: Design of TPGS-functionalized Cu₃BiS₃ nanocrystals with strong absorption in the second near-infrared window for radiation therapy enhancement. *Nanoscale* 9, 8229–8239 (2017).

256. Li A., Li X., Yu X.J., Li W., Zhao R.Y., An X., Cui D.X., Chen X.Y., and Li W.W.: Synergistic thermoradiotherapy based on PEGylated Cu₃BiS₃ ternary semiconductor nanorods with strong absorption in the second near-infrared window. *Biomaterials* 112, 164–175 (2017).

257. Aup-Ngoen K., Dumrongrojthanath P., Thongtem T., and Thongtem S.: Effect of medium solvents on crystalline degree and specific surface area of Cu₃BiS₃ nanoparticles synthesised by biomolecule-assisted hydrothermal and solvothermal methods. *Internet J. Nanotechnol.* 14, 22–30 (2017).

258. Zhong J.S., Wang Q.Y., Zhu X., Chen D.Q., and Ji Z.G.: Sovolthermal synthesis of flower-like Cu₃BiS₃ sensitized TiO₂ nanotube arrays for enhancing photoelectrochemical performance. *J. Alloys Compd.* 641, 144–147 (2015).

259. Gao X., Wang Y., Ma Z.S., Jiang W.J., Zou Y.L., and Lu C.S.: A ternary sulphonium composite Cu₃BiS₃/S as cathode materials for lithium-sulfur batteries. *J. Mater. Sci.* 51, 5139–5145 (2016).

260. Li J., Zhong H.Z., Liu H.J., Zhai T.Y., Wang X., Liao M.Y., Bando Y., Liu R.B., and Zou B.S.: One dimensional ternary Cu–Bi–S based semiconductor nanowires: Synthesis, optical and electrical properties. *J. Mater. Chem.* 22, 17813–17819 (2012).

261. Yu L.P., Kokenyesi R.S., Keszler D.A., and Zunger A.: Inverse design of high absorption thin-film photovoltaic materials. *Adv. Energy Mater.* 3, 43–48 (2013).

262. Ganose A.M., Savory C.N., and Scanlon D.O.: Beyond methylammonium lead iodide: prospects for the emergent field of ns² containing solar absorbers. *Chem. Commun.* 53, 20–44 (2017).

263. Tablero C.: Electronic property analysis of O-doped Cu₃SbS₃. *Sol. Energy Mater. Sol. Cells* 104, 180–184 (2012).

264. Tablero C.: Photovoltaic application of O-doped Wittichenite-Cu₃BiS₃: From microscopic properties to maximum efficiencies. *Prog. Photovoltaics* 21, 894–899 (2013).

265. Luque A. and Marti A.: Increasing the efficiency of ideal solar cells by photon induced transitions at intermediate levels. *Phys. Rev. Lett.* 78, 5014–5017 (1997).

266. Mesa F., Ballesteros V., and Dussan A.: Growth analysis and numerical simulation of Cu₃BiS₃ absorbing layer solar cell through the wxAMPS and finite element method. *Acta Phys. Pol., A* 125, 385–387 (2014).

267. Liu Y.M., Sun Y., and Rockett A.: A new simulation software of solar cells-wxAMPS. *Sol. Energy Mater. Sol. Cells* 98, 124–128 (2012).

268. Yin J.B. and Jia J.H.: Synthesis of Cu₃BiS₃ nanosheet films on TiO₂ nanorod arrays by a solvothermal route and their photoelectrochemical characteristics. *CrystEngComm* 16, 2795–2801 (2014).

269. Septina W., Ikeda S., Iga Y., Harada T., and Matsumura M.: Thin film solar cell based on CuSbS₂ absorber fabricated from an electrochemically deposited metal stack. *Thin Solid Films* 550, 700–704 (2014).

270. Welch A.W., Baranowski L.L., Lucas F.W.D., Toberer E.S., Wolden C.A., and Zakutayev A.: Copper antimony chalcogenide thin film PV device development. In *2015 IEEE 42nd Photovoltaic Specialist Conference* (IEEE, New York, 2015).

271. Claybourn M., Brinkman A.W., Russell G.J., and Woods J.: Electron traps in single-crystal CdS. *Philos. Mag. B* 56, 385–395 (1987).

272. Suriyawong N., Aragaw B., Shi J.B., and Lee M.W.: Ternary CuBiS$_2$ nanoparticles as a sensitizer for quantum dot solar cells. *J. Colloid Interface Sci.* 473, 60–65 (2016).

273. Mesa F., Dussan A., Sandino J., and Lichte H.: Characterization of Al/Cu$_3$BiS$_3$/buffer/ZnO solar cells structure by TEM. *J. Nanopart. Res.* 14, 7 (2012).

274. Seto J.Y.W.: The electrical properties of polycrystalline silicon films. *Appl. Phys.* 46, 5247 (1975).

275. Rodriguez-Lazcano Y., Nair M.T.S., and Nair P.K.: Photovoltaic p–i–n structure of Sb$_2$S$_3$ and CuSbS$_2$ absorber films obtained via chemical bath deposition. *J. Electrochem. Soc.* 152, G635–G638 (2005).

276. Duta A., Visa M., Manolache S.A., and Nanu M.: *Anatase (TiO$_2$) Thin Layers for Solar Energy Conversion* (IEEE, New York, 2008).

277. Suehiro S., Horita K., Yuasa M., Tanaka T., Fujita K., Ishiwata Y., Shimanoe K., and Kida T.: Synthesis of copper–antimony–sulfide nanocrystals for solution processed solar cells. *Inorg. Chem.* 54, 7840–7845 (2015).

278. Welch A.W., Baranowski L.L., Zawadzki P., DeHart C., Johnston S., Lany S., Wolden C.A., and Zakutayev A.: Accelerated development of CuSbS$_2$ thin film photovoltaic device prototypes. *Prog. Photovoltaics* 24, 929–939 (2016).

279. Macias C., Lugo S., Benitez A., Lopez I., Kharissov B., Vazquez A., and Pena Y.: Thin film solar cell based on CuSbS$_2$ absorber prepared by chemical bath deposition (CBD). *Mater. Res. Bull.* 87, 161–166 (2017).

280. Abdullah H. and Kuo D.H.: Photocatalytic performance of Ag and CuBiS$_2$ nanoparticle-coated SiO$_2$@TiO$_2$ composite sphere under visible and ultraviolet light irradiation for azo dye degradation with the assistance of numerous nano p–n diodes. *J. Phys. Chem. C* 119, 13632–13641 (2015).

281. Abdullah H. and Kuo D.H.: Photocatalytic performance of the SiO$_2$ sphere/n-type TiO$_2$/p-type CuBiS$_2$ composite catalysts coated with different contents of Ag nanoparticles under ultraviolet and visible light irradiations. *Appl. Phys. A: Mater. Sci. Process.* 122, 11 (2016).

282. Abdullah H., Kuo D.H., Lee J.Y., and Wu C.M.: Recyclability of thin nylon film-supported p-CuBiS$_2$/n-TiO$_2$ heterojunction-based nanocomposites for visible light photocatalytic degradation of organic dye. *Appl. Phys. A: Mater. Sci. Process.* 122, 12 (2016).

283. Alsaleh N.M., Singh N., and Schwingenschlogl U.: Role of interlayer coupling for the power factor of CuSbS$_2$ and CuSbSe$_2$. *Phys. Rev. B* 94, 6 (2016).

284. Li D., Li R., Qin X-Y., Song C-J., Xin H-X., Wang L., Zhang J., Guo G-L., Zou T-H., Liu Y-F., and Zhu X-G.: Co-precipitation synthesis of nanostructured Cu$_3$SbSe$_4$ and its Sn-doped sample with high thermoelectric performance. *Dalton Trans.* 43, 1888–1896 (2014).

285. Skoug E.J., Cain J.D., and Morelli D.T.: High thermoelectric figure of merit in the Cu$_3$SbSe$_4$–Cu$_3$SbS$_3$ solid solution. *Appl. Phys. Lett.* 98, 261911 (2011).

286. Parker D. and Singh D.J.: Transport properties of hole-doped CuBiS$_2$. *Phys. Rev. B* 83, 4 (2011).

287. Anandraj J. and Joshi G.M.: CuBi$_2$S$_3$ precursor based polymer composites for low frequency capacitor applications. *J. Mater. Sci.: Mater. Electron.* 27, 10550–10561 (2016).

288. Wubet W., Saragih A.D., and Kuo D.H.: Structural and electrical property analysis of bulk Cu$_{1-x}$Ag$_x$SbS$_2$. *J. Solid State Chem.* 252, 100–105 (2017).

289. Chen D., Shen G.Z., Tang K.B., Jiang X., Huang L.Y., Jin Y., and Qian Y.T.: Polyol mediated synthesis of nanocrystalline M$_3$SbS$_3$ (M = Ag, Cu). *Mater. Res. Bull.* 38, 509–513 (2003).

290. Daniel T., Henry J., Mohanraj K., and Sivakumar G.: AgSbS$_2$ and Ag$_3$SbS$_3$ absorber materials for photovoltaic applications. *Mater. Chem. Phys.* 181, 415–421 (2016).

291. Liu F.Y., Li J.Y., Yang J., Han Z.L., Jiang L.X., Lai Y.Q., Li J., He Y.H., and Liu Y.X.: Preparation and characterization of AgSbSe$_2$ thin films by electrodeposition. *J. Electrochem. Soc.* 160, D578–D582 (2013).

292. Chen Y.C., Yao H.B., Thiagarajan S., Wu M., Emge T.J., Yang R.G., Yu S.H., and Li J.: Layered hybrid selenoantimonates with reduced thermal conductivity. *Z. Anorg. Allg. Chem.* 638, 2604–2609 (2012).

Appendix 1: Silver analogues of the Cu–Sb and Cu–Bi chalcogenides

Table A1. Reports of the silver containing compounds as electronic materials and also a list of the known mineralogical phases reported by Moelo.[7]

Compound	References in the electronic materials literature	Mineral name[7]
$AgSbS_2$	288	Cuboargyrite
$(Cu_{1-x}Ag_x)SbS_2$	288	…
Ag_3SbS_3	222, 289, and 290	Pyragyrite; pyrostipnite
Ag_5SbS_4	…	Stephanite
Ag_3SbS_6	…	Baumstarkite
$AgSbSe_2$	291	…
Ag_2SbSe_3	292	…
$AgSbTe_2$	17	…
$AgBiS_2$	214, 218, 247, and 250	Matilidite
$AgBi_3S_5$	…	Pavonite
$Cu_8AgBi_{13}S_{24}$	…	Cuprobismutite
$Ag_3Bi_7S_{12}$	…	Benjaminite
$AgBiSe_2$	…	Bohdanowiczite
$Ag_9Sb(S,Se)_3Te_3$	…	Tsnigriite
$AgBiTe_2$	…	Volynskite